Wideband Channel Sounding Techniques for Dynamic Spectrum Access Networks

Qi Chen

Submitted to the Graduate Degree Program in Electrical Engineering & Computer Science and the Graduate Faculty of the University of Kansas in partial fulfillment of the requirements for the degree of Doctor of Philosophy

Dissertation Committee:

Dr. Gary J. Minden: Chairperson

Dr. James A. Roberts

Dr. Alexander M. Wyglinski

Dr. Erik S. Perrins

Dr. Tyrone E. Duncan

Date Defended

The Dissertation Committee for Qi Chen certifies
that this is the approved version of the following dissertation:

Wideband Channel Sounding Techniques for Dynamic Spectrum Access Networks

Committee:

Dr. Gary J. Minden,
Professor, EECS

Dr. James A. Roberts,
Professor, EECS

Dr. Alexander M. Wyglinski,
Assistant Professor, ECE, WPI

Dr. Erik S. Perrins,
Assistant Professor, EECS

Dr. Tyrone E. Duncan,
Professor, Mathematics

Date Approved

Abstract

In recent years, cognitive radio has drawn extensive research attention due to its ability to improve the efficiency of spectrum usage by allowing dynamic spectrum resource sharing between primary and secondary users. The concept of cognitive radio was first presented by Joseph Mitola III and Gerald Q. Maguire, Jr., in which either network or wireless node itself changes particular transmission and reception parameters to execute its tasks efficiently without interfering with the primary users [1]. Such a transceiving mechanism and network environment is called the dynamic spectrum access (DSA) network. The Federal Communications Commission (FCC) allows any type of transmission in unlicensed bands at any time as long as their transmit power level obeys specific FCC regulations. Performing channel sounding as a secondary user in such an environment becomes a challenge due to the rapidly changing network environment and also the limited transmission power. Moreover, to obtain the long term behavior of the channel in the DSA network is impractical with conventional channel sounders due to frequent changes in frequency, transmission bandwidth, and power. Conventional channel sounding techniques need to be adapted accordingly to be operated in the DSA networks.

In this dissertation, two novel channel sounding system frameworks are proposed. The *Multicarrier Direct Sequence Swept Time-Delay Cross Correlation* (MC-DS-STDCC) channel sounding technique is designed for the DSA networks aiming to perform channel sounding across a large bandwidth with minimal interference. It is based on the STDCC channel sounder and *Multicarrier Direct Sequence Code Division Multiple Access* (MC-DS-CDMA) technique. The STDCC technique, defined by Parsons [2], was first employed by Cox in the measurement of 910 MHz band [3–6]. The MC-DS-CDMA technique enables the channel sounder to be operated at different center frequencies with low transmit power. Hence, interference awareness and frequency agility are achieved. The OFDM-based channel sounder is an alternative to the MC-DS-STDCC technique. It utilizes user data as the sounding signal such that the interference is minimized during the course of transmission. Furthermore, the OFDM-based channel sounder requires lower sampling rate than the MC-DS-STDCC system since no spreading is necessary.

To my parents and my lovely wife Jin Zhu

Acknowledgments

First, I would like to express my deepest gratitude to my advisor Professor Gary J. Minden for his excellent guidance and continual support during the course of my degree. Second, I would like thank Dr. Alexander M. Wyglinski (former assistant research professor at the University of Kansas) at Worcester Polytechnic Institute for being such a good friend, and for providing generous help and guidance throughout my research. Working with them was a wonderful experience. I am very grateful for their time and patience dedicated to my research and dissertation.

The financial support provided by the National Science Foundation under the project "National Radio Testbed" as well as the EECS department are duly acknowledged. I would like to thank Professor James A. Roberts for providing me the opportunity at the University of Kansas for pursuing a Ph.D. degree. I would also like to thank Professor John Gauch for accepting and processing my late application.

I would like to thank Professor Erik S. Perrins and Professor Tyrone Duncan for agreeing to be on my committee. During my time at the University of Kansas, I met numerous students, faculty and staff in the Information and Telecommunication Technology Center (ITTC), the Electrical Engineering and Computer Science department, and the University of Kansas in general, who have made my Ph.D. experience all the more rewarding, and to them I owe my thanks. In particular, I would like to thank Tim Newman, Biao Fu, Rakesh Rajbanshi, Dinesh Datla, Mike Hulet, Annie Francis, and Paula Conlin. I would also like to thank Dan Depardo and Leon Searl for sharing their professional knowledge, for helping me solve problems during my research and other staff at ITTC who have directly or indirectly helped me complete my studies successfully.

As always, I am deeply indebted to my parents. Without their generous support, I would not have completed all my achievements. Finally, I would like to thank my lovely wife Jin for her love, understanding, support, and unwavering belief in me.

Contents

List of Figures

List of Tables

List of Symbols

$x(t)$	Transmitted signal
$y(t)$	Received signal
$h(t, \tau)$	Impulse response of the time varying multipath fading channel
$\Delta\tau$	Minimum delay resolution
τ_i	Delay of i^{th} path
$\tau_{\max}$	Maximum delay spread
N	Number of subcarriers of the OFDM and MC-CDMA systems
N_0	Noise power
$R_{\tilde{c}}$	Autocorrelation function of the time-varying channel
$S(\tau, \omega)$	Scattering function
$\mathbb{F}_{\Delta t}[\cdot]$	FFT
$\tilde{c}(\tau, t)$	Complex impulse response
$p(\tau)$	Power delay profile
$S(\omega)$	Doppler spectrum
σ_τ	*rms* delay spread
B_c	Coherence bandwidth
$\rho_{\Delta f}$	Frequency correlation coefficient
E[$\cdot$]	Expected value
f_{slip}	Slip rate
K_{scale}	Scaling factor for the STDCC
I	In-phase
Q	Quadrature

L	m-sequence length
f_{D}	Maximum Dopper shift
c	Speed of light
F_{n}	Subcarrier separation parameter
D_{dB}	Dynamic range for the channel sounder in decibel
$O(\cdot)$	On the order of
ρ	The percentage of 0s in one OFDM symbol period
γ	Signal-to-noise ratio for Rayleigh fading channel
P_e	Irreducible error floor for MC-CDMA system

List of Acronyms

ACF	Autocorrelation Function
A/D	Analog to Digital
ADC	Analog to Digital Converter
AP	Amplifier
AWGN	Additive White Gaussian Noise
BPSK	Binary Phase Shift Keying
CDMA	Code Division Multiple Access
CIR	Channel Impulse Response
CP	Cyclic Prefix
CR	Cognitive Radios
CW	Continuous Wave
DAC	Digital to Analog Converter
DARPA	Defense Advanced Research Pro jects Agency
DFT	Discrete Fourier Transform
DS	Direct Sequence
DSA	Dynamic Spectrum Access
DSP	Digital Signal Processing
EIRP	Equivalent Isotropically Radiated Power
FCC	Federal Communications Commission
FFT	Fast Fourier Transform
FPGA	Field Programmable Gate Array
GPS	Global Positioning System
GUI	Graphical User Interface
GNU	Gnu's Not Unix
ICI	Inter-carrier Interference

IF	Intermediate Frequency
IFFT	Inverse Fast Fourier Transform
ISI	Inter-Symbol Interference
ISM	Industrial, Scientific and Medical
KUAR	Kansas University Agile Radio
LOS	Line-of-Sight
LNA	Low Noise Amplifier
LFSR	Linear Feedback Shift Registers
MC-DS-CDMA	Multicarrier Direct Sequence Code Division Multiple Access
MC-DS-STDCC	Multicarrier Direct Sequence Swept Time Delay Cross-Correlation
MCM	Multicarrier Modulation
M-PSK	M-ary Phase Shift Keying
MSE	Mean Squared Error
PAPR	Peak-to-Average Power Ratio
PDP	Power Delay Profile
PN	Pseudo-Random
PRBS	Pseudo-Random Binary Sequence
PRF	Pulse Repetition Frequency
PSD	Power Spectrum Density
P/S	Parallel to Serial
OFDM	Orthogonal Frequency Division Multiplexing
OverDRiVE	over Dynamic Multi-Radio Networks in Vehicular Environments
OVSF	Orthogonal Variable Spreading Factor
RF	Radio Frequency
RMS	Root Mean Square
RSSI	Received Signal Strength Indicator
RX	Receive
SAW	Surface Acoustic Wave
SC	Single-Carrier
SDR	Software Defined Radio

SNR	Signal-to-Noise Ratio
SNIR	Signal-to-Noise Interference Ratio
S/P	Serial to Parallel
STDCC	Swept Time-Delay Cross-Correlation
TX	Transmit
U-NII	Unlicensed National Information Infrastructure
USRP	Universal Software Radio Peripheral
US	Uncorrelated Scattering
USB	Universal Serial Bus
UWB	Ultra Wideband
W-CDMA	Wideband-CDMA
WiMAX	Worldwide Interoperability for Microwave Access
WSS	Wide-sense Stationary
XG	Next Generation

Chapter 1

Introduction

1.1 Research Motivation

The current demand for high spectrum resource utilization has grown dramatically, with spectrum resources becoming increasingly scarce. Dynamic spectrum access (DSA) techniques are promising candidates for improving the spectrum utilization efficiency in order to achieve higher data rates. The ultimate goal of dynamic spectrum access is for the secondary users (i.e., unlicensed users) to use the unoccupied frequency band while introducing minimum interference to the primary users. This idea has already been used by the Federal Communications Commission (FCC) in the United States on the TV band, where unlicensed users can "fill" in frequency gaps to share spectrum with the primary TV signal transmission [7]. In this scenario, as long as the secondary user is aware of the primary user's existence, the interference should be kept at a minimum since TV signals are fairly consistent in terms of time and frequency band of transmission. However, in more complicated scenarios, where primary users can hop between frequencies, and the period of frequency band occupation is more random, designing a wire-

less communication system that is suitable for such a network environment can be challenging.

In order for the wireless communication systems to maximize the data rate, one has to have adequate information on the radio channel, which is done by performing channel sounding. Conventional channel sounding techniques require a licensed band to perform the measurements, which is expensive and inefficient in terms of spectrum utilization, since only the licensed user can perform operations within this band, and there is no guarantee that the band is always occupied. Dynamic spectrum access networks allow secondary users to share a licensed band with the primary users without interfering. On the other hand, the transmit power in DSA networks is also regulated by government agencies, such as the FCC in the United States. Some new technologies have been developed to overcome this challenge, such as software defined radio (SDR), cognitive radios (CR)[1], adaptive antennas, and space time coding. These techniques have been extensively researched over the past several years, such as the Next Generation (XG) program, by the Defense Advanced Research Projects Agency (DARPA) [8], and the European research project on Spectrum Efficient Uni- and Multicast Services over Dynamic Multi-Radio Networks in Vehicular Environments (OverDRiVE) [9, 10]. However, conventional channel sounding techniques are not suitable for DSA networks, for instance, the narrowband pulse sounding technique [11], since the transmitted energy is pulsed and requires a high power amplifier (AP) in the transmitter that increases the cost and complexity of the system. Matched filter and pulse compression channel sounders are superior to pulse sounding as far as system cost is concerned. However, once the system is built, it is limited to the use of a cer-

[1]Cognitive radio is designed based on SDR, where it has the ability to aware of spectrum availability.

tain frequency. Hence, to design a channel sounder for DSA networks based on cognitive radios is demanded.

Sliding correlator-based channel sounding techniques are frequency efficient in terms of spectrum utilization since bandwidth compression allows us to perform a wideband measurement with a relatively small bandwidth (slow A/D sample rate) compared to pulse sounding. However, *sliding correlator*-based techniques still require a licensed band and high transmit power to perform measurements. Thus, operating a *sliding correlator* channel sounder in the DSA network is impractical. Moreover, most of the conventional channel sounders are not SDR-based, which means that once the system is built, the parameters can be changed, but with difficulty. To operate in DSA networks, where frequent changes of transmission and reception parameters are required, conventional channel sounders have to be designed and implemented based on cognitive radios.

The existing problems motivate us to design an adaptive channel sounder for DSA networks, in which the channel sounder can be operated at different center frequencies depending on spectrum availability (either policy-based or measurement-based) with extremely small transmit power relative to the conventional techniques or adaptively varying transmit power without interfering with other users. The swept time-delay cross correlation (STDCC) sounding technique is relatively simple to implement, since it does not require a high sampling rate due to the pulse compression technique, and only requires an m-sequence generator at the transmitter and a cross-correlator at the receiver. Moreover, advanced signal processing algorithms also enable us to eliminate the intermediate frequency operation from the hardware domain to the software domain, which means that the correlation and other signal processing can either be done by an end termi-

nal computer or by the on-board FPGA, depending on the requirements. By combining the STDCC technique with the MC-DS-CDMA technique, called the MC-DS-STDCC channel sounder, the transmit power is reduced by a factor of the spreading sequence length. Moreover, the measurements can be employed at different center frequencies with varying transmit power.

An alternative solution to the combination of spread spectrum and multicarrier techniques is to use the orthogonal frequency division multiplexing (OFDM) technique as the channel sounding platform and utilize the user data to perform channel sounding without introducing a dedicated sounding signal, such that interference is minimized. The other advantage of this approach is that the sampling rate requirement is not as high as that of the MC-DS-CDMA technique, since the bandwidth is not traded for performance.

1.2 Implementation: A Whole New Story

Designing an algorithm may bring to light theoretical problems. One can tackle those problems by making reasonable assumptions. However, implementing a design will force us to face those problems and issues. For example, the sampling rate of the device is restricted by the DAC and the ADC, while when designing the algorithm we can assume that the DAC sampling rate is sufficient. Also, the baseband bandwidth requirement of the design may be too ambitious for the hardware device.

In this dissertation, the implementation issues will be assessed and studied by observing the combination of the theoretical design and hardware capability. The hardware platform for the implementation is the Universal Software Radio Peripheral (USRP), which was developed by Ettus Research [12], and we use the

GNU Radio software to accomplish every single functionality of the system other than the RF front end. This approach provides us many convenient features, such as fast system reconfigurability, pure software implementation of algorithms, low cost, etc. However, this approach is subject to the hardware capabilities when considering the system design.

1.3 Current State-of-the-Art

Channel sounding techniques and devices have been used by researchers, wireless service providers, and spectrum regulation agencies for many years to capture and study radio channel characteristics. In the early 1970s, a radio channel measuring device based on sliding correlator was first developed by Cox [3–6]. This was the first radio channel sounder that could measure both time and frequency domain characteristics of a wireless channel, and it was also the first "wide-band" channel sounder ever developed. The measurement was conducted at the 910 MHz band in an urban area of New York City, which later provided distributions for multipath delay spread and average excess delay expected by wireless device and systems. In 1991, Parsons named Cox's channel sounder the *swept time-delay cross-correlator* channel sounder [11]. He discovered the evolution of the sliding correlation channel sounding techniques and also did a comparison between different channel sounding techniques. In his paper, the channel sounders are categorized into wide-band and narrow-band based on the width of the frequency band of interest. The channel sounders are also divided into time and frequency domain based on their functionality.

As wireless communication systems become more and more complicated, accurate and comprehensive channel information becomes the key for the entire

system design. Depending on different applications, environment, and their operation center frequencies, radio channel characteristics may vary from one to another. Many researchers have conducted extensive measurements and analysis for different radio channel environments and applications [13–28]. In addition to radio channel measurement, statistical analysis on the data collected by the measuring devices plays an important role in the entire system design. Not only does statistical analysis help in understanding the radio channel, but it also provides a way of predicting the channel [21, 29–37].

Researchers have also shown that the performance in terms of delay resolution and accuracy of the first proposed channel sounder by Cox can be improved by designing a better sounding signal, applying signal processing on the collected data, as well as by eliminating the unnecessary hardware (IF stage). With modern communication technologies, the channel sounders can identify delay resolution of sub second nano seconds for indoor environments [19, 33], as well as couple hundreds of megahertz bandwidths [15]. G. Martin showed that the dynamic range of a sliding correlator can be improved by a new algorithm [38]. It was also shown in literature [23, 31, 39–44] that system performance can be improved by designing a better sounding signal as well as by the use of signal processing.

1.4 Dissertation Contributions

This dissertation presents the following novel contributions:

- Characterized the user access randomness in both frequency and time domain. Addressed challenges in designing the channel sounding system for the DSA network environment. Tasks needing to be solved were how to

perform channel sounding without interfering with other users, and how to perform channel sounding efficiently when frequent frequency and time switching is required.

- A multicarrier direct sequence spreading based channel sounding system framework combined with the STDCC channel sounder, also termed as MC-DS-STDCC, is presented. The MC-DS-STDCC utilizes direct sequence spreading to minimize the interference to other users within the same frequency band, and multicarrier modulation to achieve frequency agility. To be more specific, each subcarrier is able to adjust the transmit power by increasing or decreasing the spreading sequence length in order to satisfy the power limit. Moreover, the use of spread spectrum also increases the inherent processing gain of the system, and hence, the dynamic range of the channel sounder is enlarged.

- In contrast to the MC-DS-STDCC channel sounding technique, the OFDM-based channel sounding technique is focused on reducing the system complexity, mainly sampling rate. The OFDM-based channel sounder has the ability to use user data as the sounding signal, which eliminates the sounding signal generator, and hence the system complexity is reduced. However, the performance is directly related to the autocorrelation of the user transmit data, that is, the optimal sounding signal is achieved when the data across all subcarriers are equal to one. A tradeoff study is conducted by interpolating performance loss versus randomness of the user data. On the other hand, since the OFDM-based channel sounding technique uses user data as the sounding signal, no extra interference will be introduced as long as the

user has permission to the frequency band. However, system performance is traded off for system complexity.

- Channel sounder is a measurement device, and hence, it is only useful if implemented. In this dissertation, implementation of the STDCC is presented based on the USRP and GNU radio. Implementation of the MC-DS-STDCC and OFDM-based channel sounder is outside the scope of this dissertation because of hardware and software limitations; The USRP platform supports a maximum bandwidth of 32 MHz by adopting a custom FPGA bitstream file to bypass the bandpass filter built in on the daughter board. This bandwidth limitation is the major obstacle to implementing the MC-DS-STDCC channel sounder, which requires much higher bandwidth in order to perform spread spectrum. Indoor experiments were conducted inside Nichols Hall in Lawrence, KS. The experiment results were studied and analyzed.

1.5 Dissertation Organization

This dissertation is organized as follows: Chapter 2 discusses radio channel environments including large-scale fading and small-scale fading. Mathematical models of the radio channel are given, as well as the relationships between them. The main focus of this chapter is radio channel characteristics in both time and frequency domains. Several important channel parameters will be studied in detail, such as channel impulse response, channel frequency response, doppler spread, etc. The relationship and transform between time and frequency domain channel characteristics are emphasized. In the last section, dynamic spectrum access networks is emphasized. The challenges and necessity in designing a channel sounding

system for such a network environment are addressed.

Chapter 3 consists of a literature survey of channel sounding techniques, each of which is discussed in detail as to advantages and disadvantages, and the fundamentals of the sliding correlator theory and the STDCC technique. Problems when utilizing conventional channel sounders in the DSA network environment are addressed. The need for new channel sounding techniques for the dynamic spectrum access networks is discovered, with emphasis on the challenges that conventional channel sounding techniques encounter when being applied to such network environments.

In Chapter 4, wideband channel sounding techniques are discussed. The proposed technique is a combination of the multicarrier modulation technique and the STDCC technique. Each technique is focused on solving a particular research question. The MC-DS-STDCC technique is mainly designed for frequency-agile and interference awareness as well as channel sounding performance. Drawbacks of the MC-DS-STDCC technique are also presented, which become the motivation for the OFDM-based channel sounding technique.

High sampling rate requirement and system complexity are the two major drawbacks of the MC-DS-STDCC technique. In Chapter 5, an OFDM-based channel sounding technique is presented in contrast to the previous technique. The OFDM-based channel sounder does not require dedicated sounding signal generation and signal processing, and hence, system complexity is reduced, and the sampling rate required is relatively low, since time domain spreading is not necessary. However, system performance is traded off for simplicity.

In Chapter 6, hardware and software implementation of the STDCC channel sounder is presented. Implementation issues due to hardware and software limita-

tions are also discussed. Indoor channel measurements were conducted in Nichols Hall, and measurement results were analyzed and studied.

The dissertation is concluded by future work and contributions in Chapter 7.

Chapter 2

Radio Propagation Channel

2.1 Fundamentals of Mobile Radio Channel

The mobile radio channel can be attributed to large-scale path loss channel and small-scale fading (multipath fading channel). Large-scale path loss is used to study electromagnetic wave propagation characteristics. As the name implies, the propagation model is usually used to predict the mean signal strength for an arbitrary transmitter-receiver separation. On the other hand, small-scale fading is used to describe the rapid fluctuations of amplitudes, phases, or multipath delays of a radio signal over a short period of time or travel distance, and hence the large-scale path loss effects may be neglected when studying small-scale fading channels. Unlike the deterministic feature of large-scale fading, small-scale fading is a stochastic process that depends on many factors. Figure 2.1 illustrates a simulated small-scale fading and the more gradual large-scale average signal strength variation versus transmitter-receiver separation. The average signal strength does not change rapidly for a relatively short distance, hence, for studying small-scale fading, the signal strength variations due to transmission distance is ignored.

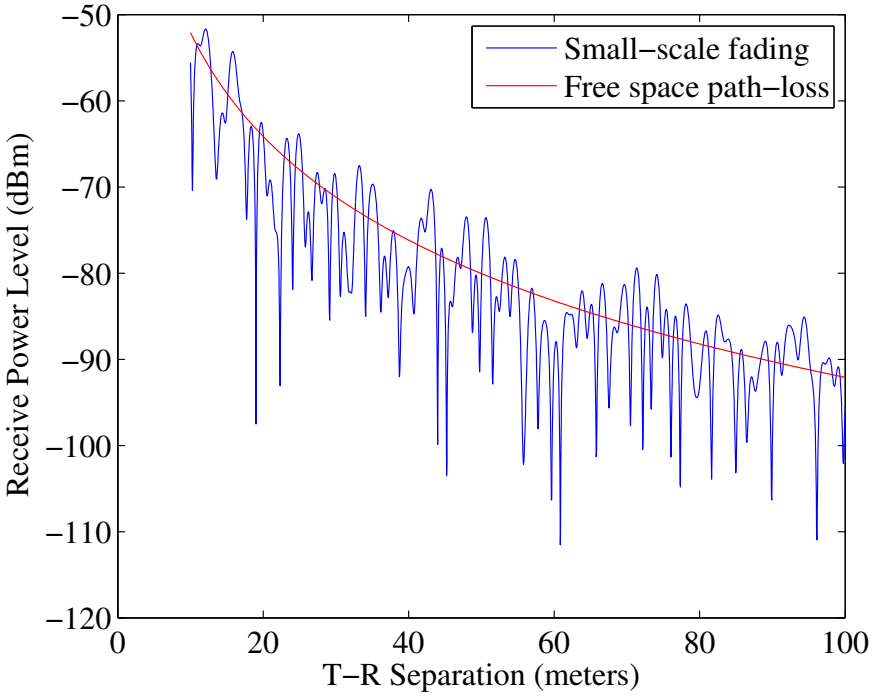

Figure 2.1. Small-scale and large-scale fading.

2.2 Multipath Fading Channel

Small-scale fading channel, sometimes referred to as multipath fading channel is a phenomenon caused by interference between multiple transmitted signals arriving at the receiver with random delays. The time-shifted versions of the transmitted signals are added up either constructively or destructively at the receiver, which causes both signal strength and phase fluctuation. In general, the causes of multipath fading can be summarized as:

- Transmitter movement
- Receiver movement
- Object movement

- Signal reflected by objects.

Depending on the speed and direction of the movement, the multipath fading channel is defined as fast and slow fading channel, which is characterized by Doppler shift [45]. Due to the random nature of the transmission channel, capturing and modeling such a channel environment can be difficult. In the following sections, the mobile radio channel is studied in three domains: temporal, frequency, and space, with each having its own parameters.

2.3 Time and Frequency Domain Characteristics

2.3.1 Delay Spread, Power Delay Profile and *rms* Delay Spread

Delay spread, power delay profile, and *rms* delay spread are the most important time domain characteristics of a wireless multipath fading channel. They are indicators of the type of the channel, i.e., indoor channel, or outdoor channel, and also frequency selective or nonselective. Let $x(t)$ represent the transmitted signal, $y(t)$ the received signal, and $h(t,\tau)$ the impulse response of the time-varying multipath fading channel. The variable t represents time variations due to motion, whereas τ represents the channel multipath delay for a fixed value of t. The received signal $y(t)$ can be expressed as a convolution of the transmitted signal $x(t)$ with the channel impulse response:

$$y(t) = \int_{\infty}^{-\infty} x(\tau) \cdot h(t,\tau) \cdot \mathrm{d}\tau = x(t) \otimes h(t,\tau). \tag{2.1}$$

In order to model the channel impulse response, the multipath delay has to be discrete, which means the delay axis τ is divided into equally spaced delay bins,

where each bin has a time delay width equal to $\tau_{i+1} - \tau_i = \Delta\tau$. If we ignore the propagation delay between the transmitter and the receiver, one can assume that the first multipath component has delay of zero, $\tau_0 = 0$. Let N be the total number of multipath components, so the *maximum excess delay* of the channel is given by $N\Delta\tau$. This channel is known as the tapped delay line model [46], which is shown in Figure 2.2:

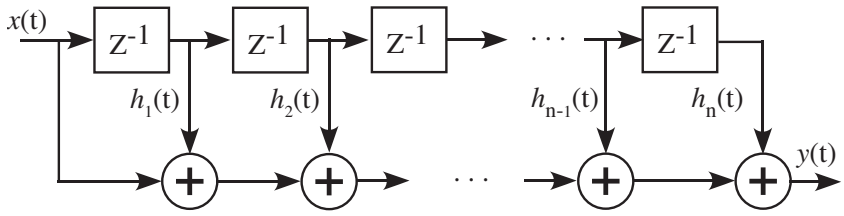

Figure 2.2. Tapped delay line model.

In general, the time-varying nature of the channel can be modeled as a *wide-sense stationary* (WSS) random process in the time variable t [47], and the attenuation and the phase shift associated with different delays are assumed to be uncorrelated, called the *uncorrelated scattering* (US) assumption [46, 47]. The autocorrelation function of the time-varying channel is defined as [46]:

$$R_{\tilde{c}}\left(\tau_1, \tau_2, \Delta t\right) = \mathrm{E}\left[\tilde{c}^*(\tau_1, t) \cdot \tilde{c}\left(\tau_2, t + \Delta t\right)\right], \tag{2.2}$$

where $R_{\tilde{c}}$ denotes the autocorrelation function of a WSS random process, $\mathrm{E}\left[\cdot\right]$ represents the expectation operator, and $\tilde{c}\left(\tau, t\right)$ describes the time-varying, complex lowpass-equivalent impulse response of the multipath fading channel. By applying the US assumption, Equation (2.2) becomes:

$$R_{\tilde{c}}\left(\tau_1, \tau_2, \Delta t\right) = R_{\tilde{c}}\left(\tau_1, \Delta t\right) \cdot \delta\left(\tau_1 - \tau_2\right). \tag{2.3}$$

Equation (2.3) indicates that the autocorrelation function depends only on the difference between τ_1 and τ_2. By replacing $\tau_1 - \tau_2$ with τ in the above equation, Equation (2.2) can be written as:

$$R_{\tilde{c}}(\tau, \Delta t) = \mathrm{E}\left[\tilde{c}^{*}(\tau, t) \cdot \tilde{c}(\tau, t + \Delta t)\right]. \tag{2.4}$$

Equation (2.4) is a time domain representation of the multipath fading channel. It indicates that the autocorrelation function of the channel can be derived from the expected value of the complex baseband impulse response. It would be helpful if there existed a function that can simultaneously provide both time and frequency domain description of the channel with respect to the delay variable τ and frequency domain variable ω. It is obvious that such a function can be obtained by applying the Fast Fourier Transform (FFT) on Δt, which yields:

$$S(\tau, \omega) = \mathbb{F}_{\Delta t}\left[R_{\tilde{c}}(\tau, \Delta t)\right] = \int_{-\infty}^{\infty} R_{\tilde{c}}(\tau, \Delta t) \cdot e^{-\jmath 2\pi\omega\Delta t} \cdot \mathrm{d}\Delta t, \tag{2.5}$$

where $\mathbb{F}[\cdot]$ denotes the Fourier transform with respect to Δt. Function $S(\tau, \omega)$ is defined as the *scattering function* of the channel, which is the Fourier transform of the channel autocorrelation function. Individually, the time and frequency domain parameters can also be derived from the scattering function.

The *power delay profile* (PDP) is defined as the intensity of a signal received through a multipath channel as a function of time delay. It can be calculated from the complex impulse response $\tilde{c}(\tau, t)$ [45]:

$$p(\tau) = \mathrm{E}\left[\mid \tilde{c}(\tau, t)^{2} \mid\right] = R_{\tilde{c}}(\tau, 0), \tag{2.6}$$

which is equal to the channel autocorrelation function evaluated at zero time instance, $R_{\tilde{c}}(\tau, \Delta t)\mid_{\Delta t=0}$. Assuming the scattering function is known, the power delay profile can be derived by averaging $S(\tau, \omega)$ over the frequency domain:

$$\begin{aligned}\int_{-\infty}^{\infty}\int_{-\infty}^{\infty} S(\tau,\omega) &= \int_{-\infty}^{\infty}\int_{-\infty}^{\infty} R_{\tilde{c}}(\tau,\Delta t)\cdot e^{-j2\pi\omega\Delta t}\cdot \mathrm{d}\Delta t\cdot \mathrm{d}\tau \\ &= R_{\tilde{c}}(\tau,0). \end{aligned} \tag{2.7}$$

Similarly, integrating the scattering function over the time domain yields the frequency domain representation, *Doppler spectrum*:

$$S(\omega) = \int_{-\infty}^{\infty} S(\tau,\omega)\cdot \mathrm{d}\tau. \tag{2.8}$$

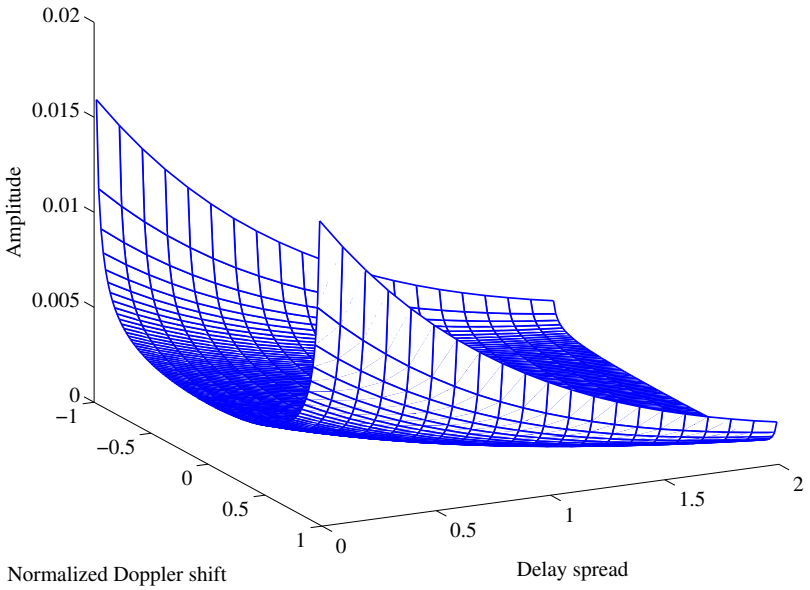

Figure 2.3. Doppler shift vs. delay spread.

Figure 2.3 demonstrates the relationship between the delay spread, the Doppler shift, and the amplitude of a multipath fading channel. The delay spread is modeled by the exponential function $e^{-\tau}$, where the Doppler spectrum is based on the Jakes model. The delay spread determines the bandwidth of the channel, and the Doppler spectrum reflects the velocity of the mobile.

The relationship between the scattering function $S(\tau, \omega)$ and the time and frequency domain functions is summarized in Figure 2.4:

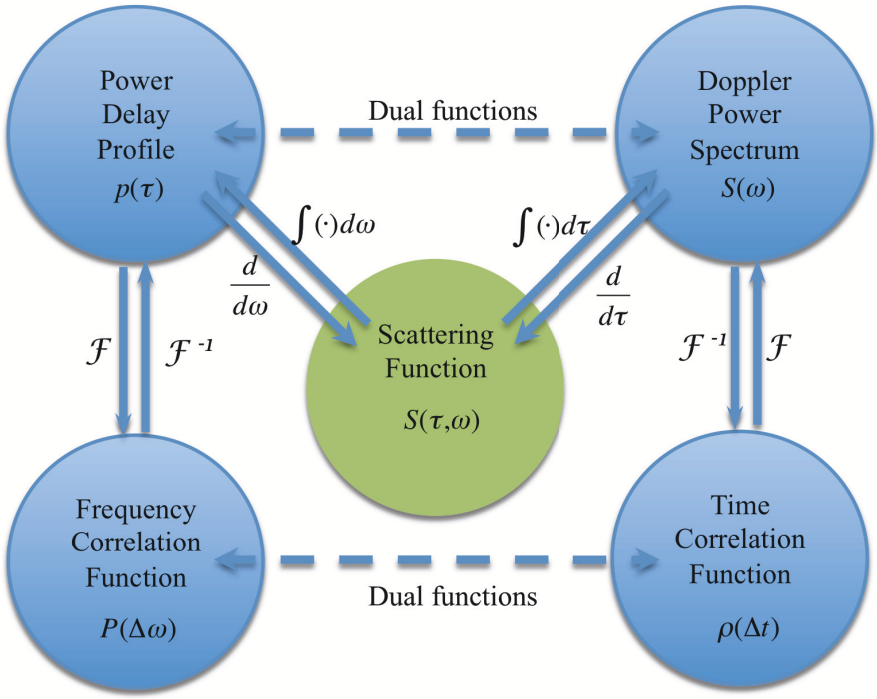

Figure 2.4. Relationship between scattering function, channel correlation functions, power delay profile, and Doppler power spectrum.

As shown in Figure 2.4, the time domain parameter power delay profile and the frequency domain parameter frequency correlation function are a Fourier Transform pair, so are the Doppler power spectrum and time correlation function. This relationship provides us an additional path to obtaining the channel parameter of one domain to another. Specifically, if one wants to get the frequency domain

channel parameter by using a time domain channel sounder, the FFT should be applied. Given the development of efficient FFT algorithms and digital signal processing (DSP) chips, implementing FFT on a hardware platform across all levels becomes cheap and feasible. Moreover, this relationship also provides a fundamental support of the OFDM-based channel sounder, which will be discussed in Chapter 5.

Channel delay spread and power delay profile are usually measured by using a channel sounding device. In order to compare different multipath channels and to develop general design guidelines for wireless systems, parameters such as *mean excess delay*, *rms delay spread*, and excess delay spread (X dB) are used. Those parameters are derived from a power delay profile. A often used parameter is *rms* delay spread, since the channel coherence bandwidth $B_c \approx \frac{1}{50\sigma_\tau}$ [46]. The *rms* delay spread is the square root of the second central moment of the power delay profile and it is defined to be [45]:

$$\sigma_\tau = \sqrt{\overline{\tau^2} - (\overline{\tau})^2}, \tag{2.9}$$

where

$$\overline{\tau^2} = \frac{\sum_k a_k^2 \cdot \tau_k^2}{\sum_k a_k^2} = \frac{\sum_k P(\tau_k) \cdot \tau_k^2}{\sum_k P(\tau_k)}. \tag{2.10}$$

2.4 Channel Coherence

2.4.1 Coherence versus Selectivity

Fading is a general term used to describe a wireless channel affected by some type of *selectivity*. A channel has selectivity if it varies as a function of either

time, frequency, or space. The opposite of selectivity is *coherence*. A channel has coherence if it does not change as a function of time, frequency, or space over a specified "window" of interest.

Indeed, wireless channels may be functions of time, frequency, and space. The most fundamental concept in channel modeling is classifying the three possible channel dependencies of time, frequency, and space as either coherent or selective in order to keep track of these dependencies in the wireless channel. As described in the previous sections, delay spread and channel coherence bandwidth are parameters which describe the time-dispersive nature of the channel. When the time-varying nature of the channel is caused by either relative motion between the mobile and base station, or by movement of objects in the channel. *Doppler spread* and *coherence time* are the parameters which describe the channel.

2.4.2 Temporal Coherence

A wireless channel has temporal coherence if the envelope of the unmodulated carrier wave does not change over a time window of interest. Mathematically, we express this condition in terms of a narrow band (no frequency dependence), fixed (no spatial dependence) channel, $\tilde{h}(t)$ [48]:

$$\left|\tilde{h}(t)\right| \approx V_0, \quad \text{for } |t - t_0| \leq \frac{T_c}{2}, \tag{2.11}$$

where V_0 is some constant voltage, T_c is the size of the time window of interest, and t_0 is some arbitrary moment in time. The largest value of T_c, on average, for which Equation (2.11) holds is called the "coherence time " and is the approximate time window over which the channel appears static.

Note that the channel in Equation (2.11) is in complex phasor form and is

independent of carrier frequency. Naturally, a transmitted wave will produce sinusoidal oscillations as a function of time, but the definition of temporal coherence is concerned with the "envelope" of those oscillations. Temporal coherence is an indication of how fast the channel response changes versus time, hence, the channel can be categorized into slow and fast fading. Slow and fast fading are relative to the transmit symbol rate. If the channel impulse response does not vary during one symbol period of the signal, the channel is considered as slow fading channel to the signal, and vice versa.

To overcome the fast fading effect, one can transmit a signal with higher symbol rate than the channel coherence time, that is, $T_c \leq T_s$, where T_c represents the channel coherence time, and T_s represents the symbol rate of the signal, so that the channel impulse response is flat over one symbol period. In general, in order to increase system throughput, we always transmit at high symbol rate. However, this approach results in frequency domain fading, which will be discussed in the next section.

2.4.3 Frequency Coherence

A wireless channel has frequency coherence if the magnitude of the carrier wave does not change over a frequency window of interest. This window of interest is the bandwidth of the transmitted signal. As we defined the time coherence of a radio channel, the condition of frequency coherence in terms of the static, fixed channel, $\tilde{h}(f)$ [48] is:

$$\left|\tilde{h}(f)\right| \approx V_0, \quad \text{for } |f_c - f| \leq \frac{B_c}{2}, \tag{2.12}$$

where V_0 is again some constant amplitude, B_c is the size of the frequency window of interest, and f_c is the center carrier frequency.

The frequency coherence characteristic is described by the frequency correlation function $P(\Delta f)$, which represents the correlation between the channel response to two narrowband signals with the frequencies f_1 and f_2. Channel coherence bandwidth, B_c, is a statistical measure of the range of frequencies over which the channel can pass all spectral components with approximately equal power and linear phase. Channel coherence bandwidth reflects the correlation between two frequency components across the frequency range of interest. Hence, the correlation coefficient determines the coherence bandwidth. The greater the correlation coefficient, the narrower the coherence bandwidth. Assuming that the correlation between two frequency responses depends only on the frequency difference, that is $\Delta f = f_1 - f_2$, the normalized frequency correlation coefficient is then defined as:

$$\rho_{\Delta f} = \frac{\mathrm{E}\left[H\left(f\right) \cdot H\left(f + \Delta f\right)^*\right]}{\mathrm{E}\left[\left|H\left(f\right)\right|^2\right]}. \tag{2.13}$$

The frequency correlation function can be thought of as the transfer function of the channel; hence, it is the inverse Fourier Transform of the channel impulse response, and as a result, Δf can be represented as: [46]:

$$\Delta f \approx \frac{1}{\tau_{\max}}, \tag{2.14}$$

Equation (2.14) reveals the relationship between the power delay profile and the frequency correlation function, that is, they are Fourier transform pairs. However, a general relationship between the coherence bandwidth and *rms* delay spread only exists for the specific channel models and must be derived from the actual

dispersion characteristics of the channels or statistical measurements and simulation [45].

As mentioned in the previous section, transmitting a signal at high symbol rate requires larger bandwidth, and hence if the channel coherence bandwidth is smaller compared with the signal bandwidth, the received signal suffers from frequency selectivity. Many techniques are available to compensate for the fading effects caused by frequency selectivity, one classic example being equalization. Equalization is achieved by estimating the channel frequency response from the distorted signal with various combining techniques [46]. Although equalization can assist in improving signal quality and reducing bit error rate, it requires complicated equalizer design at the receiver. When a communication system is to be operated in a certain wireless environment, the channel characteristics need to be acknowledged by performing channel sounding, which provides prior information of the radio channel to the communication system designer.

2.5 Radio Channel Characteristics of the Dynamic Spectrum Access Network Environment

As discussed in the previous sections, the characteristics of a radio channel depend on many factors. Researchers have addressed factors that affect these characteristics in both time and frequency domains. However, as the DSA network comes into play, the radio channel can behave differently. For example, the channel bandwidth can change from several megahertz to several hundred megahertz when then channel type changes from outdoor to indoor. This phenomenon is caused by the random access of the unlicensed users. In particular, the unlicensed users

can appear at a certain frequency band at any time as long as their activities are legitimate. Figure 2.5 shows an example of the random access of unlicensed user under licensed and unlicensed bands. The figure uses color scale to represent

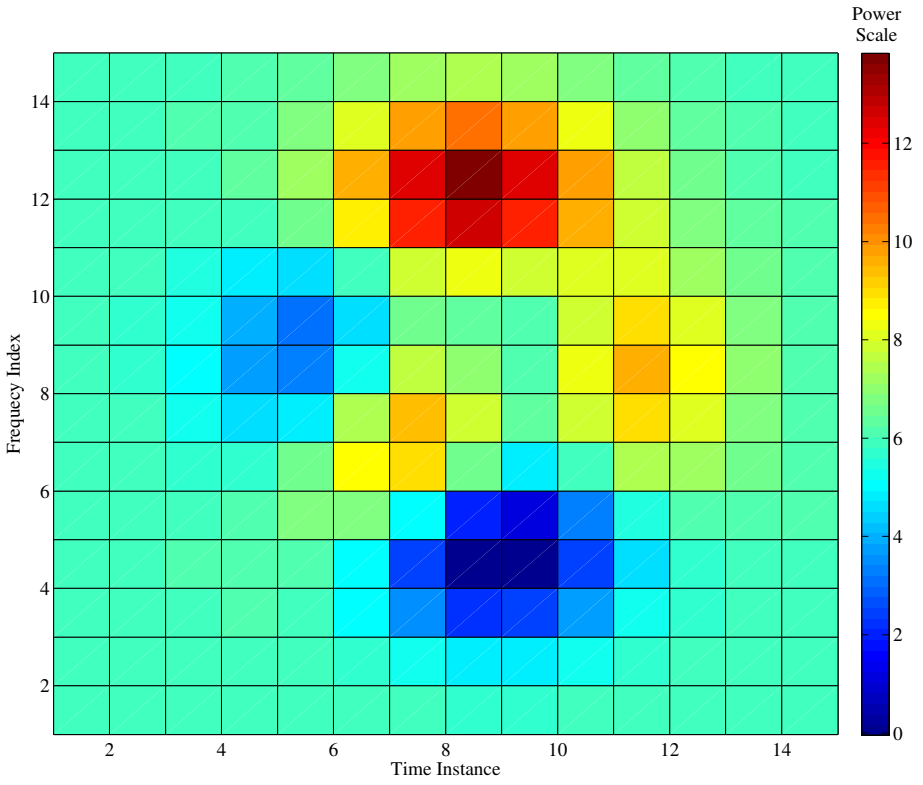

Figure 2.5. Example of an unlicensed user appearing in a DSA network environment.

the transmit power level of a certain user in both time and frequency domains. Zero on the power scale (in dark blue) shows that the slots are inaccessible by the unlicensed user due to primary user reservation or power restriction. Different color stands for different power level restrictions. In the time domain (x-axis in the figure), the unlicensed user may occupy a certain band for a period of time until the licensed users appear or other unlicensed users request to share the band. That unlicensed user either has to wait until the band is available again, or hop

to another frequency band. This approach is suitable for applications that are latency sensitive, such as file transfer, peer-to-peer, etc. Switching to a different frequency band will guarantee continuity of connection at the cost of hardware complexity, since the RF front end has to have the capability to switch between center frequencies as well as be accommodative to different bandwidths.

The Unlicensed National Information Infrastructure (U-NII) radio bands and the Industrial, Scientific and Medical (ISM) radio bands are two commonly used unlicensed bands (IEEE 802.11), which cover a wide range of frequencies. Table 2.1 lists the transmission parameters for each frequency range of the ISM and U-NII bands.

Table 2.1. U-NII and ISM band specifications.

	U-NII[a]				ISM[b]
	Low	Mid	Worldwide	Upper	ISM
Band (GHz)	5.15-5.25	5.25-5.35	5.47-5.725	5.725-5.825	2.4-2.5
Power Limit	50 mW	250 mW	250 mW	1 W	Varies

[a]U-NII is an FCC regulatory domain for 5 GHz wireless device, for complete reference please see reference [49].

[b]ISM bands listed here only indicate the most commonly used bands (WiFi band). The complete ISM band definition can be found in [50].

For a cognitive radio device to operate in the frequency bands listed in Table 2.1, not only must the device RF front end have the ability to tune accordingly, but also the radio channel characteristics must vary as well. For example, the maximum Doppler shifts for a device operating at 5.15 and 5.85 GHz with velocity of 25 M/h are equal to 429.17 Hz and 487.5 Hz, respectively. In addition, the user bandwidth may change according to the center frequency and maximum bandwidth available. Hence, the user signal may suffer from different multipath fading

channels. For example, if the user signal bandwidth changes from 5 MHz to 500 KHz, and the channel coherence bandwidth remains 2 MHz, the multipath fading channel for the user changes from frequency selective to frequency nonselective, and it may change over time and frequency. This challenge requires cognitive radios to have the ability to learn the radio channel and adjust their parameters rapidly and adaptively before the radio channel changes.

In addition to the frequency and bandwidth restrictions, operating environment also plays a critical role in cognitive radio design. For an indoor environment, the radio channel may be a frequency selective channel for the communication system, while frequency nonselective when being operated outdoors. This is because of the change in the maximum delay spread, which results in channel bandwidth change. Moreover, the path loss factor varies from indoor to outdoor as well as different channel models. Some devices may work for an indoor environment but not for outdoors due to the change in channel type. In Chapter 6, channel sounding experiments will be discussed in detail, the experiment results for both indoors and outdoors will be shown. Briefly speaking, the USRP with 2.4 GHz daughterboard works well for indoor applications. However, it fails to perform channel sounding measurements for outdoor wireless channels.

2.6 Chapter Summary

In this chapter, conventional radio channel characteristics are presented with focus on the time and frequency coherence of the multipath channel, since they are the fundamentals of the signal processing portion of channel sounding techniques. The relationship between time and frequency domain multipath channel characteristics are presented in Figure 2.5. This relationship diagram reveals how the

parameters are interwoven together by the Fourier Transform. Key factors affecting cognitive radio design are described, such as center frequency, user bandwidth, velocity, and operating environment. Due to the network environment in which cognitive radios are operated, channel sounding becomes especially critical, and yet difficult to accomplish. Furthermore, the challenges to performing channel sounding in a DSA network environment become the motivation of the research. How to perform channel sounding efficiently, frequently, and quietly is to be answered in the following chapters.

Chapter 3

Channel Sounding Techniques

Channel sounding is a technique that transmits a known signal to excite the channel and observes the signal variations in amplitude and phase at the receiver. It enables us to study and understand the radio channel characteristics. Early channel sounding systems send a single tone (unmodulated CW carrier) to excite the channel, and variations in power and phase are measured with a moving or a stationary receiver. This is referred to as a *narrow-band sounding* technique [11]. When considering multipath fading channels, where two frequencies are correlated, narrow-band sounding techniques become inefficient and impractical since a single tone has to be transmitted at various frequencies of interest to be able to capture the frequency and time coherence behavior of the channel [11].

In this section, a literature survey of existing channel sounding techniques is provided, with the problems associated with each technique described. A widely used technique, called STDCC, is emphasized.

3.1 Radio Channel Sounding

Radio channel sounding techniques, in general, can be categorized into narrowband and wideband sounding techniques, depending upon the transmit bandwidth [11, 51]. Modern radio communication systems, such as WiFi and WiMax, are normally operated in a wideband channel environment, where the desired signal is in the presence of several delayed versions of itself with random fading in amplitude and phase offset. It can also be divided into time and frequency domain channel sounding, where the time domain sounding is in the interest of capturing the channel impulse response, and the frequency domain sounding aims to capture the frequency characteristics of the channel. Depending on the domain of interest, the channel sounder design of the sounding signal and sounder structure can be different. However, the time and frequency domain parameters are closely related to each other, with several parameters being interderivable. For example, the frequency correlation function can be obtained from a time domain channel sounder by applying the Fast Fourier Transform (FFT) on the channel impulse response. However, this operation requires additional processing. The frequency domain measurement can also be obtained by using coherent measurement techniques [52].

In order to capture the wideband channel parameters, such as the root mean square (RMS) delay spread, the maximum delay spread, and the coherence bandwidth, a sounding signal occupying wide bandwidth is required. Carrying out narrowband measurements at a large range of frequencies of interest is expensive in terms of hardware complexity, moreover the performance is limited by the interference and hardware, since the hardware may be designed for a particular

center frequency, which may not be used for the others. Several wideband channel sounding techniques have been devised, based on the periodic short duration pulse approach, and the pulse compression technique [11]. Pulse compression-based techniques, depending on different receiver structures, are realized by matched filter or cross correlation. Both methods will be discussed in details in the following sections.

3.2 Periodic Pulse Channel Sounding

The principle behind the periodic pulse sounding technique is that a narrow (short duration) pseudo-impulse is periodically transmitted to excite the channel (Figure 3.1), and the signal attenuation is measured by an envelop detector. The impulse must be sufficiently narrow to ensure that the signal bandwidth is larger than the channel coherence bandwidth to capture all the echoes. On the other hand, two adjacent pulses have to be close enough observe the time-varying behavior of each echo.

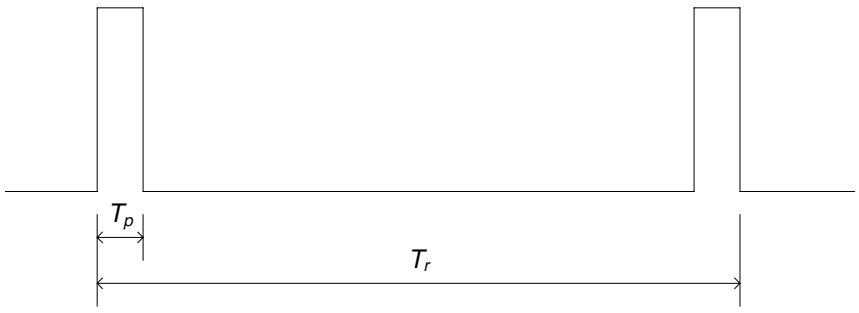

Figure 3.1. Periodic pulse sounding signal.

In Figure 3.1, T_p is the pulse duration, which represents the minimum identifiable delay path resolution, and T_r is the pulse repetition period that is equal to

the maximum resolvable delay path. Each short pulse provides a 'snapshot' of the multipath channel at a certain time instance. Combining a series of repetitions of pulses together gives the channel behavior over the measurement duration.

The pulse sounding technique uses an envelope detection technique, which means only the amplitude variations are recorded, and phase information is discarded. Theoretically, the narrow pulse sounding technique is an ideal technique if the pulse duration approaches zero, since the delay resolution is infinitely small. However, the pulse sounding technique requires high unit transmit power to detect weak signals, since all the energy is contained within the narrow pulse. High peak-to-average power ratio (PAPR) is one of the major drawbacks of this technique, since it requires a large dynamic range of the transmit power amplifier in order to guarantee accurate measurements. The cognitive radio and DSA enabled devices are generally portable and compact, and large power consumption and high sampling rate are avoided. The narrow pulse sounder is disqualified without further modification.

3.3 Frequency Domain Channel Sounder: Chirp Sounder

As an alternative to the time domain channel sounder, we can estimate the transfer function instead by using the chirp sounder. The main criterion for its design is that is has a power spectrum $|P(j\omega)|^2$, which is approximately constant in the bandwidth of interest, and it allows interpretation of the measurement result directly in the frequency domain. The time domain transmit waveform is given as:

$$p(t) = \exp\left[2\pi j\left(f_0 t + \Delta f \frac{t^2}{2T_{\text{chirp}}}\right)\right] \quad 0 \le t \le T_{\text{chirp}}, \tag{3.1}$$

consequently, the instantaneous frequency is:

$$f_0 + \Delta f \frac{t}{T_{\text{chirp}}}, \tag{3.2}$$

and thus has a linear relationship with time. The receiver filter requires a matched filter to extract the transfer function. Intuitively, the chirp filter "sweeps" through frequency range of interest, measuring different frequencies at different times. We can improve the the sounding efficiency by performing measurement on different frequencies at the same time. However, due to hardware costs, calibration issues, etc., analog generation of $p(t)$ using multiple oscillators to generate multiple frequencies is not practical. Generating such signals digitally seems feasible, since only a single oscillator is required, and the signal can be upconverted to the desired passband.

3.4 Pulse Compression

The pulse compression is based on the theory of linear systems [11, 53]. It provides a way to reduce the sampling rate by compressing the wideband signal bandwidth. The measurement time is increased as a tradeoff due to the extra processing time of pulse compression. If we consider the white noise $n(t)$ as the input to a linear system with impulse response of $h(t)$, the output signal $s(t)$ is the convolution of $n(t)$ and $h(t)$:

$$s(t) = \int h(\tau) \cdot n(t - \tau) \mathrm{d}\tau. \tag{3.3}$$

If the output signal $s(t)$ is cross correlated with a delayed version of the input, the resulting cross correlation coefficient is proportional to the impulse response of the system $h(\tau)$:

$$\begin{aligned} E\left[s\left(t\right)\cdot n^{*}\left(t-\tau\right)\right] &= E\left[\int h(\xi)\cdot n(t-\xi)\cdot n^{*}(t-\tau)\mathrm{d}\xi\right] \\ &= \int h\left(\xi\right)\cdot R_{\mathrm{n}}\left(\tau-\xi\right)\mathrm{d}\xi, \end{aligned} \tag{3.4}$$

where $R_{\mathrm{n}}(\tau)$ is the autocorrelation function of white noise $n(\tau)$, which is equal to the single-sided noise power spectral density, N_0. Hence, Equation (3.4) can be expressed as:

$$E\left[s\left(t\right)\cdot n^{*}\left(t-\tau\right)\right] = N_0\cdot h\left(\tau\right). \tag{3.5}$$

Equation (3.5) indicates that the impulse response of a linear system can be obtained using white noise as the input, and correlation technique. Generating white noise is unrealistic in practical applications. However, pseudo-random (PN) sequences have been studied and researched due to its noise-like characteristic [54]. To be explicit, the autocorrelation and cross correlation functions of the maximum length PN sequence (m-sequence) are periodic and binary valued, and the m-sequence is easy to generate with the linear shift feedback registers (LSFR). The m-sequence is also balanced, meaning that the number of ones is one greater than the number of zeros in each period of the sequence, which can limit the degree of carrier suppression [55]. Another advantage of using PN sequences is the inherent processing gain achieved by the cross correlation process, which will be discussed in detail in Section 3.5.2.2.

3.4.1 Convolution Matched Filter

The convolution matched filter technique falls into the pulse compression category. It uses a filter that matches the sounding signal to achieve pulse compression. A commonly used matched filter is the surface acoustic wave (SAW) filter. The SAW filter on the receive side is matched to the transmit m-sequence, which reduces the hardware cost of the system, since it eliminates the generation of the identical m-sequence at the receiver. The output of the matched filter is a series of snapshots of channel impulse responses, which allows the system to operate in real time [11]. However, the performance of the SAW filter is limited by the devices. When the m-sequence length is long, it is difficult to generate spurious acoustic signals. Imperfect surface acoustic waves degrade the sounder performance in terms of delay resolution and dynamic range [53]. Some other effects can also cause sensitivity degradation, such as temperature, filter materials, etc. In general, SAW filters are designed for a particular center frequency with a certain bandwidth. The hardware cost constrains the application of SAW filters in DSA networks, where operation frequency and bandwidth may change in random manners.

3.5 The STDCC Technique

The STDCC channel sounding technique is the most widely used technique by researchers and industry due to the outstanding features [4, 11, 53]. First, it can perform channel sounding over a wide bandwidth, which is suitable for modern wideband communications. Second, it reduces the sampling rate at the receiver compared with the matched filter and chirp sounders. Matched filter and chirp

sounder require sampling at the Nyquist rate where the STDCC only uses a single sample at the maximum of the autocorrelation function. Third, the STDCC does not suffer from high PAPR, because of the use of the spread spectrum technique. Last but not least, signal processing can either be done by the hardware or software depending on the requirement. If realtime channel sounding is required, the signal processing algorithms can be uploaded to the FPGA, so that realtime channel impulse responses can be observed. Off-line signal processing saves expense on board memory, and one can develop complicated signal processing algorithms to obtain better channel sounding performance.

3.5.1 Overview

The STDCC is based on the sliding correlator theory [4]. It is simple to implement and does not require a high sampling rate compared with conventional correlative channel sounders [11]. Conventional correlative channel sounders sample at the Nyquist rate, while the STDCC takes one sample value for each m-sequence at the maximum amplitude of the autocorrelation function. The position of the maximum peak of the autocorrelation function changes for each transmission cycle of the m-sequence. STDCC pulse compression is done by correlating the received sequence with an identical sequence clocked at a slightly lower rate. The difference in chip rate is called *slip rate*, which is defined as:

$$f_{\text{slip}} = f_{\text{Tx}} - f_{\text{Rx}}. \tag{3.6}$$

The difference in chip rate results in different time bases between the transmitted and the received sequences. The slower sequence (received sequence) will be

aligned with the transmitted sequence again after a duration:

$$T_{\text{slip}} = \frac{1}{f_{\text{slip}}}. \tag{3.7}$$

The time domain representation, K_{scale} gives us the number of samples for a single impulse response $h(\tau_i)$, and it is defined as:

$$K_{\text{scale}} = \frac{f_{\text{Tx}}}{f_{\text{slip}}} >> 1, \tag{3.8}$$

the larger the number of samples, the better the delay resolution. On the down side, the measurement duration is also increased by a factor of K_{scale}. The trade-off between measurement time and delay resolution needs to be considered for different radio channel environments. However, the *sliding correlator* can be substituted by a stepping correlator [40,56,57] in order to use digital signal processing techniques for improving the system performance. The STDCC transmitter and receiver schematics are shown in Figure 3.2. The schematic shown in Figure 3.2 is oversimplified, as it does not contain all the components, for example the intermediate frequency (IF) stage. The IF frequency at the transmitter employed by Cox is 10 MHz [3]. Both the Kansas University agile radio (KUAR) [58] and universal software radio peripheral (USRP) offer baseband bandwidth greater than 10 MHz. For the implementation consideration, we do not have to have the IF block as long as the sounding signal bandwidth is less than the maximum baseband bandwidth that the hardware can offer. The transmitter consists of a Pseudo-random Binary Sequence (PRBS) and a Radio Frequency (RF) end. An m-sequence generator is driven by a local clock with varying clock rate depending on the requirement. The m-sequence is then modulated and fed into the RF end and transmitted. At the

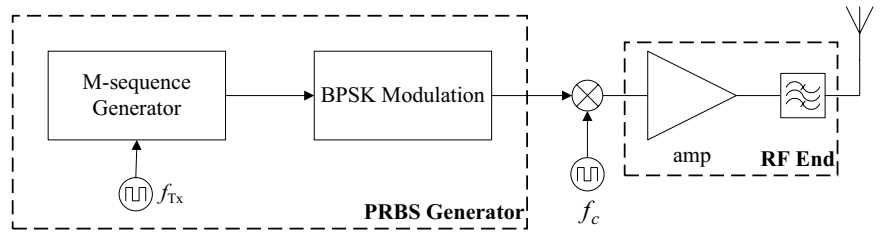

(a) STDCC Transmitter

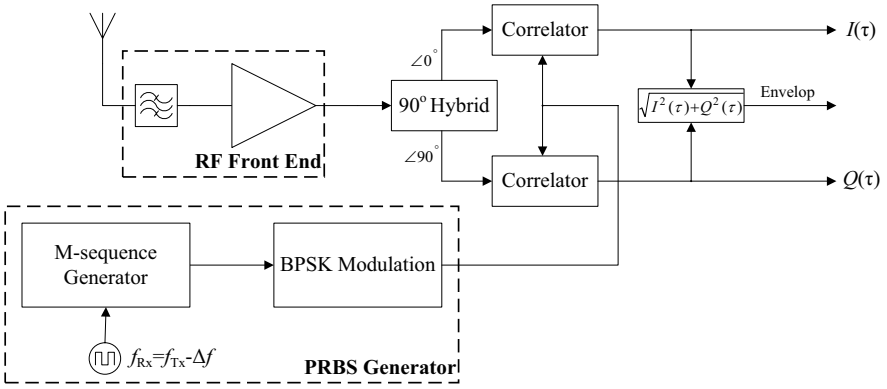

(b) STDCC Receiver

Figure 3.2. Schematic of the STDCC transceiver.

receiver end, the received signal is filtered and passed through a low noise amplifier (LNA), the inphase (I) and the quadrature (Q) of the signal are individually correlated with an identical PRBS signal except that the m-sequence generator is clocked at a slightly lower rate. The schematic shown previously provides a full hardware implementation of the STDCC. If a software and hardware hybrid implementation is used, anything beyond the RF front end can be implemented in the software to minimize the hardware scale.

3.5.2 System Parameters

In this section, several critical system parameters of the STDCC channel sounder are presented. The relationship between the parameters and the system

performance is addressed.

3.5.2.1 Multipath Resolution

The multipath resolution capability of the channel sounder is summarized as: *the maximum delay resolution* and *the minimum identifiable multipath resolution*.

The maximum delay resolution is defined as the capability to detect the maximum unambiguous multipath component by the sounder, which is a function of the m-sequence length. The maximum path delay that can be measured by the sounder is smaller than L/R_c, where R_c is the m-sequence clock rate, and L is the sequence length (in chips). The sequence period L/R_c has to be greater than the $\tau_{\max}$ to ensure that no echoes are neglected.

The minimum identifiable multipath resolution is the difference between two adjacent multipath components, and it is a function of the m-sequence chip rate as well as the slip rate f_{slip}.

3.5.2.2 Dynamic Range

The dynamic range, in decibels, is defined as the ratio of the magnitude of the correlation peak and the magnitude of the maximum spurious correlation value:

$$\text{DR} = 10 \log_{10}(L^2), \tag{3.9}$$

where L is the m-sequence length [53]. It represents the ability to detect weak signals. The ideal dynamic range for m-sequence with L varying from 127 to 2047 is shown in Table 3.1. For an AWGN channel, the dynamic range can be represented as the ratio of the peak power level and the noise power level, and as

Table 3.1. Ideal dynamic range of m-sequence.

Sequence Length L	Dynamic range (dB)
127	41.1
255	48.1
511	54.2
1023	60.2
2047	66.2

a result, Equation (3.1) becomes:

$$\mathrm{DR}_{\mathrm{AWGN}} = 10 \log_{10} \left(\frac{L^2}{N_0 B} \right), \tag{3.10}$$

where N_0 denotes the noise power spectral density, and B is the bandwidth of the m-sequence.

The correlation process at the receiver provides a processing gain[1] (similar to the Code Division Multiplexing Access (CDMA) system), which means the dynamic range of the estimated impulse responses is better than the signal-to-noise ratio (SNR) observed at the receiver end [59]. However, the dynamic range is restricted by several factors, such as system noise, power amplifier nonlinearities, and the chip rate difference. The difference in chip rate introduces autocorrelation function distortion, which means the maximum value of the autocorrelation function is inversely proportional to f_{slip}. A small value of f_{slip} leads to a longer measurement duration, but better delay resolution. Cox notes that $K_{\mathrm{scale}} = 5000$ produces a good correlation with minor distortion, whereas distortion is consider-

[1]The processing gain in decibels is defined as: $10 \log_{10} N$, where N is the spreading sequence length.

able when $K_{\text{scale}} = 1000$ [3]. Martin discusses the relationship between achievable dynamic range and correlation noise by using a novel sliding correlation algorithm in the correlation process, and quantifies dynamic range as a function of the ratio of K_{scale} (time scaling factor) and L (the m-sequence length). This contribution provides us a systematic method of designing sliding correlators [38].

3.5.2.3 Time Scaling Factor

As mentioned in the previous section, a large time scaling factor provides good minimum identifiable delay performance and minimum distortion, but also results in longer correlation time and larger memory sizes to store the data. The choice of the time scaling factor is dependent only on the requirement and channel environment. For example, for outdoor channel sounding, the number of reflected paths and maximum delay are substantially larger than those of indoor environments, but the minimum delay is on the order of microseconds. Such an radio channel would require a channel sounder with longer sounding sequences, and slower chip rate and vice versa for an indoor channel. However, both outdoor and indoor channel sounding always need a larger dynamic range, which is directly related to the sequence length.

3.5.2.4 Doppler-shift Resolution

The Doppler-shift resolution is a function of the transmitter and receiver velocity (v), carrier frequency (f_c), m-sequence length (L), clock rate (τ_c), and time scaling factor (K_{scale}). The relationship between these values can be summarized as follows:

- Maximum Doppler shift experienced by a moving receiver with velocity v is:

$$f_{\mathrm{D}} = \frac{v \cdot f_{\mathrm{c}}}{c}, \tag{3.11}$$

  where $c = 3 \times 10^8 m/s$ is the free space velocity of electromagnetic waves.

- The maximum Doppler shift that can be measured by STDCC is given by:

$$f_{\mathrm{D}} = \frac{1}{2K_{\mathrm{scale}} \cdot L \cdot \tau_{\mathrm{c}}}. \tag{3.12}$$

  Inserting Equation (3.12) into Equation (3.11) yields:

$$v = \frac{c}{2K_{\mathrm{scale}} \cdot L \cdot \tau_{\mathrm{c}} \cdot f_{\mathrm{c}}}. \tag{3.13}$$

  Equation (3.13) indicates that v is inversely proportional to the m-sequence length for fixed K_{scale}, τ_c, and f_c:

$$v \propto \frac{1}{L}. \tag{3.14}$$

The derivation above leads to a new problem of finding the tradeoff between delay resolution and Doppler-shift resolution. Longer m-sequence provides better minimum identifiable delay resolution, but sacrifices the Doppler-shift resolution. For situations in which both transmitter and receiver are stationary, the Doppler-shift resolution can be ignored, such that better dynamic range performance can be achieved.

3.6 Frequency Domain Characterization

The frequency correlation function is a measure of the correlation between two spaced carrier frequencies. This function is generated from the values of $P(\tau_i)$ through FFT techniques [60]. The coherence bandwidth, defined as the maximum frequency difference for which two signals have a specified value of correlation, is a frequency domain parameter that is used for assessing the performance of various modulation or diversity techniques. No definitive value of correlation has been established for the specification of coherence bandwidth. However, channel coherence bandwidth values of 0.9 ($B_{0.9}$) and 0.5 ($B_{0.5}$) are the two most widely used values [45]. The resolution in the frequency domain, however, is related to the pulse repetition frequency (PRF) of the spread spectrum sounding signal, which is defined as:

$$\text{PRF} = \frac{1}{L\tau_0}, \tag{3.15}$$

e.g., for $L = 127$ and $\tau_0 = 0.1$ μs, the PRF is 78.74 kHz. If the frequency resolution is not sufficient, detail may be lost in the estimation of the frequency correlation function resulting in erroneous values for $B_{0.9}$ and $B_{0.5}$. In essence, this is the same problem that afflicts the spaced-tone sounding techniques.

One obvious method of counteracting this problem is to increase the length of the m-sequence, thereby maintaining the same time resolution. However, the drawback for adopting this approach, as discussed previously, limits the maximum practical value of m.

An alternative and more elegant solution has been proposed by Haese [20]. Since it is assumed that all distinguishable echoes in the power-delay profile occur within a certain time delay window, if the length of the m-sequence is doubled,

the new power-delay profile will contain exactly the same information up to a delay of 12.7 μs with only the system noise floor extending to 25.4 μs. However, the frequency resolution capability will improve from 78.74 kHz to 39.37 kHz. In practice, therefore, the frequency resolution capability can be improved by increasing the length of the time delay window off-line, i.e., after completion of the field trials, by taking the system noise floor and extending it in time, prior to using the FFT.

As opposed to the case where m is increased, the only penalty of increasing the length of the time delay window off-line is the increased time of computation.

3.7 Chapter Summary

In this chapter, an overview of the radio channel sounding techniques is provided. Both the advantages and disadvantages of each technique were outlined. The reasons why the STDCC channel sounding technique is chosen as the prototype technique for DSA networks are addressed. The swept time-delay cross correlation technique was emphasized, system parameters were discussed from a design point of view. The inherent processing gain makes STDCC the nearest to optimum sounding technique for DSA networks. However, some necessary modifications to the STDCC systems are required before applying to DSA networks, such as transmit power, sounding efficiency, which will be discussed more in detail in later chapters.

Chapter 4

Multi-carrier Swept Time Delay Cross Correlation Channel Sounder

Multicarrier modulation (MCM) techniques are promising candidates for DSA networks due to their spectrum utilization efficiency and robustness. Two major types of MCM techniques are Orthogonal Frequency Division Multiplexing (OFDM) and Multicarrier Code Division Multiple Access (MC-CDMA). For each type, there are many different versions in terms of implementation, especially for the MC-CDMA systems. Depending on how the spreading is achieved, MC-CDMA systems can be divided into Multicarrier Direct Sequence Code Division Multiple Access (MC-DS-CDMA) and MC-CDMA (in general). If the spreading is performed in the time domain, the system is called MC-DS-CDMA, while in contrast, the system is named MC-CDMA for frequency domain spreading.

Both systems have their own advantages and disadvantages, which have been

fully studied in [61]. The motivation of collaborating multicarrier system and STDCC system is to improve the channel sounding efficiency, since with MCM techniques, one can operate at different center frequencies simultaneously. In addition, a Direct Sequence (DS) technique allows us to change the signal power by varying the spreading sequence length. This property fits in the DSA network perfectly, where secondary users can only have access to certain bands at certain time with limited power based on FCC regulations.

In this chapter, a novel channel sounding technique, named MC-DS-STDCC, is introduced, starting by a brief introduction to the MC-DS-CDMA system, and followed by the MC-DS-STDCC system structure. A comparison study between conventional STDCC and MC-DS-STDCC is conducted, including simulation results on channel sounding performance and mathematical analysis. Further issues of the MC-DS-STDCC is addressed.

4.1 MC-DS-CDMA System

In this dissertation, the MC-DS-CDMA system is not only considered as a data transmission system, but also as a platform for the STDCC technique. Figure 4.1 shows the MC-DS-CDMA transceiver block diagrams.

In Figure 4.1, $x(t)$ and $s(t)$ stand for the input and output signal of the transmitter. Similarly, $x'(t)$ and $s'(t)$ are the input and the output of the receiver. N represents the total number of subcarriers, which is also the FFT size. T_0 is the input signal $x(t)$ symbol duration, $C_i, i = 1 \dots N$ is the spreading code space, and the codes do not have to be orthogonal in this case, since the time domain signal is not summed up before transmit. The value $M_i, i = 1 \dots N$, represents the length of each individual spreading sequence. Generally, they all have the same length,

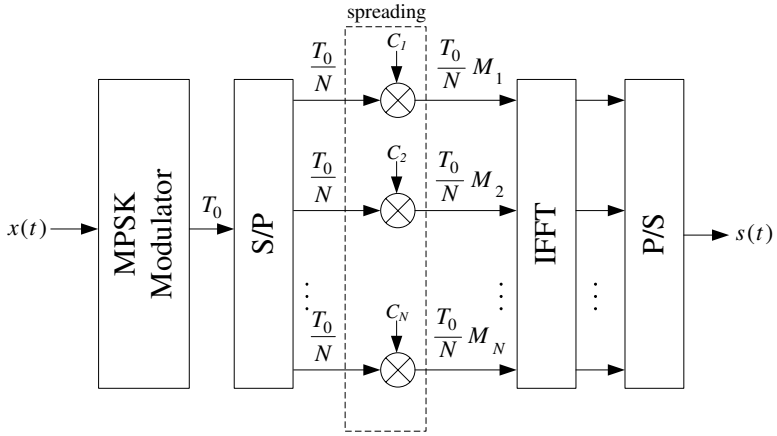

(a) MC-CDMA Transmitter

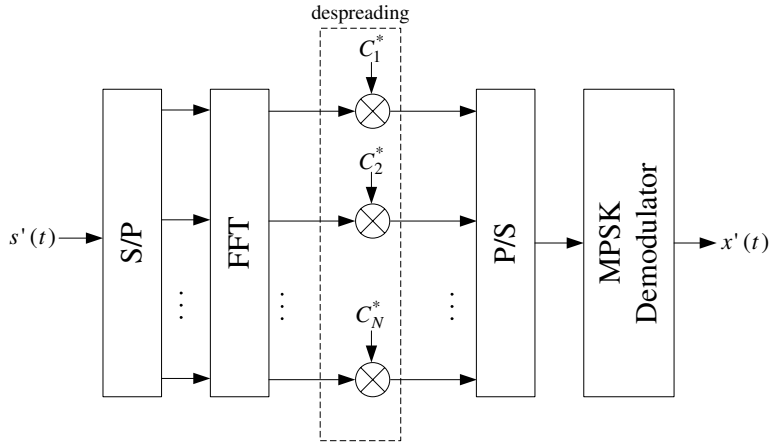

(b) MC-CDMA Receiver

Figure 4.1. MC-CDMA transceiver.

but it is possible to use various length spreading sequences to achieve signal power adjustment for each subcarrier.

On the transmitter side, a serial data sequence is first M-PSK modulated and then converted into parallel before being fed into the spreading and the inverse fast Fourier Transform (IFFT) blocks. After serial to parallel (S/P) conversion, data on each subcarrier is multiplied with corresponding spreading sequence, C_i, and then the signal on individual subcarrier is modulated onto different carrier

frequencies by the IFFT. The parallel signal is serialized and transmitted. The receiver performs the reverse operation, except that the despreading process uses the complex conjugate version of the spreading sequence. The schematic does not include *Cyclic Prefix* (CP) block, which is used to eliminate the effects of Inter-Symbol Interference (ISI). Since we are employing the MC-DS-CDMA system as a channel sounding system, we are interested in capturing the entire channel behavior. Thus, we do not employ CP, since all the channel information is contained in the distorted signal.

4.2 Combined STDCC MC-DS-CDMA Implementation

The proposed technique employs multicarrier direct sequence spread spectrum modulation and STDCC channel sounding to tailor the channel sounding signal transmit power level across frequency, thus minimizing the amount of interference introduced per subband. Each subcarrier in an MC-DS-CDMA system is considered as a branch, on which a complete STDCC system is operating. The system is similar to a conventional MC-DS-CDMA system, except some changes are made to integrate the STDCC system. MC-CDMA systems have various implementations depending on which domain the spreading is performed. Time domain spreading can minimize the interference caused to other subcarriers and users at cost of high sampling rate. Frequency domain spreading enhances the immunity to frequency errors, which is critical to any type of multicarrier system. Since reducing interference to the interference tolerance of other users is one of our main objectives, the MC-DS-CDMA system is selected to be collaborated with the STDCC channel sounding technique. The transmitter and receiver block diagrams are illustrated in Figure 4.2.

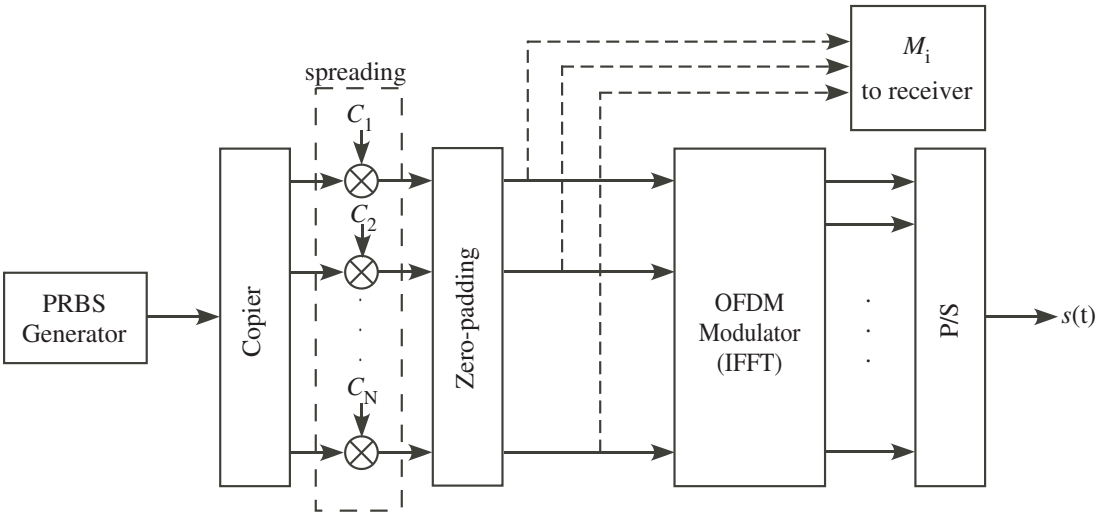

(a) MC-DS-STDCC Transmitter

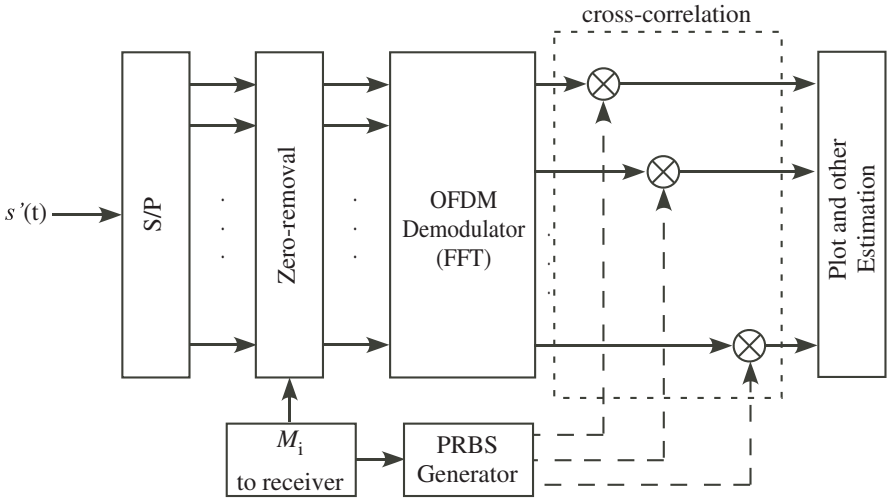

(b) MC-DS-STDCC Receiver

Figure 4.2. MC-DS-STDCC transceiver.

On the transmitter side, Figure 4.2(a), a pseudo-random binary sequence (PRBS) of data rate R_{b} is copied N times, where N is the number of subcarriers corresponding to different frequency bands, and propagated in parallel such that the data rate of each subcarrier signal is the same as the original signal. The subcarrier signals are then spread in the time domain with an independent spreading code. The selection of the spreading code depends on the system requirement. The data rate for each subcarrier after spreading becomes the chip rate $M_i R_{\mathrm{b}}$, where M_i is the spreading sequence length of the i^{th} subcarrier. Note that M_i could be different for each subcarrier depending on the power level limit of each frequency band or interference tolerance.

In this dissertation, the Orthogonal Variable Spreading Factor (OVSF) codes and m-sequence are studied and compared as the spreading codes for the sounder. OVSF codes are recommended for Wideband-CDMA (W-CDMA) systems [62]. One important property of OVSF codes is that the orthogonality between codes is guaranteed regardless of spreading factors, which reduces the intercarrier interference. It was first designed to achieve various symbol rates for different users in W-CDMA systems [29, 63]. This property of the OVSF codes guarantees orthogonality between codes for the case where spreading codes with different lengths are used.

Due to the chip rate difference after spreading, shorter output sequences are zero-padded to compensate for the chip rate differences with respect to the largest spreading sequence length $M_{\mathrm{m}} = \max\{M_i\}$, such that all the output sequences are aligned in time before the IFFT operation. Hence, the chip rate is equal to $M_{\mathrm{m}} R_{\mathrm{b}}$ for each subcarrier signal. Extra information on the power level limit for each frequency band also needs to be transmitted to the receiver. This information

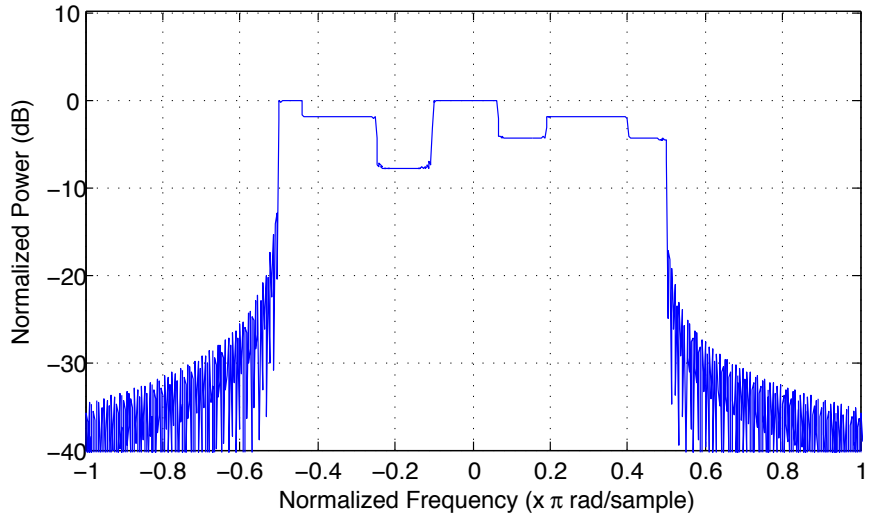

Figure 4.3. Multicarrier sounding signal power spectrum density with 256 subcarriers and varying spreading gain.

can also be interpreted as the spreading sequence length M_i for each subcarrier. The power spectrum density (PSD) of each subcarrier signal occupies an equal bandwidth but with different power levels [64]. Figure 4.3 shows an example of the PSD of a 256-subcarrier MC-DS-STDCC with different spreading gains across the whole frequency band. The entire band is divided into seven subbands, where each subband may contain multiple numbers of subcarriers, and each subband has its power level limit. Depending on the total transmission bandwidth, as well as the bandwidth for each user, the number of subcarriers can be adjusted accordingly.

Last, the modulated parallel data streams are serialized using a Parallel to Serial (P/S) converter and transmitted, and the transmitted sequence chip rate is reduced to $M_{\mathrm{m}}R_{\mathrm{b}}/N$.

For example, the normalized complex envelop of an baseband M-PSK modulated MC-CDMA signal is represented for the duration of a symbol period T

as:

$$s(t) = \frac{1}{\sqrt{N}} \sum_{n=0}^{N-1} \sum_{m=0}^{M_{\mathrm{n}}-1} b_{\mathrm{n}} \cdot c_{\mathrm{n}}[m] \cdot e^{j2\pi F_{\mathrm{n}} R_{\mathrm{b}}^{\mathrm{n}} m t},$$

where N is the number of subcarriers, M_{n} represents spreading sequence length of each subcarrier, b_{n} is the information bit of the nth subcarrier, and $c_{\mathrm{n}}[m]$ is the mth chip of the spreading sequence associated with the information bit on the n^{th} subcarrier. The square bracket $[\cdot]$ denotes the discrete index of the spreading sequence, since M_{n} is a variable according to different subcarriers, and the length of $c_{\mathrm{n}}[m]$ is also different for each subcarrier. For calculating the envelope power of the signal, we only consider nonzero values, which means we only consider the elements satisfying $|c_{\mathrm{n}}[m]| = 1$. F_{n} is defined as the subcarrier separation parameter, in other words, it is the ratio between the spreading sequence length (spreading gain) and the number of subcarriers: $F_{\mathrm{n}} = M_{\mathrm{n}}/N$ [65]. When $F = 1$, the subcarrier separation is the symbol rate R_{b}, the MC-DS-CDMA signal spectrum has the same shape, as in an MC-CDMA system. When F is a variable, the signal spectrum is no longer the same. To maintain the subcarrier separation constant, but vary the signal power on each subcarrier, the symbol rate R_{b} is also changed accordingly by zero-padding, and those two variables are represented as F_{n} and $R_{\mathrm{b}}^{\mathrm{n}}$.

The received signal is converted into N parallel data streams and fed into each subcarrier. The extra zeros are removed based on information M_i before FFT demodulation. The cross-correlation operation is done on a subcarrier basis, where the demodulated signal is cross-correlated with an individual PRBS signal at chip rate of $M_{\mathrm{m}}R_{\mathrm{b}}$. The PRBS signal used at the receiver is obtained by spreading the output of an identical PRBS generator with respect to the spreading sequence length for each subcarrier.

At the receiver, shown in Figure 4.2, the distorted signal is parallized into N streams, and the time domain signal is then converted to the frequency domain by FFT demodulation. The cross-correlation process is done on a subcarrier basis, since each branch carries a complete STDCC unit. After the cross-correlation, each branch gives a series of channel impulse responses for the center frequency associated with it, and they are expressed as $\hat{h}_i(\tau), i = 1 \ldots N$. The cross-correlation process produces a direct estimation of the time domain channel response. The transfer function can be obtained by applying FFT on the power delay profile (PDP) on each branch. Note that the receiver does not despread the received signal prior to cross-correlation in order to maintain a high sampling rate such that the delay resolution is improved. Moreover, despreading the received signal will discard the desired channel information. The disadvantage is that the autocorrelation property of the m-sequence is ruined. However, channel sounding accuracy can still be guaranteed if the spreading sequence length is properly selected. The locally generated m-sequence is correlated with the distorted spread spectrum signal to recover the channel impulse response. The impact on the performance will be quantified in the later section.

4.2.1 Channel Impulse Response Estimation

Intuitively, it is possible to obtain the channel frequency response by taking advantage of the FFT operation built in the MC-CDMA system. However, one common assumption for multicarrier modulation systems, i.e., OFDM and MC-CDMA, is that the carrier separation should be large enough to make sure the signal on each subcarrier undergoes the independent fading. In contrast, for the MC-DS-STDCC system, the frequency response might only be obtained under the

condition where fading on one subcarrier is correlated to another. Furthermore, in order to achieve this approach, the sounding signal needs to be carefully designed depending on the channel environments, especially the total signal bandwidth and number of subcarriers. These two parameters determine the type of fading effects that will be experienced by the signal. Since the subcarrier separation is reduced to introduce the correlation between subcarriers, the total bandwidth is also reduced.

The overall estimation of the channel impulse response (CIR) is the combination of each subcarrier's estimation. To ensure a good minimum delay resolution, the cross-correlation is performed at a chip rate of $M_{\mathrm{m}}R_{\mathrm{b}}$, since channel information will be lost if the estimation process is done after despreading. Hence, the minimum delay resolution is expressed as:

$$\Delta\tau = \frac{2}{M_{\mathrm{m}}R_{\mathrm{b}}}. \tag{4.1}$$

Comparing Equation (4.1) with the minimum delay resolution of an STDCC system, which is $2/R_{\mathrm{b}}$, the minimum delay resolution of the MC-DS-STDCC system is increased by a factor of M_{m}. This is due to the inherent processing gain provided by the direct sequence spread spectrum system. Given a certain power level threshold, the maximum multipath delay spread can be detected is given by:

$$\tau_{\max} = \frac{LN}{M_{\mathrm{m}}R_{\mathrm{b}}}. \tag{4.2}$$

Comparing Equation (4.2) with the maximum delay resolution of the STDCC channel sounder, L/R_{b}, the MC-DS-STDCC sounding technique increases the measurement performance by a factor of M_{m}. In other words, the longer the

spreading sequence, the better the performance. However, this approach is at the cost of high sampling rate and system complexity. As discussed in Chapter 3, the PRBS used at the receiver is generated locally, which introduces the potential issue of synchronization. If the received signal and locally generated signal are not synchronized in time before they correlate with each other, the estimation will result in a time-shifted version of the channel impulse response. However, this can be compensated for by estimating the phase rotation of the out-of-phase signal.

4.2.2 Dynamic Range Performance

Ideally, the autocorrelation function (ACF) of an m-sequence is a near-optimal approximation to a train of Kronecker delta function.[1] Spreading the sounding signal (m-sequence) at the transmitter increases delay resolution. However, the autocorrelation function of the sequence after spreading is no longer Kronecker delta like. This is because the insertion of the spreading sequence partially breaks the property of the original m-sequence, which results in a "noisy" autocorrelation function. However, the autocorrelation function of the resulting sequence can be calculated by using the partial autocorrelation property of the m-sequence [66]. It is well known that the periodic autocorrelation function of an m-sequence b is given by [67]:

$$\theta_b(k) = \begin{cases} 1, & k = lN \\ -\frac{1}{N}, & k \neq lN \end{cases}, \tag{4.3}$$

where $\theta_b(k)$ denotes the value of the autocorrelation function at the k^{th} lag , and N represents the sequence period and l is an integer. Note that Equation (4.3)

[1]Kronecker delta function δ is defined as: $\delta_i = \begin{cases} 1, & \text{if } i = 0 \\ 0, & \text{if } i \neq 0 \end{cases}$.

is defined over a complete cycle of the sequence. If the correlation estimate is based on a correlation over a partial period, Equation (4.3) is no longer valid. It is shown in [66] that the partial autocorrelation function of an m-sequence b is given by:

$$\theta_b(k, k', W) = \frac{1}{W} \sum_{m=k'}^{k'+W-1} a_m a_{m+k}, \tag{4.4}$$

where k' is the starting index of the window, and W denotes the window size. Observe that the partial autocorrelation function is not well behaved as was the full-period autocorrelation function, since the partial-period autocorrelation is not two-valued and it is a function of window size and the position of the window. Due to the random behavior of the partial autocorrelation function, it is convenient to use the variance over k' of $\theta_b(k, k', W)$ to determine the partial autocorrelation function. The variance is defined as [66]:

$$\begin{aligned} \text{var}\left[\theta_b(k, k', W)\right] &= \overline{\theta_b^2(k, k', W)} - \left[\overline{\theta_b(k, k', W)}\right]^2 \\ &= \frac{1}{W}\left(1 - \frac{W-1}{N}\right) - \frac{1}{N^2}. \end{aligned} \tag{4.5}$$

Figure 4.4 demonstrates the partial window size of a 15-chip m-sequence. Ide-

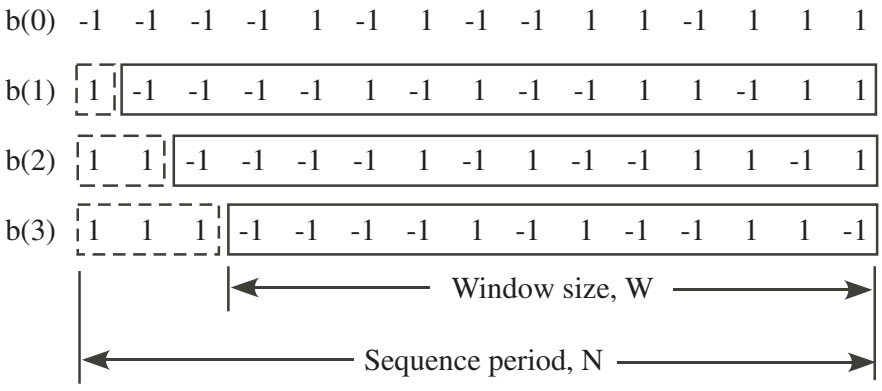

Figure 4.4. Partial autocorrelation with different window size W.

ally, if the autocorrelation is estimated over the sequence period N, the partial autocorrelation function is then equal to Equation (4.3), and Equation (4.4) is equal to zero. Spreading the original m-sequence $\{a_i\}$, $0 \leq i \leq N-1$ with the spreading m-sequence $\{b_j\}$, $0 \leq j \leq K-1$ can be considered as concatenating the spreading m-sequence N times, and hence the resulting sequence is $a_i\{b_j\}$. Note that a_i contains ± 1s, which means that the partial autocorrelation function $\theta_b(k, k', W)$ becomes $a_i\theta_b(k, k', W)$.

Figure 4.5 shows an example of the relationship between the variance and the window size of a 15-chip m-sequence. Observe that the magnitude of variance is equal to 0.01778 with window size of 12. The window size can also be interpolated as the lag with respect to zero lag (window size of 15), and hence, the variance is

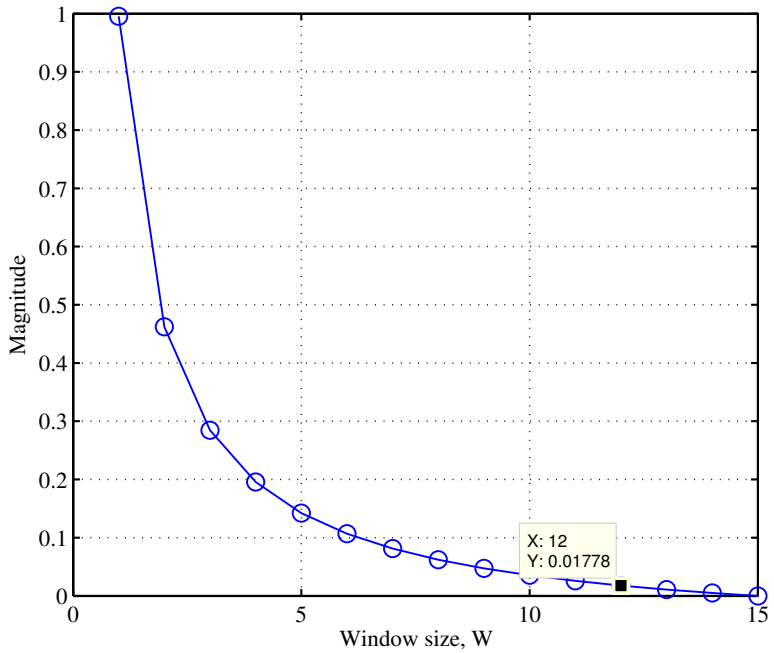

Figure 4.5. Variance of the partial autocorrelation function as a function of window size; m-sequence length = 15.

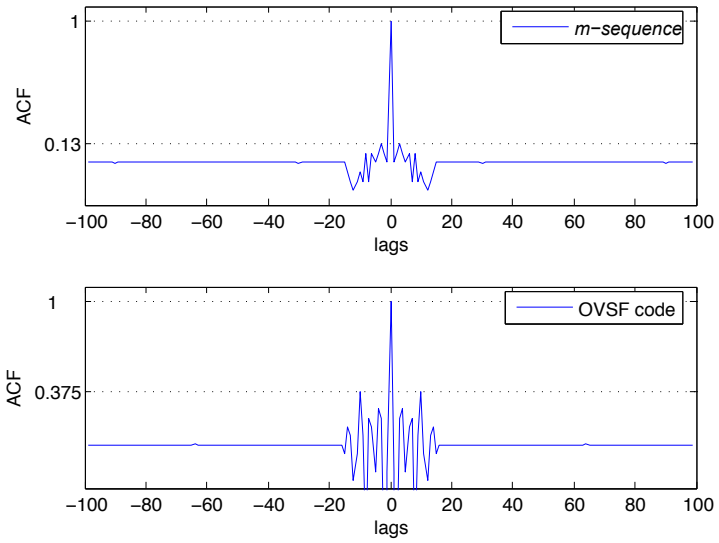

(a) 15-chip m-sequence versus 16-chip OVSF code.

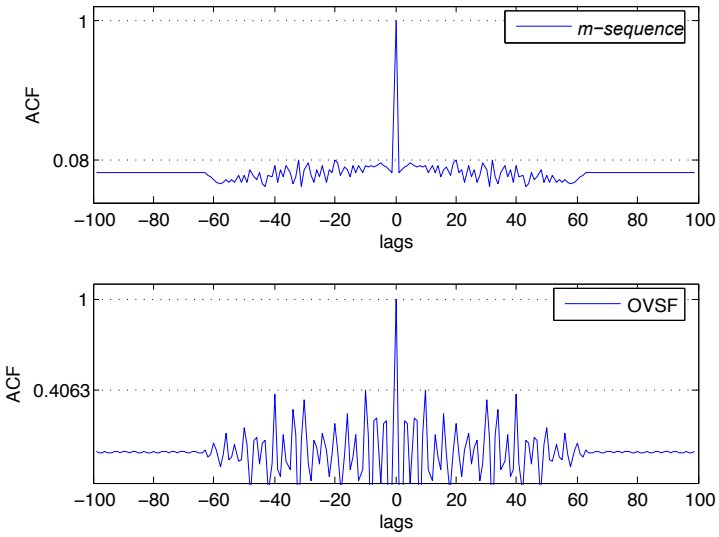

(b) 63-chip m-sequence versus 64-chip OVSF code.

Figure 4.6. Dynamic range performance with different spreading sequences.

equal to 0.01778 at lag 3. Let θ_a be the maximum out-of-phase autocorrelation peak level. The analysis indicates that if θ_a appears at lag 3, the peak magnitude is equal to $\sqrt{0.01778} \approx 0.1333$. However, the position of θ_a is not unique, and it depends on the feedback polynomial of the linear feedback shift register. A

simulation is conducted to validate the previous analysis. Assuming that a 255-chip m-sequence is spread by using a 15-chip m-sequence and a 16-chip OVSF code, as well as an m-sequence of 63-chip and an OVSF code of 64-chip. The partial autocorrelation function is shown in Figure 4.6. As we can see from the top figure in Figure 4.6(a), θ_a is equal to 0.13 at lag 3, which matches the analytical result. Although the position of the θ_a is not unique, Sarwate provided a general lower bound and upper bound for any periodic and aperiodic binary sequences in [67, 68].

As shown in Table 3.1, the dynamic range is a function of sequence length L. In reality, m-sequence can only be length of $2^r - 1$, where r is an integer. To evaluate the dynamic range performance degradation, we assume that the dynamic range of the sequence after spreading is also a function of sequence length. In Figure 4.6, m-sequence spreading outperforms OVSF codes spreading. This is due to the fact that the ACF of an m-sequence is an impulse. Moreover, Figure 4.6(b) indicates that a longer spreading sequence results in a better performance when m-sequence spreading is used. Although the OVSF codes do not have superior autocorrelation property as m-sequence does, they are easy to generate. OVSF codes are generated recursively, which means once the code tree is built, shorter codes are also accessible from the deeper branches of the tree. This feature increases the degree of freedom for code selection. If the power level limit changes frequently across frequencies, an m-sequence has to be generated individually for each subband to meet the transmit power limit. Figures 4.7 and 4.8 show the relationship between dynamic range performance and spreading sequence length. As discussed previously, m-sequence spreading promises greater dynamic range than OVSF code spreading especially with a longer spreading sequences; m-sequence

spreading outperforms OVSF code spreading by 7 dB with spreading factor of 64. It is also seen from Figure 4.7, the dynamic range difference between the

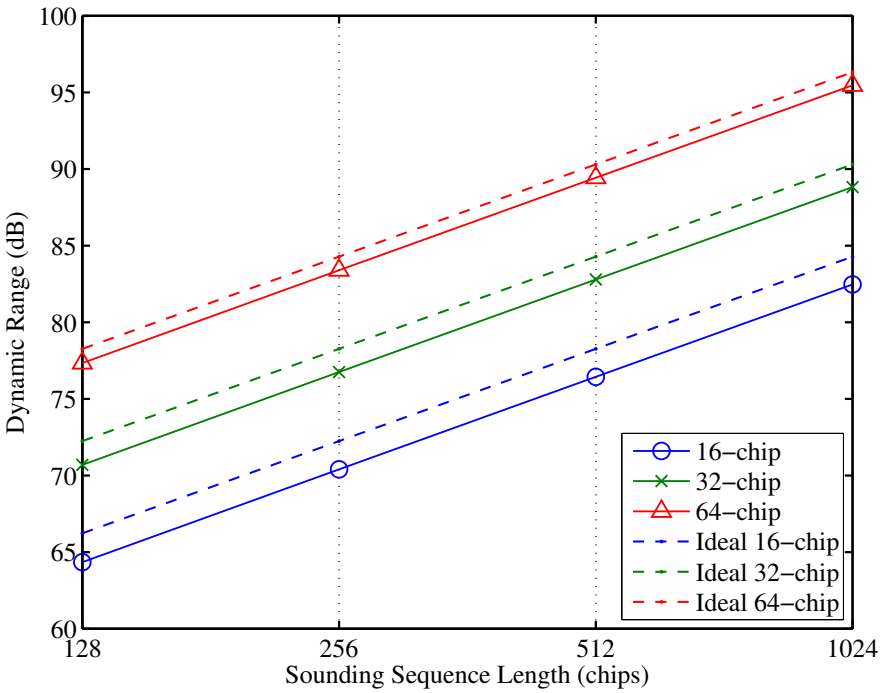

Figure 4.7. Dynamic range performance using m-sequence as spreading sequence.

ideal and non ideal values gets smaller as the spreading sequence length increases. The dynamic range difference is less than 3 dB for all three cases. The opposite trend is observed from Figure 4.8; shorter spreading sequence results in minimum dynamic range degradation. However, the difference for 16-chip spreading is still more than 6 dB. This analysis explains the reason why m-sequence is chosen as superior to other spreading sequences. Moreover, the combination of the sounding sequence and spreading sequence could provide the same delay resolution as the sequence with the same length can. For example, a sounding sequence with degree of 12 (4095 chips) is equivalent to a sounding sequence with degree of 8

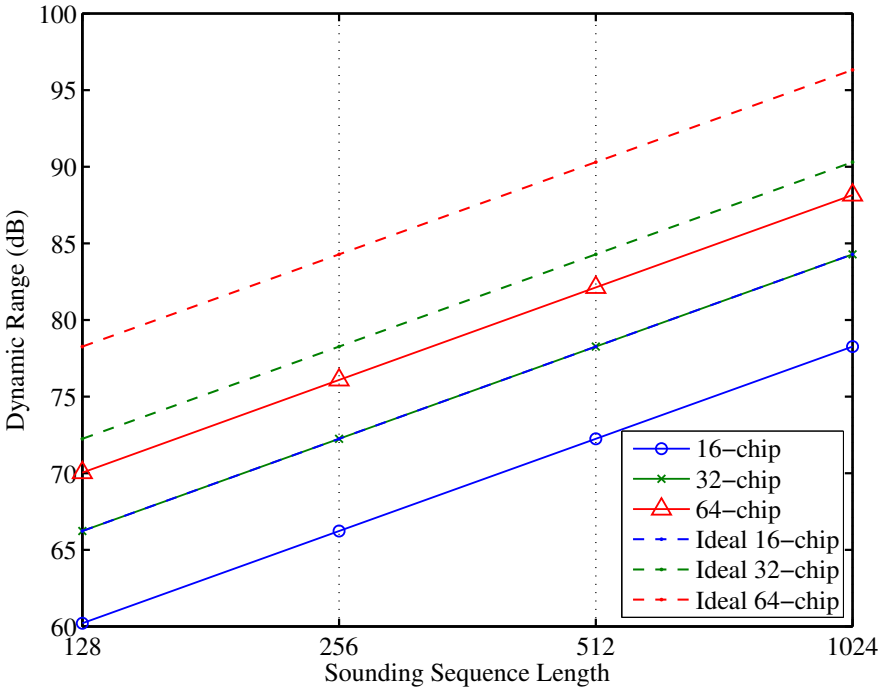

Figure 4.8. Dynamic range performance using OVSF codes as spreading sequence.

(255 chips) spread by another sequence with degree of 4 (16 chips) in terms of delay resolution.

There are other pseudo-random binary sequences other than the m-sequence, such as Kasami sequences, gold sequences, Barker sequences and Williard sequences [69]. The choice of m-sequence is because it has the best autocorrelation property among other PN sequences, which promises the largest dynamic range, and periodicity. The m-sequence can be generated with a Linear Feedback Shift Register (LFSR), which can be easily implemented on an FPGA or other programmable logic devices.

4.2.3 Assessing the Impact of the Proposed Channel Sounding Technique

In addition to the performance, interference introduced by the sounding signal to the primary and secondary users cannot be neglected. The total interference caused by the sounding signal is evaluated by employing the primary user signal-to-noise inteference ratio (SINR), which is defined by:

$$\text{SINR (dB)} = 10\log_{10}\sum_{i=1}^{N}\frac{P_i}{I_i + BN_0}, \tag{4.6}$$

where P_i is the transmit power for a certain primary user within the i^{th} subcarrier bandwidth, N_0 is the noise power spectral density, and it is assumed to be the same for all the subcarriers, I_i is the interference power introduced by the sounding signal on the i^{th} subcarrier, and N is the number of subcarriers. Since the sounding signal is spread in the time domain, the resulting sounding signal power becomes $P_{\text{s}}^{(i)} - G_i$, where G_i is the spreading gain for the i^{th} subcarrier. Hence, Equation (4.6) can be rewritten as:

$$\text{SINR (dB)} = 10\log_{10}\sum_{i=1}^{N}\frac{P_i}{P_{\text{s}}^{(i)} - G_i + B_iN_0}, \tag{4.7}$$

where B_i denotes the subcarrier bandwidth after spreading. For equal spreading gain scenario, G_i becomes a constant, so does B_i. Equation (4.7) works for primary users with interference tolerance greater than zero. For zero-interference tolerance, the band is totally inaccessible when primary users are present in this band.

It is noticed that the SINR is inversely proportional to the spreading gain G_i for the i^{th} subcarrier, increasing spreading gain will improve the SINR significantly.

However, as discussed previously, time domain spreading of the sounding signal violates the cross-correlation property of the original signal. Hence, the channel sounding performance degrades. Moreover, direct sequence spreading increases DAC sampling rate by M_m times, which substantially increases overall system cost.

4.3 Simulation Results and Analysis

In this section, both STDCC and MC-DS-STDCC systems are simulated. Simulation results are compared in terms of channel sounding performance. Due to structure differences between the two systems, some simulation parameters could be different for fair comparisons. For example, the baseband data rate for the MC-DS-STDCC system is reduced according to the spreading gain to maintain the same chip rate (after spreading) as the STDCC system. Both systems use the same modulation and demodulation schemes, i.e., BPSK, the same PRBS generator except the data rate for the m-sequence generators are different to ensure the channel environment has the same impact on both signals, and the channel environments for both systems are identical.

4.3.1 Simulation Setup

The simulation parameters are listed in Table (4.1). The multipath fading channel contains five multipath components with each path attenuation a zero complex Gaussian random variable. The channel is also assumed to be a frequency nonselective slow fading channel, meaning that the channel is flat over all the subcarriers and the channel is changing slowly over time compared to one symbol duration.

Table 4.1. Simulation parameters.

Parameters	**STDCC**	**MC-DS-STDCC**
Modulation	BPSK	BPSK
m-sequence length(chips)	255-2047	255-2047
Baseband bandwidth (MHz)	10	varying
Number of subcarriers	1	16-128
Number of multipath components	5	5
Maximum delay spread (ns)	500	500
Average attenuation (dB)	0 -5 -12 -16 -21	0 -5 -12 -16 -21
SNR (dB)	0-30	0-30

Since the MC-DS-STDCC system copies the PRBS signal onto each subcarrier, the data rate is maintained before spreading. After spreading, the m-sequence data rate R_0 is upconverted to a higher chip rate R_c. Finally, parallel streams are serialized, which means the chip rate is increased by a factor of the total number of subcarriers N. To ensure the signals for both systems experience the same channel environment, the baseband data rate for the MC-DS-STDCC has to be NR_c/R_0 times slower than the one in STDCC. In addition, the m-sequence length for both systems remains the same.

4.3.2 STDCC Simulation Results

Figures 4.9, 4.10, 4.11, and 4.12 show the simulated channel impulse responses for a Rayleigh fading channel with five multipath components. Each multipath component is modeled as a complex Gaussian random process with zero mean and average attenuation for each path as the variance. It is clear to see that the dynamic range increases as the m-sequence length gets longer, which matches the

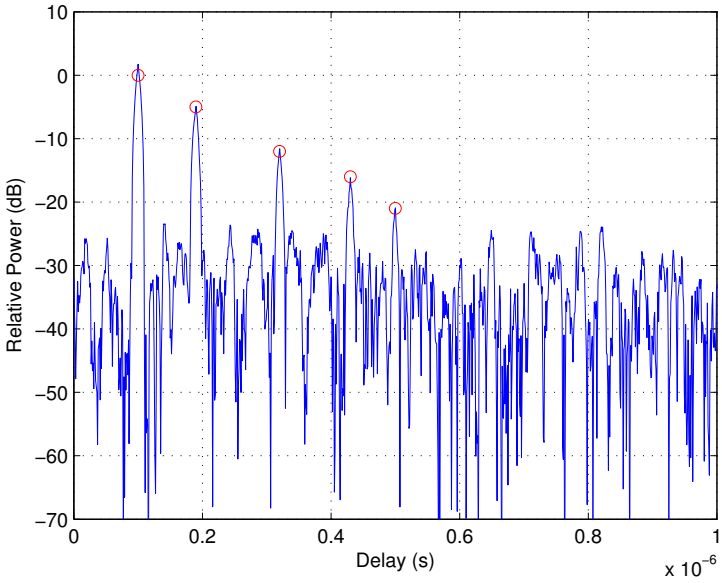

Figure 4.9. Simulated channel impulse response. SNR=0 dB; path delay={100,190,320,430,500} ns; average attenuation={0,-5,-12,-16,-21} dB, respectively; m-sequence length = 255.

theoretical analysis. This feature is especially essential for DSA networks where the transmit power is limited, because larger dynamic range allows weaker channel impulse response to be detected.

It is also noticed that the dynamic range performance degrades dramatically as the channel environment becomes complicated (e.g., multipath fading). The ideal dynamic range can be referred to in Table 3.1. For instance, the ideal dynamic range for an m-sequence length of 255 is 48.1 dB, but the simulation results show that the weakest detectable signal is roughly 30 dB lower than the strongest. In this set of simulations, the chip rate is set to 100 chips/s to ensure that two adjacent delay paths are resolvable. As discussed in the previous chapter, the maximum delay spread that can be measured by the system is: m/R_{c}, take

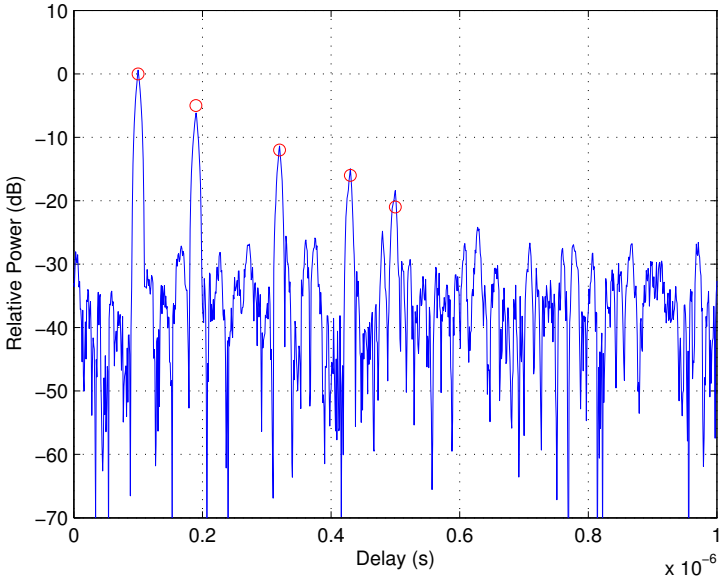

Figure 4.10. Simulated channel impulse response. SNR=0 dB; path delay={100,190,320,430,500} *n*s; average attenuation={0,-5,-12,-16,-21} dB, respectively; *m*-sequence length = 511.

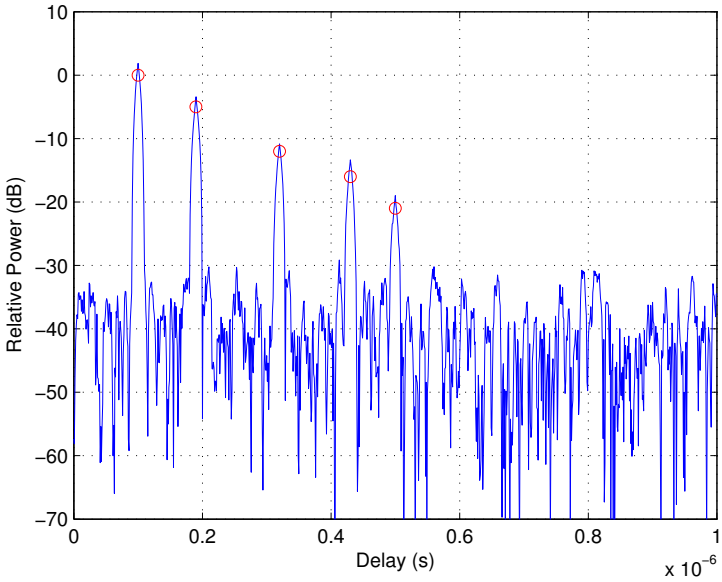

Figure 4.11. Simulated channel impulse response. SNR=0 dB; path delay={100,190,320,430,500} *n*s; average attenuation={0,-5,-12,-16,-21} dB, respectively; *m*-sequence length = 1023.

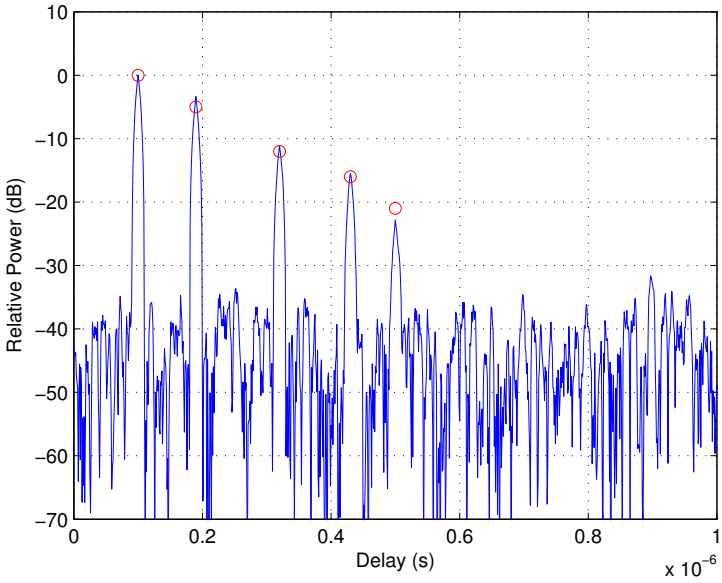

Figure 4.12. Simulated channel impulse response. SNR=0 dB; path delay={100,190,320,430,500} ns; average attenuation={0,-5,-12,-16,-21} dB, respectively; m-sequence length = 2047.

$m = 255$ for example:

$$\tau_{\max} = \frac{255}{80 \text{ MHz}} = 3.1875 \ \mu\text{s}. \tag{4.8}$$

In Equation (4.8), the original signal is upsampled to 80 MHz, i.e., there are eight samples per chip instead of one sample per chip for a better resolution. The maximum path delay set in the simulation is 0.5 μs, which means the system is capable of measuring all the path delays.

To validate the simulation model and the causes of the dynamic range degradation, the following simulations were conducted:

- AWGN channel: SNR = 0 dB, 10 dB, 30 dB, 100 dB (negligible amount of white noise) .

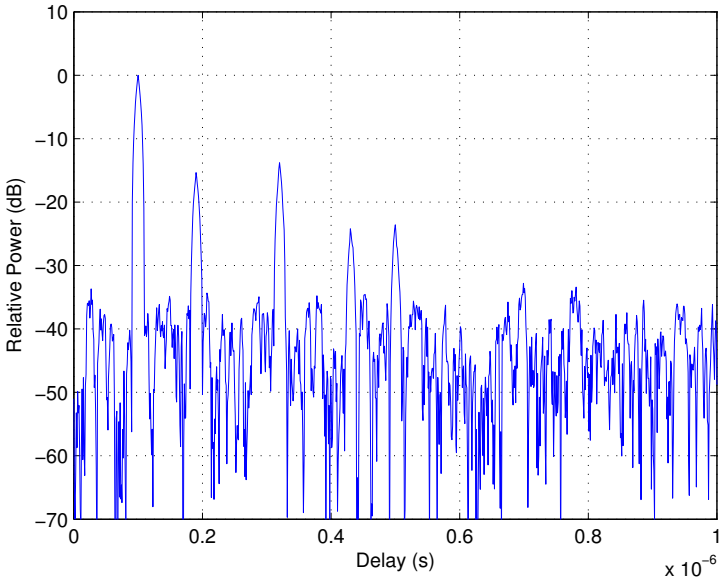

Figure 4.13. Dynamic range degradation due to white noise without ISI with 511-bit m-sequence. Path delay=$\{100,190,320,430,500\}$ ns; average attenuation=$\{0,-5,-12,-16,-21\}$ dB, respectively; SNR=0dB.

- Multipath channel environment: no ISI, with ISI.

In Figures 4.13, 4.14, 4.15 and 4.16, the dynamic range is directly related to the noise power, which is represented as SNR in decibels. With a nearly perfect channel (100 dB), the dynamic range is close to the ideal value for a 511-bit m-sequence, which is 54.2 dB. As the SNR value decreases, the dynamic range degrades. In this case, the channel is assumed to be no ISI, meaning that the attenuation for each path is applied to the entire sequence for one transmission cycle, and only the signal power is attenuated. Phase shift and frequency offset is not considered.

Figures 4.17, 4.18, 4.19 and 4.20 demonstrate the dynamic range degradation due to ISI. In this scenario, the dynamic range does not degrade as much as it does for the AWGN channel since the intersymbol interference power level is dominating

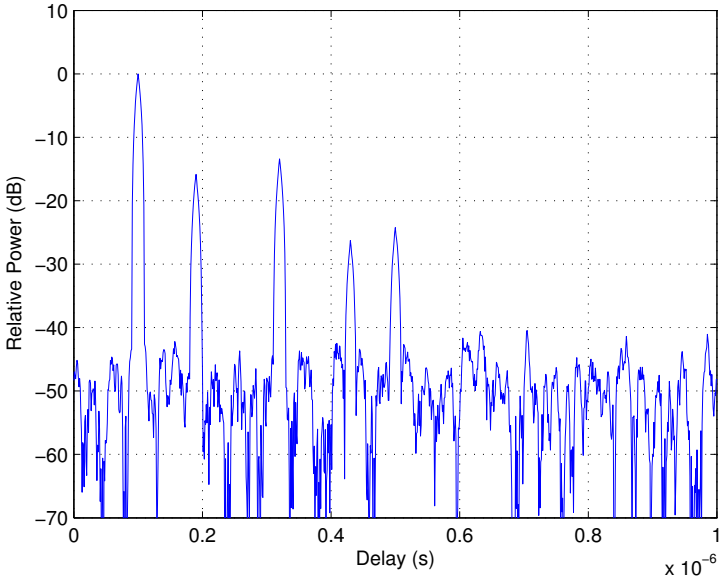

Figure 4.14. Dynamic range degradation due to white noise without ISI with 511-bit m-sequence. Path delay=$\{100,190,320,430,500\}$ ns; average attenuation=$\{0,-5,-12,-16,-21\}$ dB, respectively; SNR=10dB.

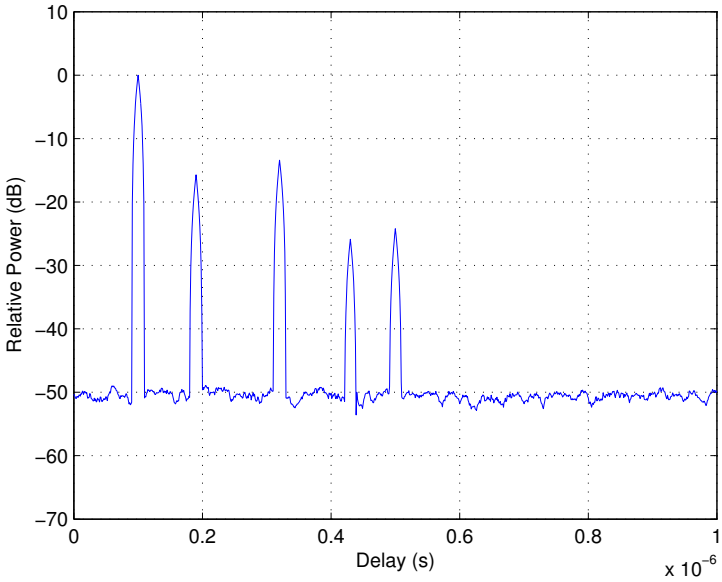

Figure 4.15. Dynamic range degradation due to white noise without ISI with 511-bit m-sequence. Path delay=$\{100,190,320,430,500\}$ ns; average attenuation=$\{0,-5,-12,-16,-21\}$ dB, respectively; SNR=30dB.

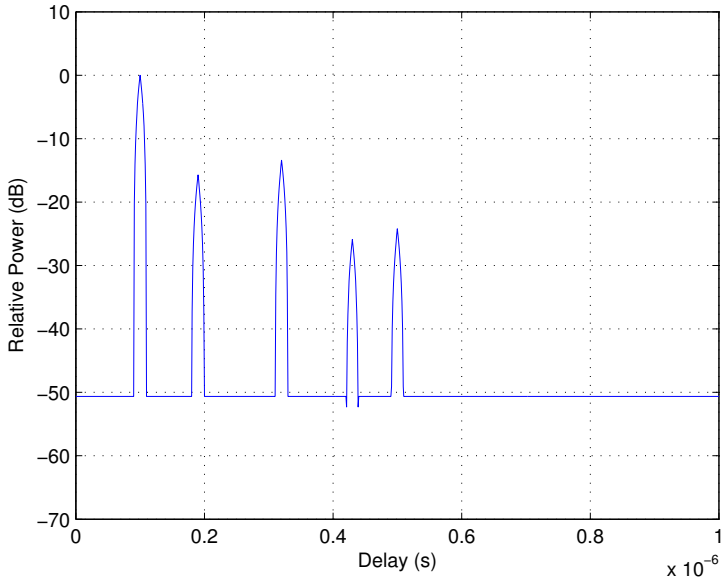

Figure 4.16. Dynamic range degradation due to white noise without ISI with 511-bit m-sequence. Path delay=$\{100,190,320,430,500\}$ ns; average attenuation=$\{0,-5,-12,-16,-21\}$ dB, respectively; SNR=100dB.

over the noise power. Comparing Figure 4.17 with 4.13, it is found that the ISI introduces approximately 10 dB degradation in dynamic range. This analysis is intuitive, although the intersymbol interference power could be quantified in terms of frequency error [64], which will not be discussed in detail here.

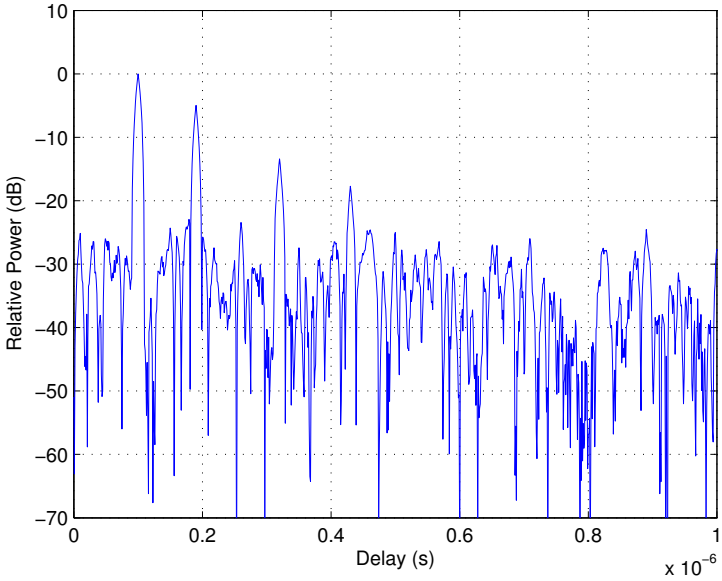

Figure 4.17. Dynamic range degradation caused by ISI. 511-bit m-sequence; path delay= {100,190,320,430,500} ns; average attenuation = {0,-5,-12,-16,-21} dB; SNR= 0 dB.

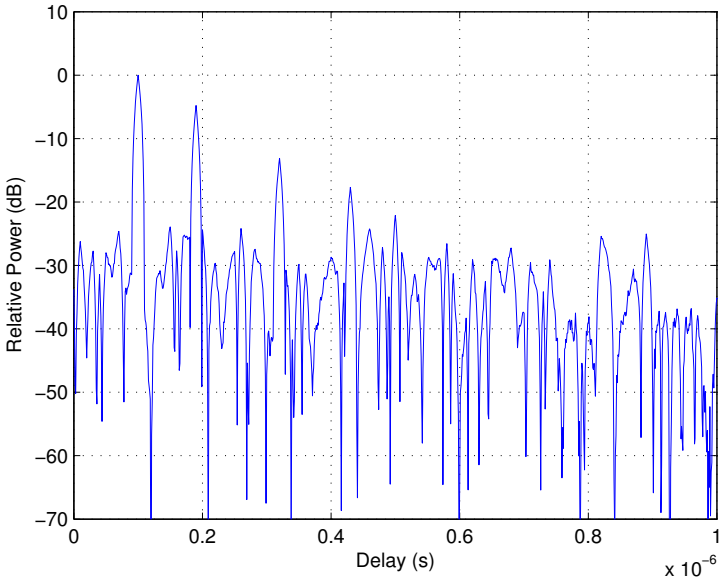

Figure 4.18. Dynamic range degradation caused by ISI. 511-bit m-sequence; path delay= {100,190,320,430,500} ns; average attenuation = {0,-5,-12,-16,-21} dB; SNR= 10 dB.

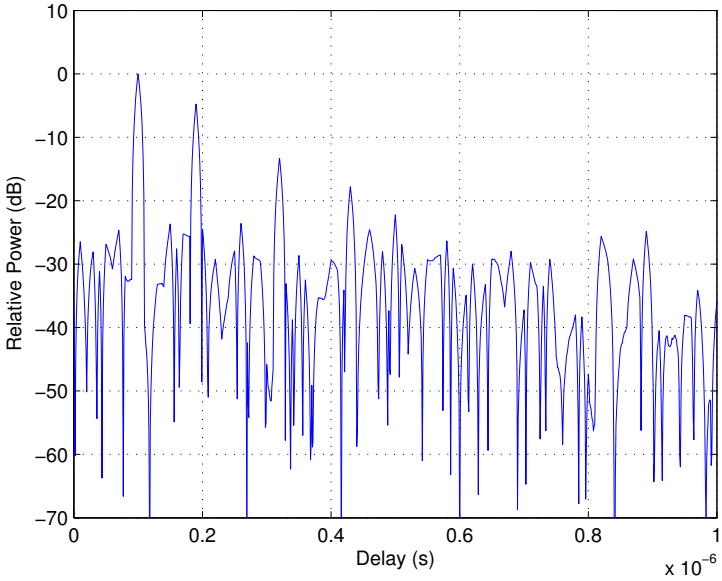

Figure 4.19. Dynamic range degradation caused by ISI. 511-bit m-sequence; path delay= {100,190,320,430,500} ns; average attenuation = {0,-5,-12,-16,-21} dB; SNR= 30 dB.

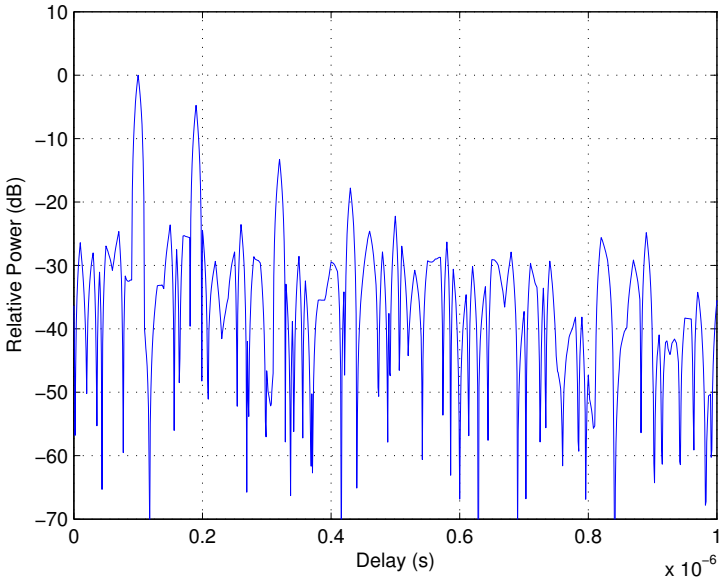

Figure 4.20. Dynamic range degradation caused by ISI. 511-bit m-sequence; path delay= {100,190,320,430,500} ns; average attenuation = {0,-5,-12,-16,-21} dB; SNR=100 dB.

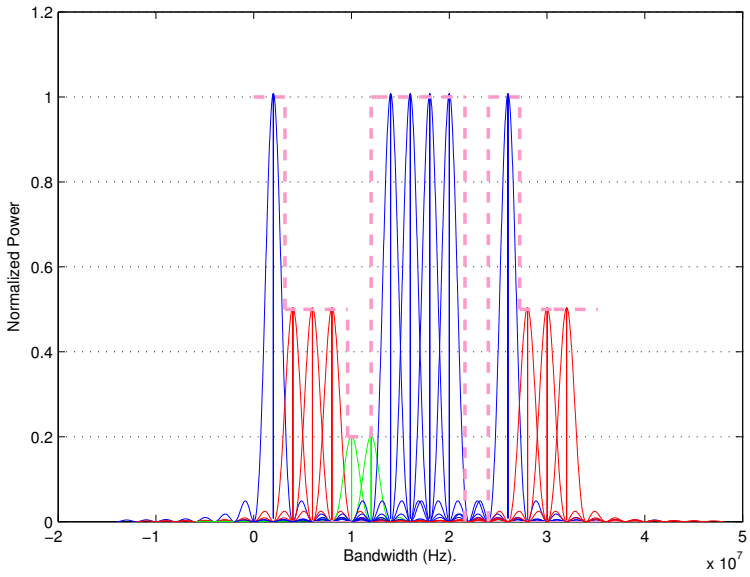

Figure 4.21. Power spectral density of MC-DS-STDCC signal with 16 subcarriers and total transmission bandwidth of 30 MHz.

4.3.3 MC-DS-STDCC Simulation Results

The simulation setup is basically the same as the STDCC system, except the chip rate is different. It is also assumed that the channel is flat over subcarriers.

One of the advantages of MC-DS-STDCC systems, as discussed before, is the ability to be operated at different center frequencies with various transmit powers. An example can be seen from Figure 4.21, where the dashed line represents the transmit power limits, and solid curves are the signal spectrum. Each curve is a sinc(·) function. It is easy to notice that the bandwidth of each subcarrier is the same but the power is different. In some of the Ultra-Wideband (UWB) applications, pulse shaping is used to ensure the ultra-wideband signal spectrum fits, for instance the FCC mask [39]. The multicarrier modulation technique provides a more adaptive way of spectrum control. In addition, digital signal processing techniques, such as windowing and sidelobe cancellation can also be applied to

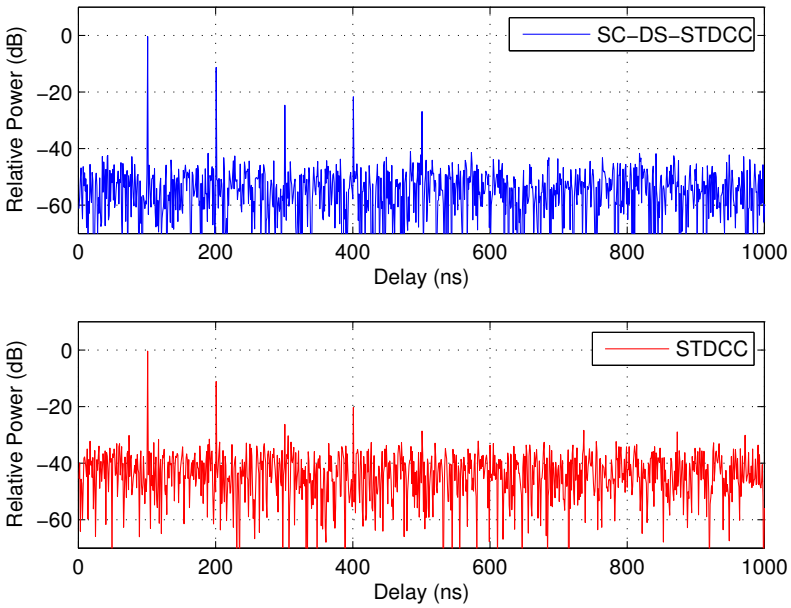

Figure 4.22. SC-DS-STDCC with 16-bit spreading sequence vs. STDCC. The delay of each path is 100,200,300,400,500 ns, and the average attenuation of each path is 0,-10,-15,-20,-25 dB, respectively.

the transmitted and received sounding signals to improve the performance as well as to reduce the spectral efficiency [70–72].

To validate the MC-DS-STDCC simulation model, we started with a single-carrier direct sequence STDCC (SC-DS-STDCC) system, comparing the simulation result with the STDCC system. Since there is only one subcarrier in the MC-DS-STDCC system, the copier, P/S, S/P, IFFT, and FFT can be treated as redundant blocks, which do not change the data sequence, except spreading and despreading. Figure 4.22 shows the estimated channel impulse response. The performances of both SC-DS-STDCC and STDCC systems are identical, except that the error floor of the SC-DS-STDCC is about 12 dB ($10\log_{10}(16)$, spreading sequence length is 16) lower than the STDCC system. This is because of the processing gain introduced by the time domain spreading process.

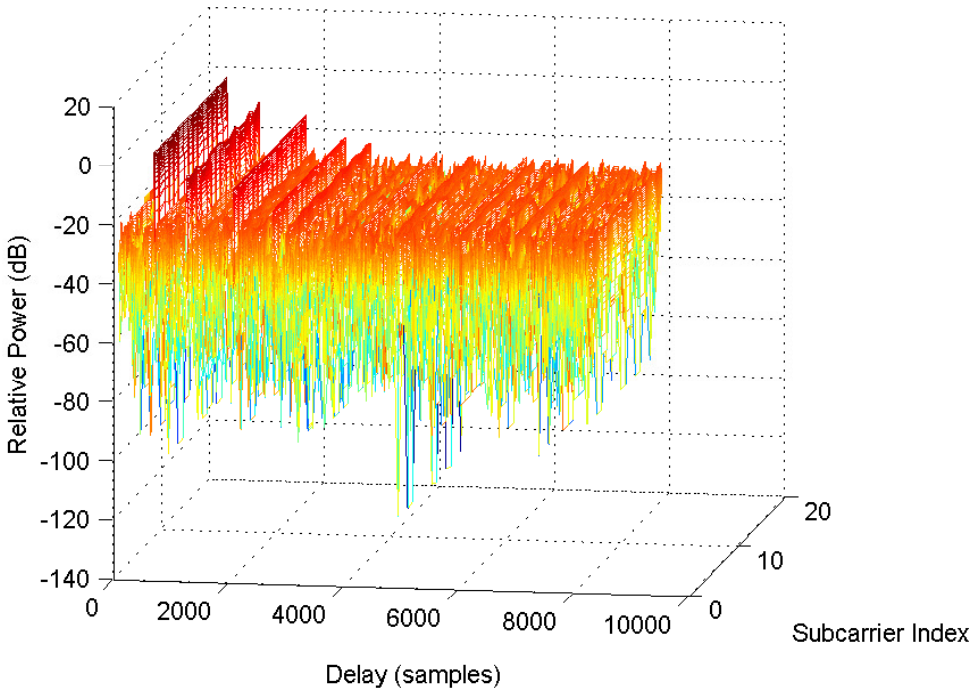

Figure 4.23. MC-DS-STDCC simulation results with 16 subcarriers and 511-bit m-sequence. The delay of each path is 100,190,320,430,500 ns, and the average attenuation of each path is 0,-5,-12,-16,-21 dB, respectively.

Figure 4.23 shows an estimated channel impulse response of a 16-subcarrier MC-DS-STDCC system in presence of a flat fading channel. The power is normalized with respect to the first multipath component, and it is flat over subcarriers. For the rest of the multipath components, the power level is varying over subcarriers, which is due to Gaussian white noise.

4.3.4 Mean Squared Error of the CIR Estimation

In this section, the MC-DS-STDCC channel sounder performance is evaluated by introducing the mean squared error of the estimated CIRs for various cases.

The MSE of the estimated CIRs is defined as the following:

$$\mathrm{MSE(t)} = \mathrm{E}\left[\left(P_{\hat{c}_i}(\tau) - P_{c_i}(\tau)\right)^2\right], \tag{4.9}$$

where $P_{\hat{c}_i}(\tau)$ and $P_{c_i}(\tau)$ represent the the power levels associated with each channel impulse response at delay τ for the estimated CIR, and actual CIR, respectively. The MSE is estimated by averaging the CIR over a time period of T. The m-sequence length varies from 127 to 511 chips, number of subcarriers chosen are 16, 32 and 64, and the spreading sequence length for m-sequence spreading and OVSF code spreading is {15, 16} and {31, 32}, respectively. The MSE performance is compared with different system parameter combinations.

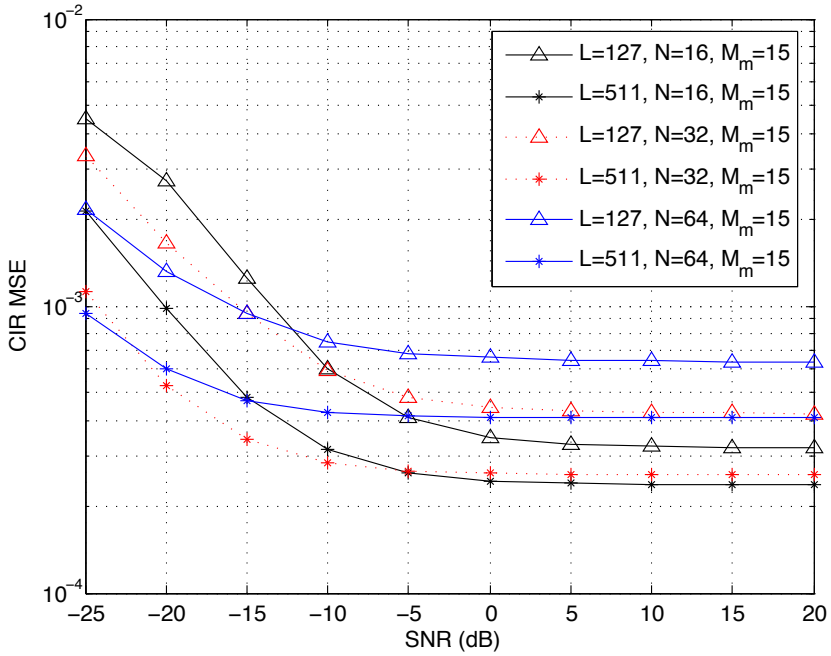

Figure 4.24. MC-DS-STDCC MSE performance. $L = \{127, 511\}$; $N = \{16, 32, 64\}$; M_{m}={15}.

Figure 4.24 compares the MSE performance between m-sequence and OVSF code spreading with spreading sequence length of 15 and 16, respectively. The

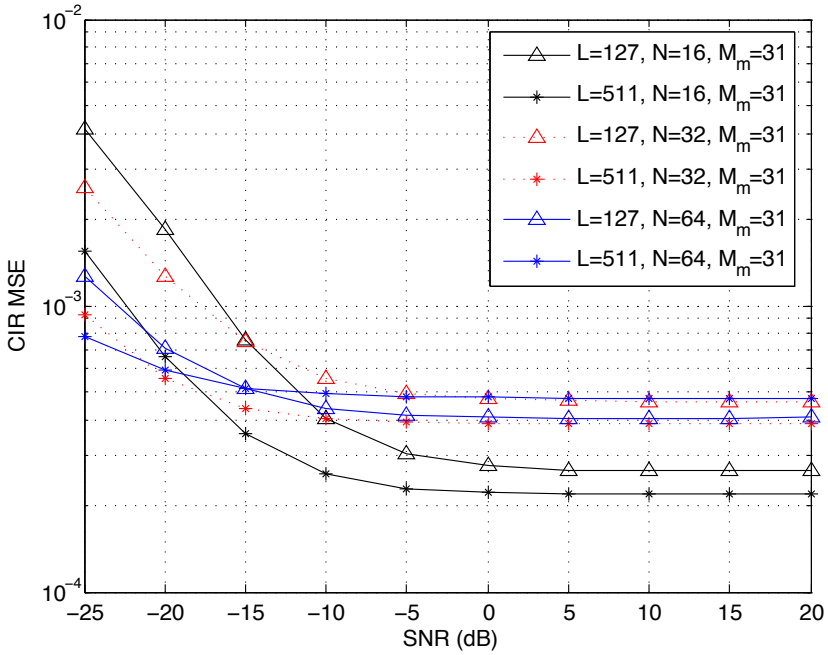

Figure 4.25. MC-DS-STDCC MSE performance. $L = \{127, 511\}$; $N = \{16, 32, 64\}$; M_{m}=$\{31\}$.

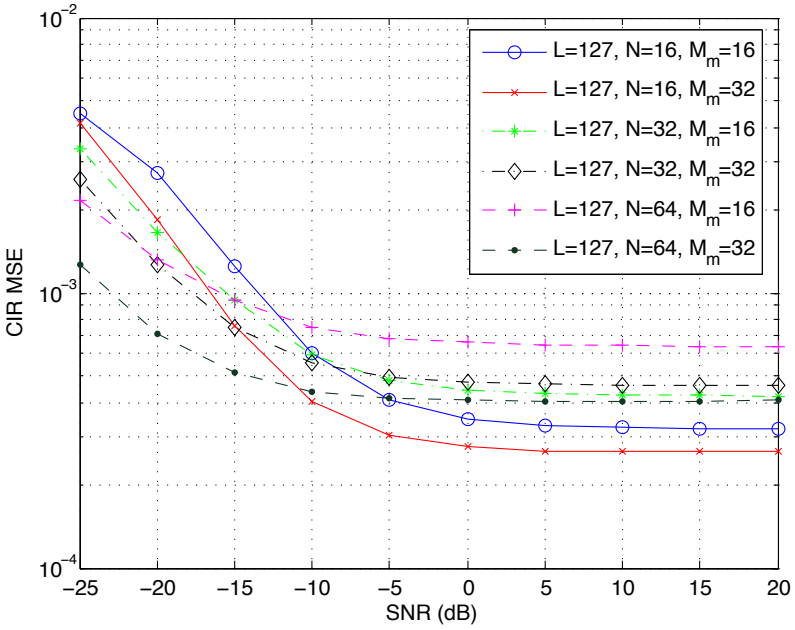

Figure 4.26. MC-DS-STDCC MSE performance. $L = \{127\}$; $N = \{16, 32, 64\}$; M_{m}=$\{15,\ 31\}$.

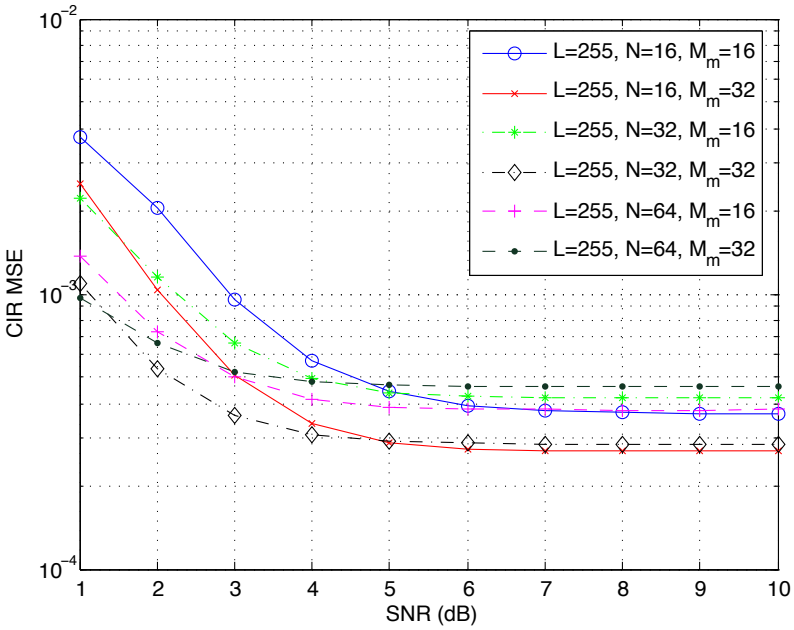

Figure 4.27. MC-DS-STDCC MSE performance. $L = \{255\}$; $N = \{16, 32, 64\}$; M_{m}=$\{15,\ 31\}$.

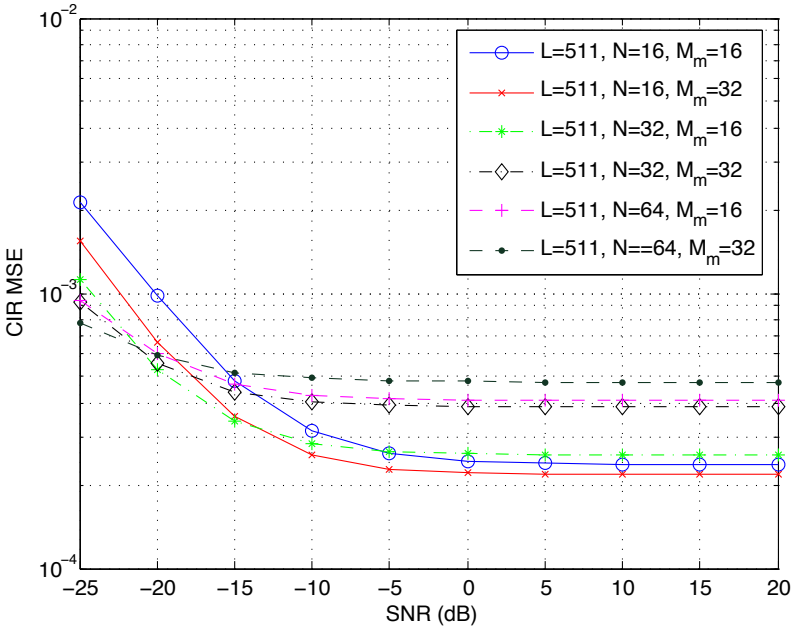

Figure 4.28. MC-DS-STDCC MSE performance. $L = \{511\}$; $N = \{16, 32, 64\}$; M_{m}=$\{15,\ 31\}$.

sounding m-sequence length is L=$\{127, 511\}$, and the number of subcarriers are 16, 32 and 64. As the length of the sounding sequence increases, the MSE error floor decreases. This is because a longer m-sequence provides more inherent processing gain. It is also noticed that 64-subcarrier case results in a worse MSE performance than 32 and 16 subcarriers. Since increasing the number of subcarriers also broadens the noise bandwidth, hence the SNR decreases, which is what causes the MSE error floor to rise.

Comparing Figure 4.25 with Figure 4.24, doubling the length of the spreading sequence reduces the MSE error floor by approximately 6 dB for the combination of $\{L = 511, N = 64\}$. In this case, 32- and 64-subcarrier systems almost perform the same when the SNR is greater than -10 dB. 16-subcarrier system outperforms the other two when the channel SNR value is greater than -10 dB. As discussed previously, a larger number of subcarriers delivers a more frequency-agile channel sounder, since the subcarrier power can be fine tuned to fit the transmit power restriction. However, it does not perform as well as less subcarrier systems in terms of CIR estimation accuracy due to the extra noise introduced.

Figures 4.26, 4.27 and 4.28 demonstrate the MSE performance with fixed sounding sequence length L with various N and M_{m} combinations. They share the same trend as analyzed before, that is, longer spreading sequence provides more processing gain, and hence the MSE error floor decreases. Systems with a larger number of subcarriers introduce wider noise bandwidth, which lower the channel SNR, and hence the MSE performance degrades.

Observe that there appears an irreducible error floor in each figure, which is caused by multi-carrier interference. Qinghua and Coulson have provided detailed BER error floor analysis in [73,74] for MC-CDMA and OFDM systems. Although

the BER error floor analysis does not apply directly to the MSE floor, the cause of the error floor is the same. Considering an MC-CDMA system, we define P_e as the average error floor among all subcarriers, and it is given by [73]:

$$P_e = \frac{1}{N} \sum_{i=1}^{N} P_{e,i}, \tag{4.10}$$

where $P_{e,i}$ is the unconditional error floor of the i^{th} subcarrier, and K denotes the total number of subcarriers. Equation (4.10) indicates that the larger the number of subcarriers, the higher the irreducible error floor. The same conclusion can be drawn from Figures 4.24 through 4.28. In addition to the MC-CDMA system, direct-sequence spreading provides inherent processing gain for the MSE performance. Assume that G_i is the spreading gain for the i^{th} subcarrier, then Equation (4.10) becomes:

$$P_e = \frac{1}{N} \sum_{i=1}^{N} \left(P_{e,i} - G_i \right). \tag{4.11}$$

When $N = 1$, the system simplifies to a single carrier direct-sequence CDMA system, and the error floor analysis can be found in [75].

Overall, one can change the MC-DS-STDCC channel sounder parameters depending on the system requirements, channel sounding accuracy, interference level, etc. When designing a channel sounding system for DSA networks, many factors such as, hardware complexity, interference level, and channel sounding performance, need to be considered. This leads to a multi-objective problem, and a tradeoff has to be made before design.

4.4 Chapter Summary

In this chapter, the MC-DS-STDCC channel sounding technique was explained in detail. System schematics and its mathematical expression of the signal were presented. The system parameters were strengthened. In the end, the chapter is concluded by simulation results and analysis. A sanity check of the proposed technique was done by simulating a Single-Carrier DS-STDCC system and compared with the STDCC simulation result in order to validate the simulation model. A simple 16-subcarrier MC-DS-STDCC system was also simulated with flat fading channel. Further simulations on frequency selective and non equal subcarrier power systems needs to be conducted. On the performance analysis, the mean squared error metric is introduced in measuring the channel sounding performance with various system parameter combinations. The MSE performance is evaluated from different aspects. They are, MSE versus number of subcarriers, MSE versus m-sequence length, and MSE versus spreading sequence length. Depending on the channel sounding measurement requirements, the simulation results can be used as a system design guideline.

The most important feature of the MC-DS-STDCC technique is interference awareness. However, direct sequence spread spectrum requires large bandwidth, which results in high sampling rate. In the next chapter, an alternative solution that is based on the OFDM system will be discussed. This solution does not require a high sampling rate compared to the MC-DS-STDCC technique, and hence, the implementation is simple. Moreover, the OFDM-based sounder extracts channel information from the user transmit data such that no sounding signal generation is required.

Chapter 5

OFDM-Based Channel Sounder

5.1 Ultra Wideband Channel Sounder

An ultra-wideband (UWB) channel sounder can perform channel sounding across a very wide bandwidth of up to gigahertz. However, it has several potential problems when the FCC regulations are applied. A UWB channel sounder generates an extremely narrow pulse (i.e., nanoseconds) in the time domain, such as a Gaussian monocycle pulse [76], to record the reflected paths of the mobile radio channel. Although a UWB sounder can achieve high multipath delay resolution and spectrum utilization efficiency, narrow pulses suffer from the peak-to-average power (PAPR) problem, which requires large power amplifier dynamic range. Moreover, studies have shown that the UWB systems could cause interference with other systems [77,78]. Hence, pulse shaping must be applied to the pulse before being transmitted. However, to fit the transmitted signal spectrum under the FCC mask, sophisticated pulse shaping algorithms are required. Furthermore, when the UWB channel sounder is operated in the DSA network environment, where primary and secondary users are sharing the spectrum resource, more re-

striction, such as frequency band availability, will be added in addition to the FCC regulations, which could make pulse shaping infeasible or, at the cost of long computation time.

5.2 OFDM Systems Overview

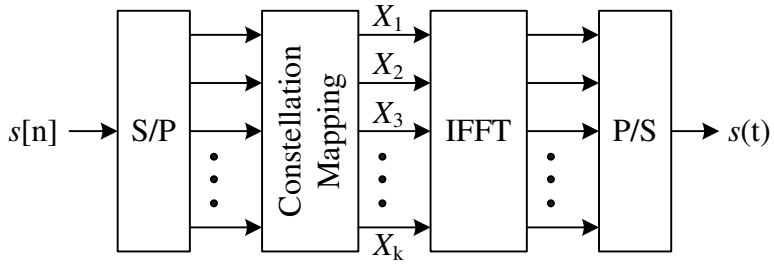

(a) OFDM transmitter.

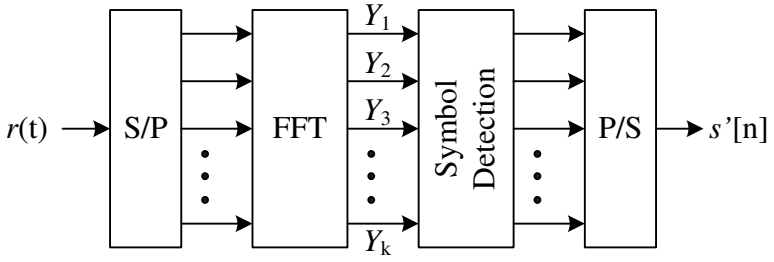

(b) OFDM receiver.

Figure 5.1. OFDM transceiver architecture.

OFDM systems use the spectrum resource more efficiently by transmitting data using orthogonal subcarriers. As shown in Figure 5.1, the serial data $s\,[n]$ stream is first converted to N parallel streams, where N is the number of subcarriers, each parallel data stream is modulated onto a different subcarrier. The mathematical expression is defined as the following:

$$s(t) = \sum_{k=0}^{N-1} X_k e^{j2\pi kt/T}, \quad 0 \leq t < T, \tag{5.1}$$

where X_k are the data symbols, T is the OFDM symbol time. The subcarrier spacing is defined as $1/T$, which makes them orthogonal over one symbol period.

The modulated parallel streams are transmitted after parallel to serial conversion. The receiver performs the reverse operation to recover the signal. The OFDM signal bandwidth is a function of the number of subcarriers as well as the subcarrier bandwidth. For example, an OFDM system of 1024 subcarriers with subcarrier bandwidth of 200 KHz will generate a total bandwidth of 200 MHz spectrum. If a UWB system is used to generate a 200 MHz bandwidth signal, it would require a 5 ns pulse in the time domain. The theoretical spectrum of an OFDM system is shown in Figure 5.2(a).

OFDM is considered as one of the major candidates for the DSA technology because of its spectrum efficiency and spectral robustness. In other words, the OFDM system can achieve spectrum shaping by adjusting the power level of certain subcarriers. In Figure 5.2(b), the relative transmit power level of an OFDM system is limited to 0, -20, -10, -5 dB across the restricted band respectively. To achieve OFDM spectrum shaping, the most straightforward way is to attenuate certain subcarrier power level. However, this approach requires prior information of the radio channel, which is feasible for the policy-based[1] DSA network. In an environment where spectrum accessibility and transmit power are totally determined by the user, a more agile approach is needed.

It can also be observed that the sidelobe power level exceeds the FCC limit. However, this can reduced by applying a sidelobe cancellation algorithm [79], which is beyond the scope of this work.

[1]The DSA networks are generally categorized into policy-based and nonpolicy-based, where the former requires full knowledge of the channel environment to function, and the latter does not.

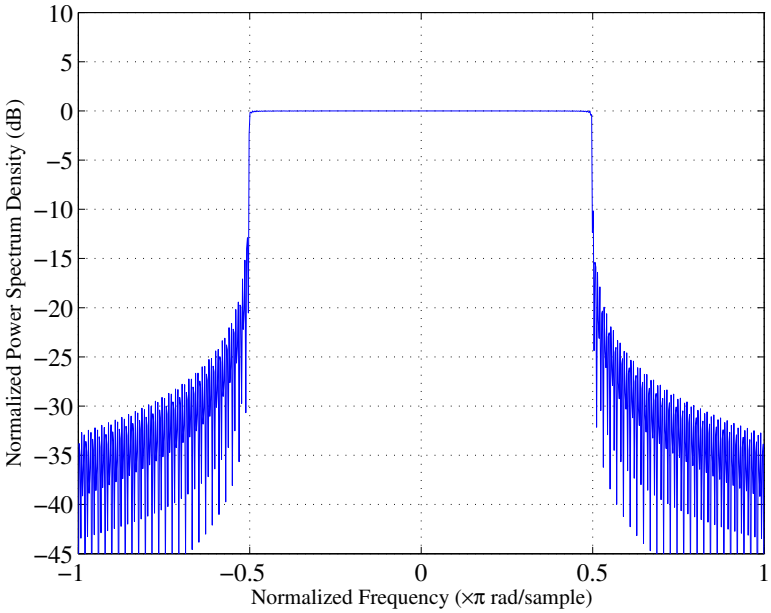

(a) Theoretical OFDM signal spectrum with 256 subcarriers.

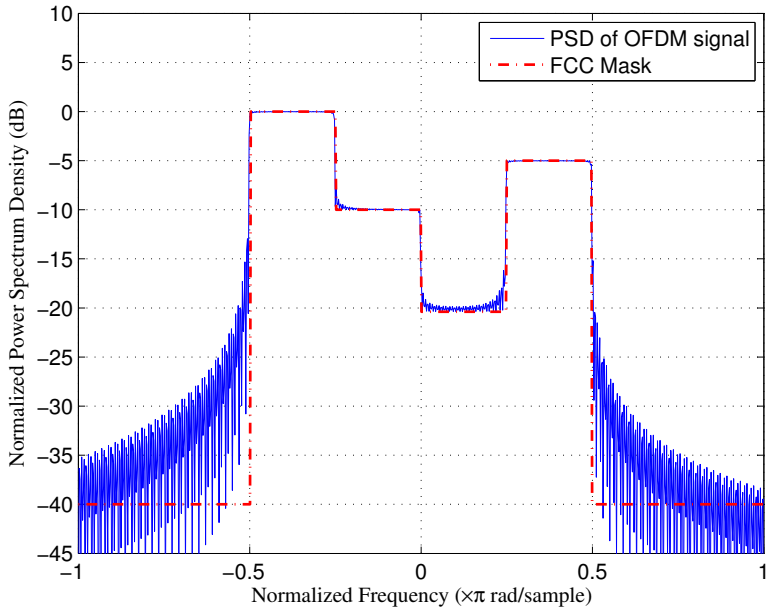

(b) OFDM signal spectrum with subcarrier power adjustment under the FCC mask

Figure 5.2. OFDM signal spectrum.

Considering the design perspective of a wideband channel sounder for the DSA network, the spectral robustness and efficiency feature of the OFDM system can be adapted. As mentioned in Chapter 4, the channel sounder operating in the DSA network has to introduce minimum amount of interference to the other users while maintaining sounding performance. Complexity in both hardware and software design is also critical. In the following section, an OFDM-based channel sounder will be discussed with focus on the aforementioned design considerations.

5.3 OFDM-Based Channel Sounder for Cognitive Radios

The motivation of designing an ideal channel sounder for the DSA network environment falls back to the basic principle of channel sounding, which is theoretically simple and easy to achieve. Hence, the question becomes how to approach the simple solution by not increasing the hardware complexity as well as software processing. Given a cognitive radio transceiver, the ideal design of such a sounder is to use the CR transceiver as a sounder, which is at no cost in terms of hardware and software design. Generally, the CR transceiver is not designed for such a purpose, which leads to the question of minimizing the modification of an existing CR transceiver.

As shown previously in Figure 2.4, the radio channel characteristics are closely related to each other. For example, the channel frequency correlation function and the power delay profile are a Fourier Transform pair, so are the Doppler power spectrum and the time correlation function. For the OFDM system, the baseband signal is generally considered as a "frequency domain" signal before the IFFT and after the FFT at the transmitter and receiver respectively. The signal is converted back and forth between the time and frequency domains during the entire trans-

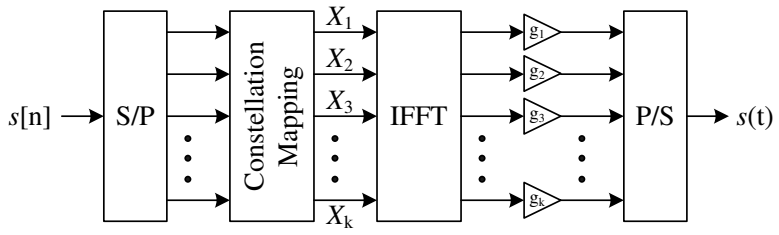

(a) OFDM sounder transmitter architecture.

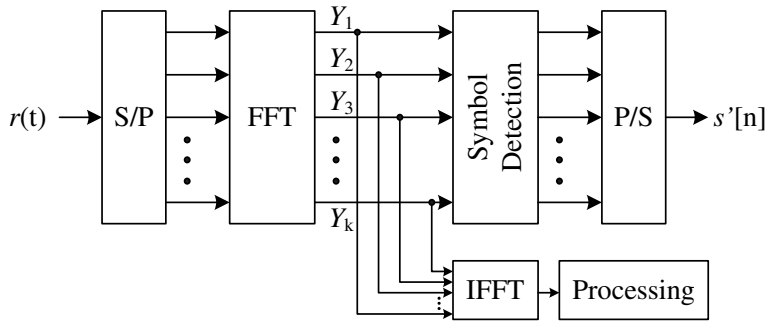

(b) OFDM sounder receiver architecture.

Figure 5.3. OFDM-based sounder transceiver architecture.

mission and reception. This feature provides a way of obtaining the time domain characteristic of the radio channel if the frequency domain characteristic can be captured by the OFDM transceiver. Ideally, the channel sounding device transmits an impulse to excite the radio channel, and the distorted signal is received at the receiver so that the multipath components are resolved.

Figure 5.3 demonstrates the system architecture for the OFDM-based channel sounder. For an OFDM transmitter, the serial data stream is converted into N parallel substreams and passed to the OFDM modulator. OFDM modulation is generally done by the IFFT [64], the signal before and after the IFFT is considered as frequency domain and time domain signal, respectively. The IFFT converts a frequency domain signal into time domain so that it can be used as the sounding signal. Theoretically, the inverse Fourier Transform of a band unlimited constant

amplitude signal is a delta function (impulse), which is impossible to achieve practically. However, a band limited signal with fairly large bandwidth in the frequency domain will provide a narrow pulse in the time domain. For example, a rectangular window with bandwidth of 100 MHz in the frequency domain is equivalent to a 10 ns pulse in the time domain. If this narrow pulse is transmitted over a multipath channel, it will provide a delay resolution of 10 ns. On each subcarrier, the power level is controlled by a tunable gain g_i before the signal is serialized and transmitted. The advantage of using tunable gain to adjust the power level of each subcarrier is simplicity compared to spreading for the MC-DS-STDCC system. However, a small power level will result in a CIR estimation degradation for the OFDM-based sounder.

At the receiver, the received signal is again converted into N substreams and demodulated with FFT, which transforms the time domain signal into frequency domain. The output of the FFT block is an estimation of the frequency correlation function. The time domain characteristics of the radio channel can be obtained by transforming the the output signal of the FFT block into the time domain using inverse Fourier Transform and time shifting.

Comparing Figures 5.1 and 5.3, the only addition to the OFDM transmitter is the tunable gain. On the receive side, the output of the FFT block is first extracted and stored on the computer, both the IFFT and postprocessing can be done off-line. Furthermore, the MC-DS-STDCC receiver also requires knowledge of the spreading sequence length used on each subcarrier in order to perform despreading, while the OFDM-based channel sounder does not perform such information exchange between the transmitter and the receiver.

5.3.1 System Parameters

In general, the OFDM-based channel sounding system parameters are minimum delay resolution, maximum detectable delay, dynamic range and processing time.

- Delay Resolution $\Delta\tau$.

  Similar to the conventional channel sounding systems, the minimum delay resolution is determined by the baseband sampling rate of the system. In this case, since the sounding signal is one OFDM symbol, the minimum delay resolution is equal to the inverse of the OFDM system baseband bandwidth, that is:

  $$\Delta\tau = \frac{1}{B_{\mathrm{s}}}. \tag{5.2}$$

- Maximum Detectable Delay $\tau_{\max}$.

  The maximum detectable delay is equivalent to one OFDM symbol period T_{s}. In a time-variant channel, where channel condition changes frequently, channel sounding has to be performed frequently in order to keep the channel information up-to-date.

- Dynamic Range D.

  Channel sounding performance is mainly affected by the dynamic range, the larger the dynamic range, lower the threshold can be set. The dynamic range of a sliding correlator based channel sounder is proportional to the m-sequence length, where the dynamic range is determined by the DFT size N for the OFDM-based channel sounder. The Discrete Fourier Transform

(DFT) is defined as:

$$X_k = \sum_{n=0}^{N-1} x_n e^{\frac{-2\pi i}{N} nk}, \quad k = 0, \ldots, N-1, \tag{5.3}$$

where x_n is the time domain discrete signal. If $x_n = 1, \quad \forall n$, the amplitude of $X_k = N$. Hence, the dynamic range in decibels is calculated as:

$$D_{\text{dB}} = 10 \log_{10} N. \tag{5.4}$$

Note that the contribution to the dynamic range only comes from the non-zero data points, if the sounding signal contains zeros, the dynamic range will be degraded, and hence Equation (5.4) becomes:

$$D'_{\text{dB}} = 10 \log_{10} N'. \tag{5.5}$$

More details on sounding singal design will be discussed in the following section.

- Processing Time.

  The processing time defines how long it takes for the system to complete the channel impulse response computation. Sliding correlator based channel sounder's processing time is a function of the m-sequence length M and the chip rate R_{c}. For example, a 4095-chip $(2^{12} - 1)$ m-sequence at chip rate of 32 Mcps needs $4095 \times 4095/32\text{e}6 \approx 0.5$ (s) to compute the channel impulse response across all phases of the entire m-sequence. Since the OFDM-based channel sounder does not require cross-correlation process at the receiver, the processing time is determined by the FFT algorithm. It is known that

the FFT reduces the number of operations from $O(N^2)$ for the DFT to $O(N \log N)$. For example, the USRP uses Altera Cyclone^{TM}FPGA. If the FPGA is running at 250 MHz, the processing time for a 4096-point DFT is equal to $4096^2/250e6 \approx 0.067$ (s), which is significantly shorter than the sliding correlator based channel sounder.

5.4 Sounding Signal and Performance

As discussed in the previous section, in order to design a suboptimal sounding signal, one has to transmit a constant envelop signal across one OFDM symbol, which is an ideal scenario for a unlicensed user. However, this approach is subject to subband availability and signal power level restrictions. Furthermore, dedicating transmission slots to the sounding signal reduces the user overall throughput and also increases the PAPR for the system. Our research shows that one can use the user data as the sounding signal to minimize the system overhead. Given a fixed bandwidth, the channel sounding accuracy, in terms of MSE, is a function of the number of subcarriers as well as the correlation factor of the user transmit data. In this section, the impact on the channel sounding accuracy caused by impairment of the sounding signal and using user data as sounding signal will be discussed, and a tradeoff study is conducted to identify the confidence of channel sounding accuracy.

5.4.1 Guaranteed Spectrum Availability

The channel sounding accuracy is limited by the signal transmit power or signal-to-noise (SNR) ratio when the spectrum availability is guaranteed. STDCC and MC-DS-STDCC channel sounder are promised to work under a low SNR

condition because of the inherent processing gain provided by the cross correlation and direct sequence spreading respectively. For the OFDM-based channel sounder, the signal reception only depends on the radio channel SNR.[2]

Transmitting a highly correlated sequence (i.e., N "1" s) increases the OFDM system peak-to-average power ratio [80]. This problem is more severe when frequent channel sounding is required. However, this approach gives the best performance in terms of sounding accuracy, and will be used as the baseline performance for comparison purposes. This drawback leads to a demand for another channel sounding signal design.

The properties of Fourier Transform as well as the resulting functions of certain time domain signals provide the solution. As mentioned previously, the FT of an infinite number of ones is an impulse in the frequency domain with zero width and infinite amount of energy. In practice, the energy can also be stored within a fairly short bandwidth if the time domain signal is long enough, which leads to a optimal sounding signal. Given certain number of subcarriers, N, the more number of ones transformed, the better the sounding signal and vice versa. On the other hand, if a certain OFDM symbol contains zeros, the magnitude of the resulting OFDM modulator output is a *sinc*-like function. Note that the definition of DFT is [64]:

$$X_k = \sum_{n=0}^{N-1} x_n e^{\frac{-2\pi j}{N} kn}, \quad k = 0, \ldots, N-1. \tag{5.6}$$

For a rectangular function x_n with total number of sample $M \leq N$, and assuming

[2]In general, the signal quality is also affected by the interference. For simplicity, it is assume that the sounding signal is not interfered with by other signals.

that M is odd:

$$x_n = \begin{cases} 1, & |n| \leq \dfrac{M-1}{2} \\ 0, & \text{otherwise} \end{cases},$$

the Fourier Transform X_k is:

$$\begin{aligned} X_k &= \sum_{n=0}^{N-1} x_n e^{\frac{-2\pi j}{N} kn} \\ &= \frac{\sin(\omega M/2)}{M \sin(\omega/2)} \\ &\approx \frac{\sin(\pi f M)}{\pi f}, \end{aligned}$$

where $\omega = 2\pi k/N$ and $f = k/N$. From the equation above, the $\text{sinc}(\cdot)$ function mainlobe width is $2 \cdot 2\pi/M$ radian, which is inversely proportional to the time domain number of samples M. We can define the sidelobe width $\Omega_M \triangleq 2\pi/M$, as M gets larger, the mainlobe width narrows, which improves the frequency resolution. However, the window size M has no effect on sidelobe level, it only changes the location of the zero-crossing points. The sidelobe height is instead a result of the abruptness of the window's transition from 1 to 0 in the time domain. This is the same thing as the so-called Gibbs phenomenon [64] seen in truncated Fourier series expansions of periodic waveforms. The mainlobe magnitude is always approximately 13 dB higher than the first sidelobe magnitude. The peak magnitude difference between the mainlobe and the first side lobe determines the dynamic range when channel sounding is performed with this signal. Hence the dynamic range for such a signal is 13 dB. However, the dynamic range can be improved by applying different window functions. The choice of window functions depends

on the system requirement such as channel SNR, channel sounding accuracy, etc. Another method for improving the dynamic range is pulse shaping. Pulse shaping is usually done by applying a raised-cosine filter on the input signal to reduce spectral leakage of the signal. Figure 5.4 compares the impulse response of a raised-cosine filter with different roll-off factors. The impulse response is a time domain parameter, but we desire a frequency response that is *sinc* function like. Since FFT and IFFT operations are reversible, the transforms themselves are identical except one is the time-shifted version of another, so the characteristics discussed here in one domain can also be projected to another. As can be seen, the sidelobe peak level decreases with the increase of the roll-off factor.

Another system parameter is the delay resolution. As discussed previously, the mainlobe width of the *sinc* function is equal to $2\Omega_M$ radian. For an N-point

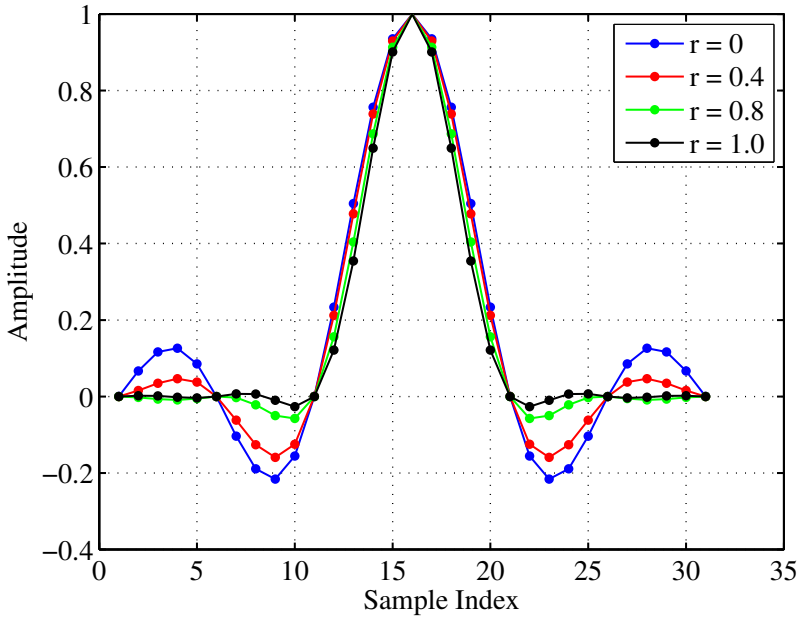

Figure 5.4. Impulse responses of a raised-cosine filter with roll-off factors of {0, 0.4, 0.8, 1}.

FFT with input chip rate of R_c, the delay resolution $\Delta\tau$ is defined as:

$$\Delta\tau = \frac{2\pi}{M} \cdot \frac{N}{R_c}. \tag{5.7}$$

For example, considering a time domain signal with a sampling rate of 32 Mcps, FFT size of 1024, and windows size $M = 512$, the minimum delay resolution is calculated as follows:

$$\begin{aligned}\Delta\tau &= \frac{2\pi}{M} \cdot \frac{N}{R_c} \\ &\approx \frac{6.28 \times 1024}{512 \times 32e^6} \\ &\approx 39\ \mu\text{s}.\end{aligned}$$

Equation (5.7) contains a fraction N/M, and $\min\{\frac{N}{M}\} = 1$. This indicates that the minimum delay resolution is only achieved when the fraction is equal to one. When the window size is equal to N, the window function is sampled at exactly all of it's zero-crossings, which gives the impression of an infinitely long sinusoidal sequence, hence the delay resolution is reduced to $2\pi/R_c$.

5.4.2 Non-Contiguous Band

A non-contiguous band generally refers to the subbands that do not share common borders. In other words, the target frequency band is divided into contiguous subbands due to frequency availability, transmit power restrictions, and spectrum owner restrictions. An illustration of a non-contiguous band is shown in Figure 5.5. For example, the measurement show that there is a strong signal appears between 400 MHz and 500 MHz band. If this band is to be used for chan-

nel sounding, the sounding signal has to avoid the frequency where the primary user appears. Non-contiguous bands introduce a new challenge for the sounding signal design, since the channel sounding needs to be done accurately as well as "quietly." As described previously, if the user data can be used as the sounding signal, no additional interference will be introduced to other users. Moreover, channel sounding can be performed more frequently (per OFDM signal period).

5.4.3 Sounding Signal Performance Analysis and Simulation Results

Based on Fourier Transform theory, if a given signal $x(t) = x(t+T)$ is periodic (temporal period T), its spectrum $X[n]$ is discrete (Fourier series with interval $\omega_0 = 2\pi/T$). If a given signal $x[m]$ is discrete (with temporal interval t_0 between

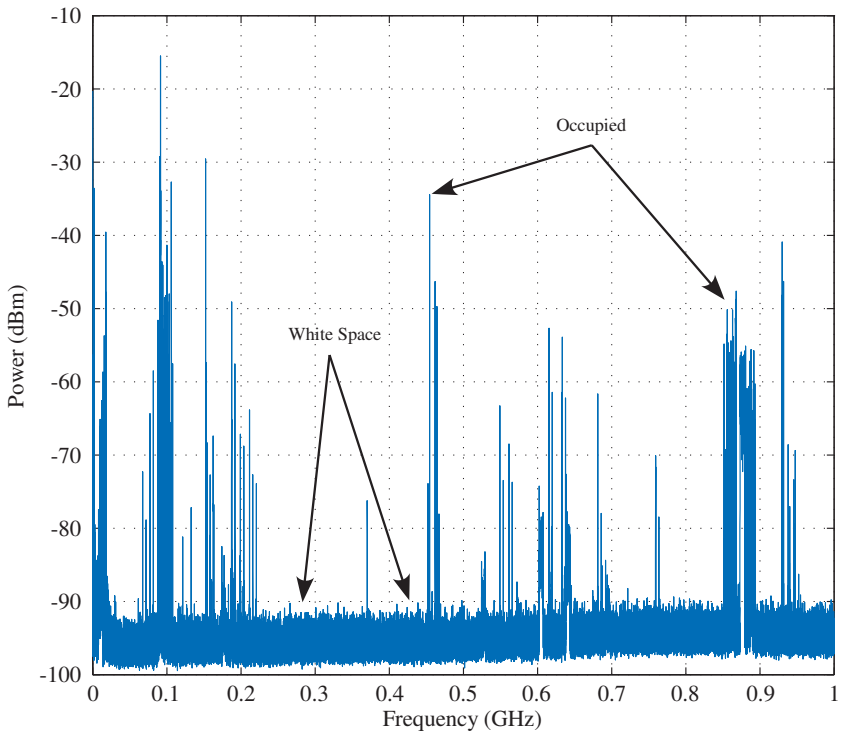

Figure 5.5. Spectrum occupancy measurements from 9 kHz to 1 GHz (8/31/2005, Lawrence, KS, USA).

samples), its spectrum $X(f)$ is periodic (frequency period $\Omega = 2\pi/t_0$). If a given signal is both periodic and discrete, its spectrum is periodic and discrete. In this case, the user data is used as the sounding signal, which is discrete but aperiodic, and we define ρ to be the percentage of "0"s in one OFDM symbol period, that is:

$$\rho = \frac{N'}{N}. \tag{5.8}$$

In order to investigate how channel sounding accuracy reacts when ρ changes, we define the Mean Squared Error (MSE) of the estimated channel impulse response as:

$$\text{MSE(t)} = \text{E}\left[\left(P_{\hat{c}_i}(\tau) - P_{c_i}(\tau)\right)^2\right], \tag{5.9}$$

where $P_{\hat{c}_i}(\tau)$ and $P_{c_i}(\tau)$ are the estimated and actual power of the channel impulse responses respectively. In Equation (5.9), $(P_{\hat{c}_i}(\tau) - P_{c_i}(\tau))$ is defined as residual, or estimated error ϵ_i, which is the difference between the observed data and fitted model. In an ideal case, where the estimated error is only caused by the channel noise, the MSE is a function of the channel SNR and the dynamic range. Assuming BPSK modulation, ϵ_i can be represented by the complementary error function:

$$\epsilon_i = \frac{1}{2} erfc\left(\sqrt{\frac{E_b}{N_0}}\right), \tag{5.10}$$

and hence, Equation (5.9) can be rewritten as:

$$\text{MSE} = -(\text{DR} + \text{SNR}). \tag{5.11}$$

For a multipath fading channel, both power attenuation and multipath delay distribution will affect the accuracy of the CIR estimation. Furthermore, the

error estimation accuracy also depends on how the threshold is chosen. Higher threshold will limit the amount of noise during the estimation process. However, the multipath component with weak signal strength might be left out, which degrades the accuracy. Assume that all the multipath components can be resolved for a given threshold R, and the envelop of the channel impulse response has a Rayleigh probability density function:

$$f_R(r) = \frac{r}{\sigma^2} e^{-r^2/\left(2\sigma^2\right)}, \tag{5.12}$$

where σ^2 denotes the time-average power of the received signal. The probability that the received signal does not exceed a specified value R is given by the corresponding cumulative distribution function (CDF) [45]:

$$P(R) = P_r(r \leq R) = \int_0^R p(r)\mathrm{d}r = 1 - e^{-R^2/\left(2\sigma^2\right)}. \tag{5.13}$$

Let $\bar{\gamma}$ be the average E_b/N_0 for a Rayleigh fading channel, and $\bar{\gamma}$ is defined as [81]:

$$\bar{\gamma} = \frac{E_b}{N_0}\left[a^2 + 2\sigma^2\right], \tag{5.14}$$

where $a^2 + 2\sigma^2$ is the average power of the signal envelop. Based on Equation (5.14), the MSE for a Rayleigh fading channel is given by:

$$\mathrm{MSE} = -(\mathrm{DR} + \bar{\gamma}). \tag{5.15}$$

Figures 5.6 and 5.7 show a set of snapshots of the estimated channel impulse responses versus the actual channel impulse responses generated by the simula-

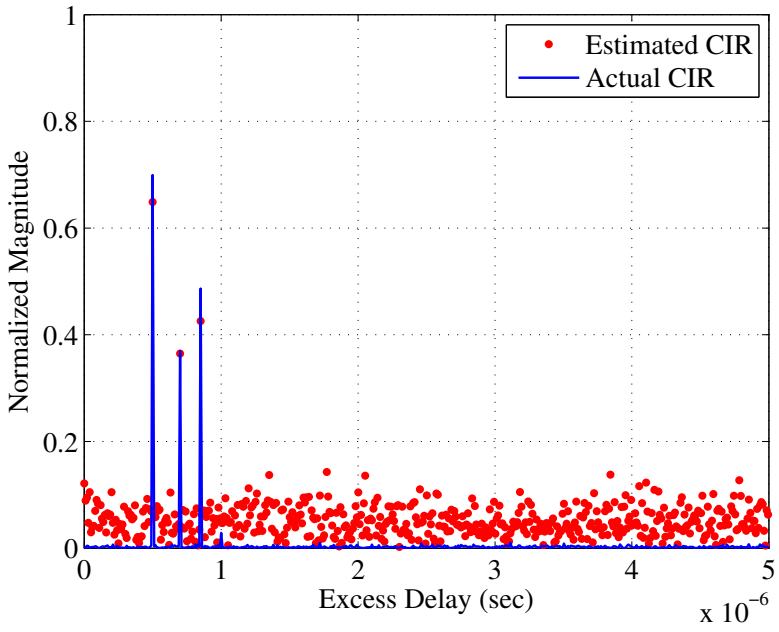

(a) $N = 1024$.

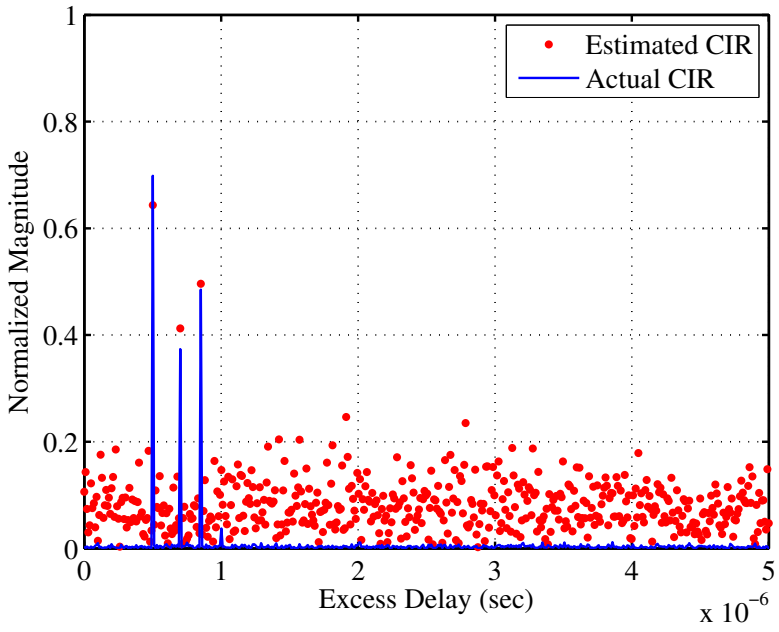

(b) $N = 512$.

Figure 5.6. Snapshot of an estimated CIR versus actual impulse response. $\rho = 0.8$; SNR=20 dB; path delays = {0.5, 0.7, 0.85, 1} μs; N={512,1024}.

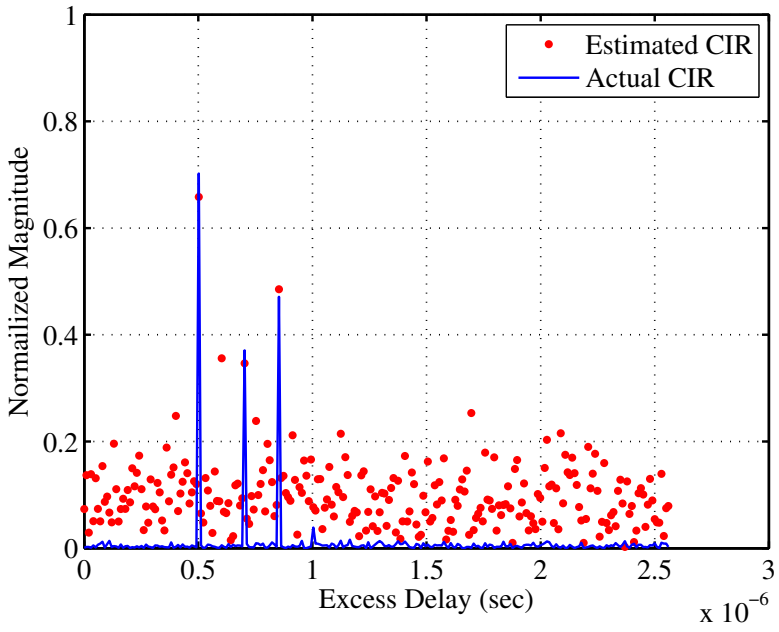

(a) $N = 256$.

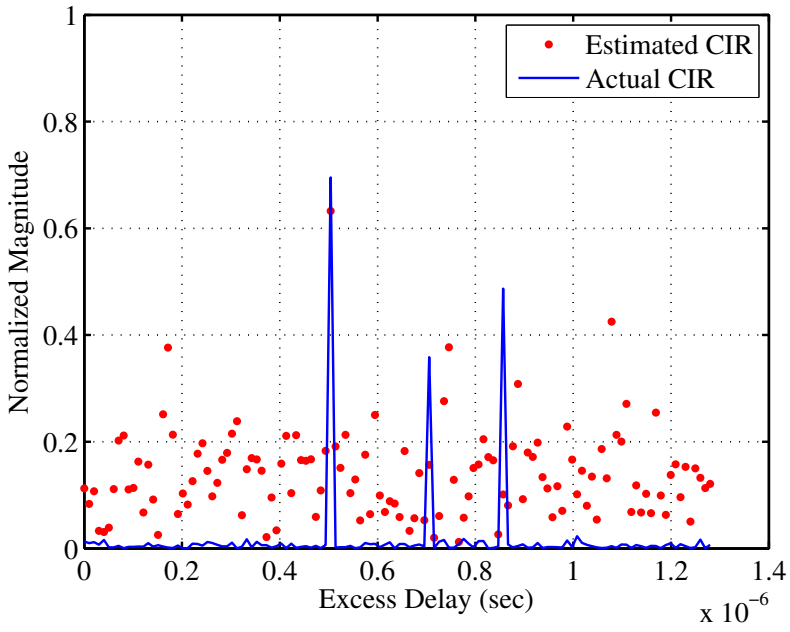

(b) $N = 128$.

Figure 5.7. Snapshot of an estimated CIR versus actual impulse response. $\rho = 0.8$; SNR=20 dB; path delays = {0.5, 0.7, 0.85, 1} μs; N={128,256}.

tor. The simulation results are collected under the following system parameters: SNR = 20 dB, $\rho = 0.8$, $N = \{1024, 512, 256, 128\}$, channel path delays = {0.5, 0.7, 0.85, 1} μs. The actual delays are displayed instead of considering the first path delay to be zero. Comparing the estimated channel impulse responses for different N values, it is obvious that under the same channel condition, larger N value delivers greater dynamic range. For $N = \{1024, 512\}$, the first three multipath components delays are clearly resolved but the amplitudes are off. This is because a large ρ value is used. The last multipath component is not detected since the noise power is dominating over it at this time instance. In Figure 5.6(b), the first three multipath delay components are identified. However, a false alarm may occur due to the presence of the data point between the first and the second multipath delay. For $N = 128$, the estimated CIRs are too close to the noise floor to be clearly identified. Moreover, the baseband bandwidth B and noise power spectral density N_0 are identical for all cases, hence the noise floor rises as the number of subcarriers reduces, which results in poor estimation in terms of multipath component identification. For instance, the noise floor rises approximately 2 to 3 dB when comparing Figure 5.6(a) with 5.7(b).

Assume that the minimum delay of the multipath fading channel is greater than the OFDM channel sounder delay resolution $\Delta\tau$, and the maximum delay $\tau_{\max}$ is less than one OFDM symbol period. Based on this assumption, given an ideal sounding signal (impulse), the MSE should hold a linear relationship with the SNR. Simulation results (i.e., Figure 5.8) reveal the relationship between channel sounding accuracy and ρ. The simulations were conducted under identical system parameters and channel conditions for each ρ value, each curve is averaged over 40 random realizations, and the system parameters are summarized in Table (5.1).

Table 5.1. OFDM sounder simulation parameters.

Chip rate (R_c)	100 Mcps
Number of subcarriers (N)	1024
Channel type	Rayleigh fading channel
Maximum Doppler shift	100 Hz
Multipath delays	0, 100, 200, 400 ns
Average attenuation (dB)	0, -3, -8, -12 dB
SNR (dB)	-10 to 20 dB
ρ	0, 0.2, 0.4, 0.6, 0.8

As shown in the figure, the MSE performance decreases as ρ increases for almost the entire SNR range. At small SNR values (-10 to -5 dB), the noise power is dominating, the curves are close to each other. As SNR increases, the MSE curves start to split. It is noticed that when ρ is equal to 0, the MSE performance improves linearly as SNR(dB) increases, which matches the analysis.

The same trends can be observed from Figures 5.9, 5.10, and 5.11. The MSE curves reach a certain error floor for all ρ values except for $\rho = 0$, and the error floor increases as N decreases. This is because the dynamic range reduces as the number of subcarriers gets smaller.

Figure 5.12 compares the theoretical MSE with the simulation results for different N values. It is clearly seen that all four curves are almost parallel to each other, which proves the fact that the MSE performance degrades as the number of subcarriers decreases for a given SNR value (i.e., Figures 5.6 and 5.7). For SNR equal to 10 dB, the MSEs for $N = \{128, 1024\}$ are -28.93 dB and -40.01 dB, respectively, and the difference is approximately 11 dB. Analytically, the performance degradation caused by the dynamic range reduction is equal to

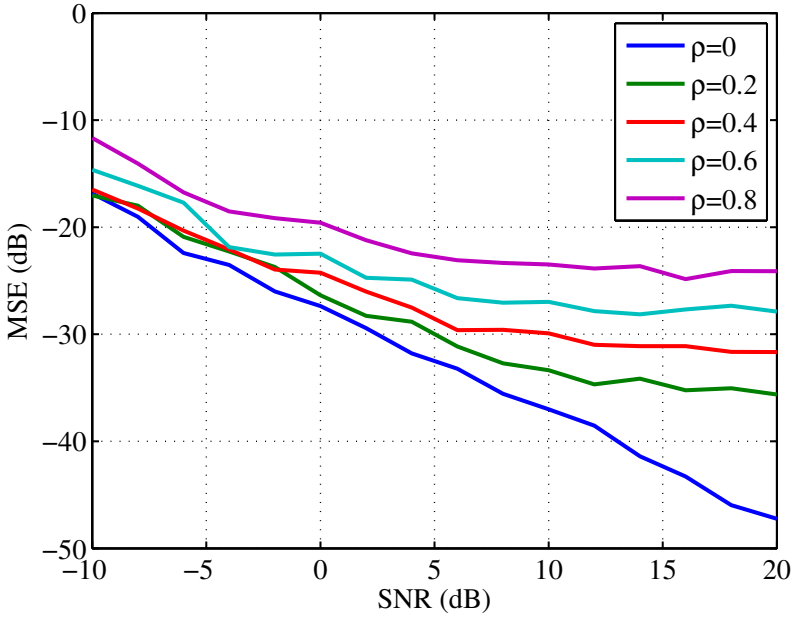

Figure 5.8. OFDM sounder Mean Squared Error (MSE) performance. $N = 1024$, $\rho = \{0, 0.2, 0.4, 0.6, 0.8\}$.

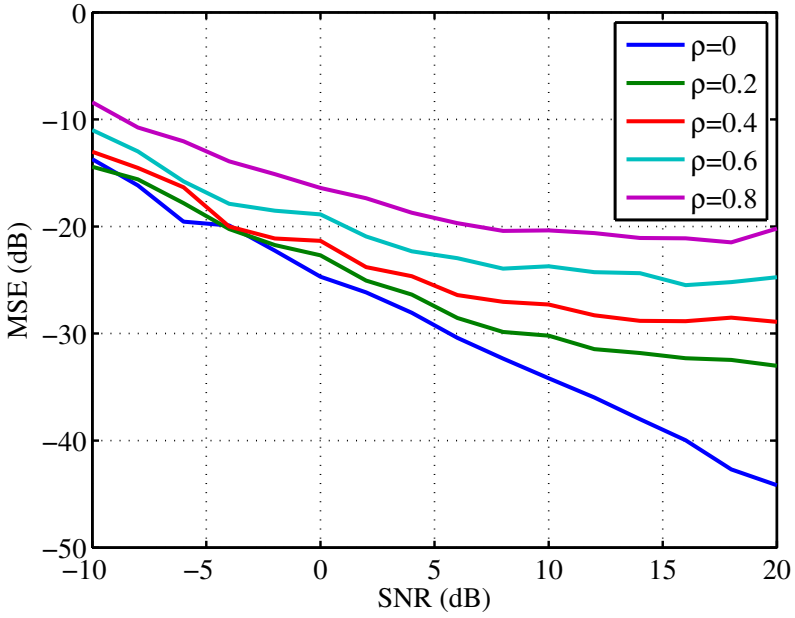

Figure 5.9. OFDM sounder Mean Squared Error (MSE) performance. $N = 512$, $\rho = \{0, 0.2, 0.4, 0.6, 0.8\}$.

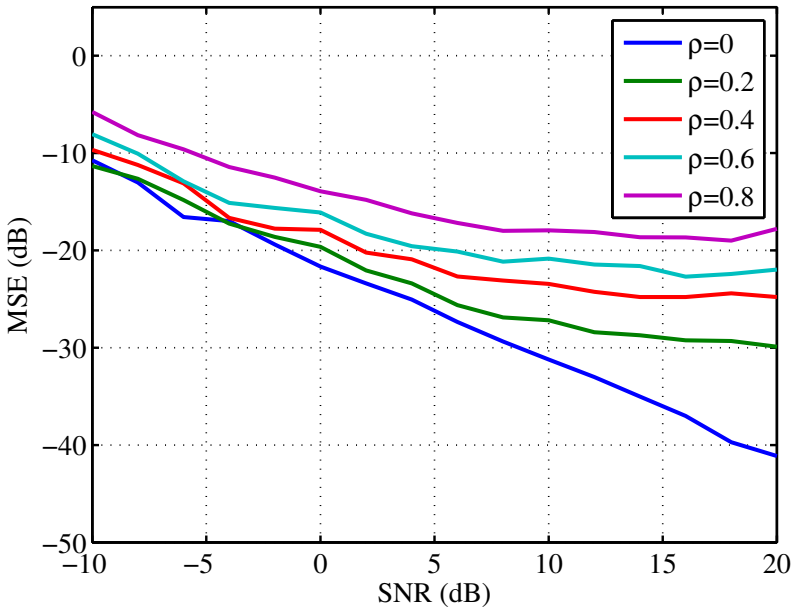

Figure 5.10. OFDM sounder Mean Squared Error (MSE) performance. $N = 256$, $\rho = \{0, 0.2, 0.4, 0.6, 0.8\}$.

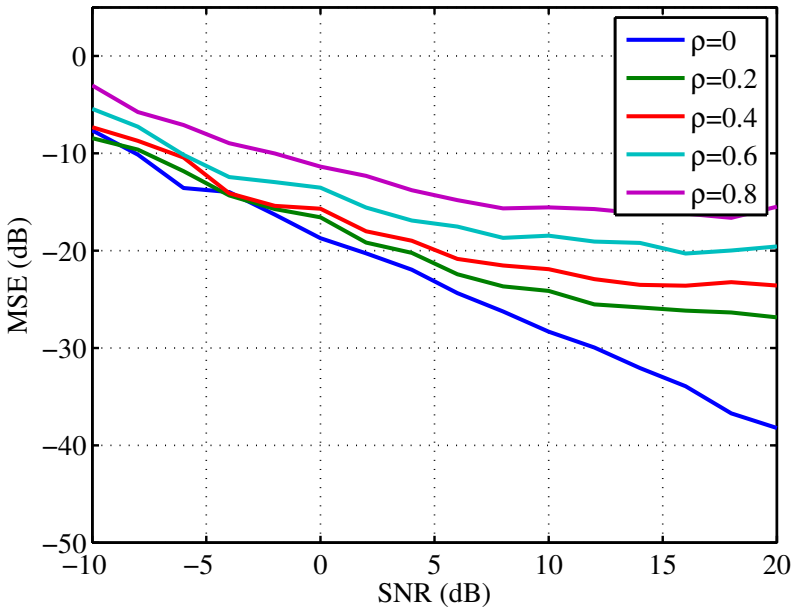

Figure 5.11. OFDM sounder Mean Squared Error (MSE) performance. $N = 128$, $\rho = \{0, 0.2, 0.4, 0.6, 0.8\}$.

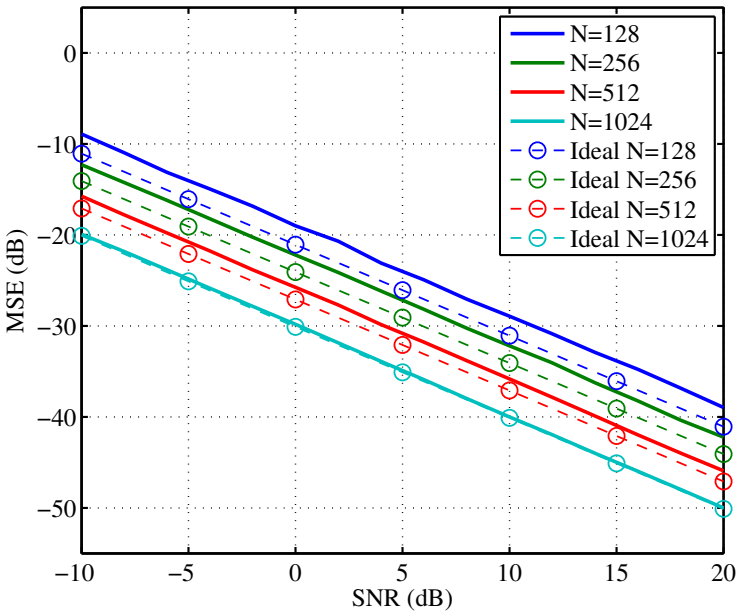

Figure 5.12. OFDM sounder Mean Squared Error (MSE) performance. $N = \{128, 256, 512, 1024\}$, $\rho = 0$.

$10\log_{10}(1024) - 10\log_{10}(128) \approx 9$ dB. The 2 dB difference is caused by the noise floor raise for different N values as discussed previously. Figure 5.12 is a better demonstration of the linear relationship between the MSE of the estimated CIR and the signal-to-noise ratio. The MSE for $N = 1024$ is observed to be -20 dB at SNR of -10 dB, which decreases to roughly -50 dB when the SNR increases to 20 dB. Note that with larger N values, e.g., $N = 1024$, the simulation results are almost identical to the theoretical results. This is because larger N value provides better delay resolution than smaller N values, and hence, the error is primarily caused by the noise.

5.5 Chapter Summary

In this chapter, a novel channel sounding technique based on OFDM transceiver architecture is presented. The proposed OFDM channel sounder is specifically designed for cognitive radios and dynamic spectrum access network environment. The OFDM channel sounder achieves interference awareness by taking advantage of the multicarrier modulation techniques. It utilizes user transmission data as the sounding signal, hence, no extra interference is introduced to other users by performing channel sounding. Furthermore, a signal processing algorithm that extracts the multipath channel characteristics is developed. This algorithm's target is minimizing system complexity as well as maintaining channel sounding performance. Channel sounding performance is studied analytically, and simulation results are provided in supporting the analysis. The proposed technique is also evaluated for the future use in different channel environments. A tradeoff study between channel sounding performance and system complexity is conducted, which can be used as system design guideline.

Chapter 6

Implementation of STDCC Channel Sounder

In this section, several implementation issues will be discussed in detail. Both the STDCC and the OFDM-based channel sounder implementations were executed on the Universal Software Radio Peripheral (USRP) [12] hardware platform. The signal processing and postprocessing functionality blocks are implemented in the GNU Radio [82] software, an open source software radio.

6.1 USRP Hardware Prototyping Platform

The USRP, shown in Figure 6.1, is developed by Ettus Research LLC. It allows us to create a software radio using any computer with USB 2.0 and Gigabit ethernet ports. The operation center frequency can be changed by switching different daughter boards, in our case, the RFX 2400 daughter board is used. This daughter board offers a center frequency range from 2.3 GHz to 2.9 GHz with maximum output power of 50 mW (17 dBm). The USRP mother board

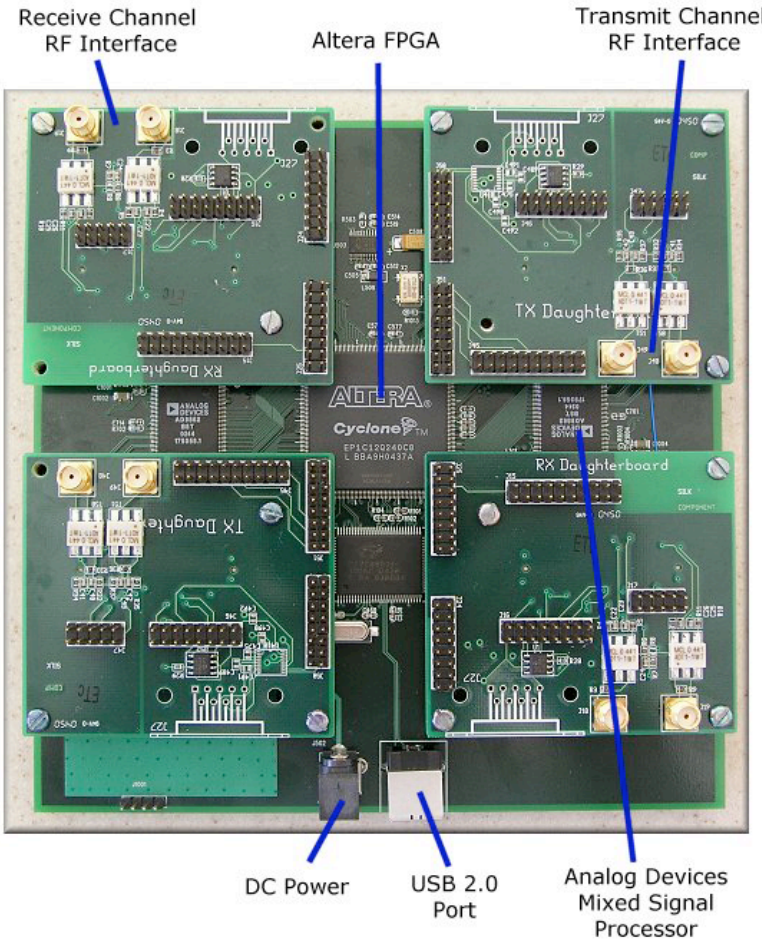

Figure 6.1. Universal Software Radio Peripheral mother board equipped with four of daughter boards.

contains an Altera Cyclone EP1C12 Field Programmable Gate Array (FPGA). It has four high-speed analog to digital converters (ADCs), each running at 12 bits per sample, which is 64 MSamples/sec, and also four high-speed digital to analog converters (DACs), each at 14 bits per sample, 128 MSamples/sec.

Figure 6.2(a) and 6.2(b)[1] show the block diagrams of the transmit and receive path for RFX 2400 daughter board used by this measurement. For complete specifications of the RFX 2400 daughter board, see [12]. As we notice, there exists

[1]Block diagrams shown here are modified based on the original ones due to typos, original diagrams can be found [83].

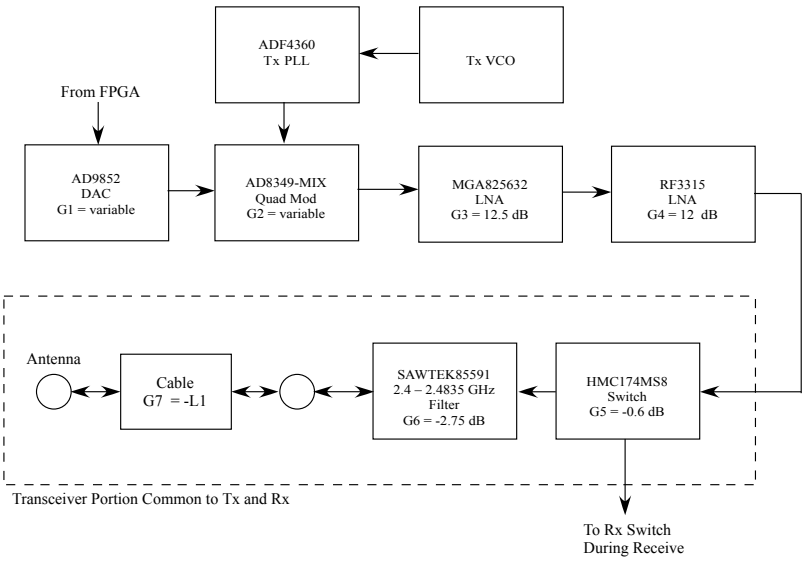

(a) RFX2400 Transmit path.

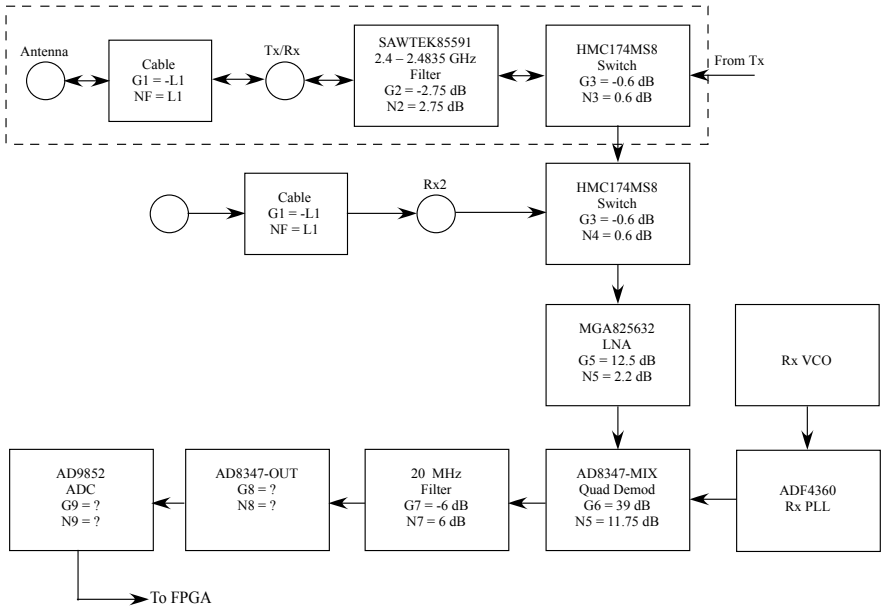

(b) RFX2400 Receive path.

Figure 6.2. RFX2400 daughter board transceiver signal flow diagram.

a bandpass filter on both the transmit and receive path between the antenna and the Low Noise Amplifier (LNA), which limit the center frequency range to 2.4 to 2.4835 GHz. Hence, all experiments were conducted within this center frequency range. The maximum baseband bandwidth is about 20 MHz, because of the usage of a 20 MHz lowpass filter. The maximum bandwidth that the USRP supports is 256 Mbps; this is because the USB 2.0 is sustained to this value. This indicates that 8-bit samples can provide 16 MHz bandwidth, while 4-bit samples will provide a bandwidth of 32 MHz, if a complex signal is used, each I and Q signal occupies half of the whole USB bandwidth. Practically, this bandwidth is not ideal for the implementation of the proposed channel sounder, since the maximum delay resolution that can be provided is equal to:

$$\frac{2}{32 \times 10^6} = 62.5 \ n\text{s},$$

which requires a minimum separation between the transmitter and receiver to be $62.5 \times 10^{-9} \times 3 \times 10^8 = 18.75$ (m) in order to resolve the minimum delay. Saleh and Valenzuela reported the results for indoor propagation measurements in [84]. They reported a maximum multipath delay spread of 100 ns to 200 ns within rooms of a building, and 300 ns in hallways without line-of-sight path between the transmitter and the receiver. The measured *rms* delay spread within rooms had a median of 25 ns and a maximum of 50 ns, which is shorter than the minimum delay resolution provided by the USRP sounder. It was also reported that the large-scale path loss obeys a log-distance power law [45], which is:

$$\overline{PL}(\text{dB}) = \overline{PL}(d_0) + 10n \log\left(\frac{d}{d_0}\right), \tag{6.1}$$

where n is the path loss exponent which indicates the rate at which the path loss increases with distance, d_0 is the close in reference distance which is determined from measurements close to the transmitter, and d is the transmitter-receiver separation distance. For in building line-of-sight (LOS), n varies from 1.6 to 1.8, and for obstructed in building environment, n is equal to 4 to 6. If we assume that the reference distance d_0 is 1 meter, and the measured power at d_0 is equal to the equivalent isotropically radiated power (EIRP), then the path loss $\overline{PL}$ with transmitter-receiver separation of 18.75 meters is approximately equal to 2 and 5 dB for LOS and non-LOS, respectively.

6.1.1 Signal Processing

The USRP is in charge of the RF front end, Intermediate Frequency (IF) processing, such as decimation, interpolation, etc. Once the signal is in the baseband domain, it is processed by the FPGA running GNU Radio software. GNU Radio is a free software development toolkit that provides the signal processing runtime and processing blocks to implement software radios using readily-available, low-cost external RF hardware and commodity processors [82]. Specifically, all performance-critical signal processing functionalities are written in C++, and system level applications are done in Python programming language. In our case, since all the required signal processing functions are already written by researchers and GNU Radio contributors, only Python programming is needed. In addition to the GNU Radio software, MATLAB is used for most of the post signal processing, graphing and Graphical User Interface (GUI) design.

The onboard baseband filter (20 MHz bandwidth) is enabled by default, which reduces the delay resolution performance by 37.5%. In order to perform channel

sounding measurement across the entire 32 MHz bandwidth, researchers have developed a custom FPGA bitstream that is able to generate and receive a sounder waveform across a full 32 MHz wide bandwidth. The waveform generation and impulse response processing occur in logic in the USRP FPGA and not in the host PC. This avoids the USB throughput bottleneck entirely as well as bypassing the baseband filter. However, the OFDM-based channel sounder implementation does not have the ability to bypass the USB throughput bottleneck. Hence, the maximum bandwidth is limited to 20 MHz instead of 32 MHz.

6.2 Implementations of STDCC

In this section, the details of the implementations of the STDCC will be presented and experiment results will be analyzed. As discussed in Chapter 4, the MC-DS-STDCC channel sounder requires a much higher sampling rate than what the USRP can offer. Hence, the implementation becomes infeasible on the USRP hardware platform. Moreover, the USRP transmitter and receiver clock synchronization are not implemented by the designer of the USRP, which results in a random time shift when the received m-sequence is cross-correlated with the locally generated m-sequence. This issue causes inaccurate absolute multipath delays, but relative delay estimations are still valid as far as the channel impulse response is concerned. If we can assume that the first multipath component always contains the most power, one can time shift the correlated sequence to reserve a zero lag for the first multipath component.

Since we discovered that the clock synchronization may affect the sounding results, we need to validate that the sounding sequences are transmitted continuously without any unwanted bits between the sequences. To do this, we con-

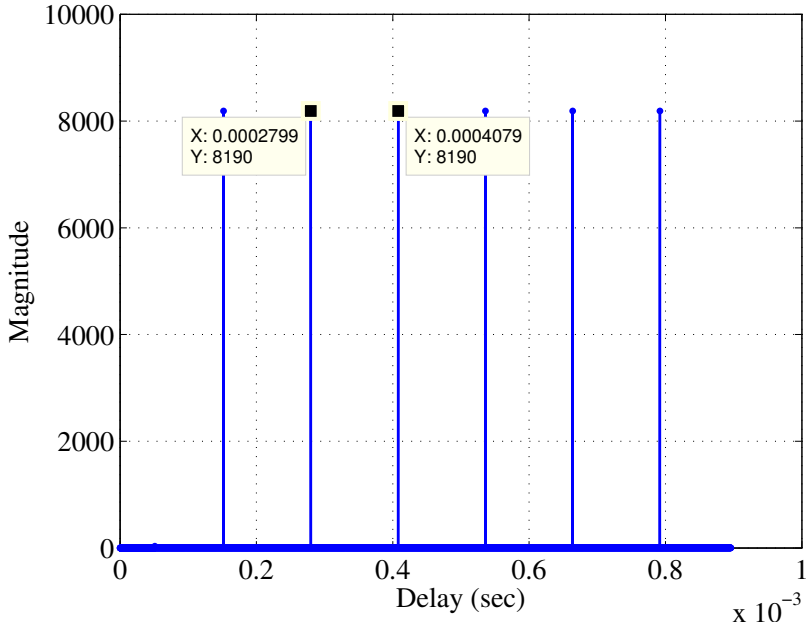

Figure 6.3. Channel impulse responses of a loopback test with 4095-chip m-sequence.

ducted two simple loopback tests. The first loopback test was conducted within one USRP, an m-sequence is transmitted and routed back directly without going through any other function blocks, then the loopback sequence is cross-correlated with itself (autocorrelation). Intuitively, the resulting cross-correlation function should contain a set of impulses with separation of $2^m - 1$ chips, where m is the degree of the m-sequence. Figure 6.3 shows an output of the cross-correlator with 7 cycles. Each m-sequence occupies approximately 128 μs. As can be seen from the data tips in the figure, the delay between the second and the third impulse is exactly 128 μs. This test verifies that the same m-sequence is transmitted continuously over time. However, the appearance of the first impulse is random as discussed previously. This test also validates that the buffer is long enough to handle the entire process.

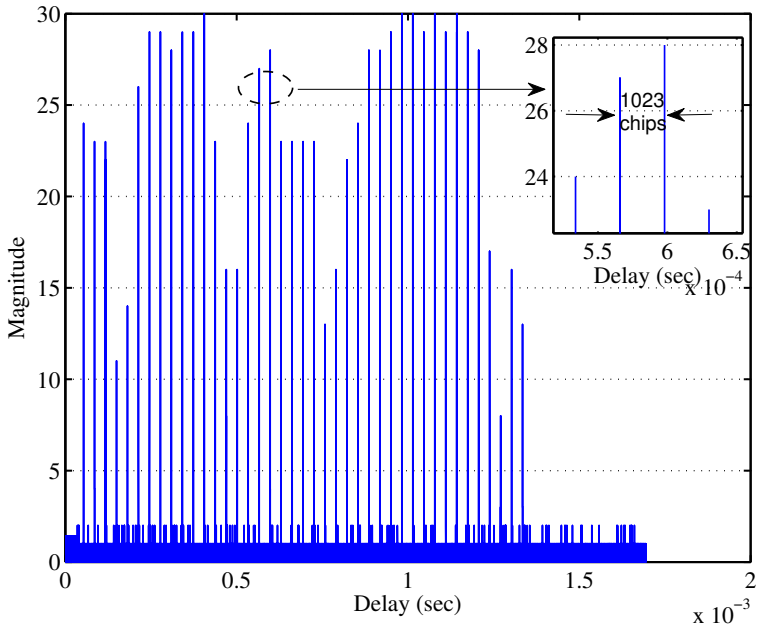

Figure 6.4. Estimated channel impulse responses between two USRPs with 1023-chip m-sequence.

The second test was conducted between two USRP boards, the daughter boards used were BasicTX and RX for the purpose of simplicity and avoiding unnecessary interference. For this test, two daughter board antennas are connected directly using a SMA-SMA RF cable, and a 40 dB attenuator is inserted to avoid the receive power from exceeding the maximum value. Detailed specifications of this operation can be found in [12]. The test result is shown in Figure 6.4. From the close-up figure we can see that the impulse separation remains the same as the sequence length. It is also noticed that, the magnitudes are fluctuating for each cycle, where the magnitude is constant for each cycle in Figure 6.3. Moreover, noise is present in this case since a real channel is added. The magnitude fluctuation is caused by summation of the background noise, insertion loss of the device including daughter boards, RF cable, etc.

6.2.1 In Building Setup and Measurements

In this section, we will discuss the channel impulse response measurements by using the STDCC. All measurements were conducted inside Nichols Hall at the University of Kansas, Lawrence, KS, USA. We consider both LOS case and non-LOS case in our study. As discussed previously, due to the synchronization issue, the CIR measurements need to be time-shifted in order to recover the real CIR. This is only feasible only for the LOS case, since we cal always assume that the first path has the strongest power. For the non-LOS case, the strongest path may arrive with longer delays, and the time-shifting technique does not work any more. In this case, only the relative delay between multipath components will be studied. The measurements were conducted on the second floor of Nichols Hall, both the transmitter and receiver are stationary, and the transmitter is set up in room 240 on the east side of the building, and the receiver is located on the opposite side in the hallway. The transmitter and receiver separation is approximately 164 feet (50 meters) so that the minimum delay resolution is guaranteed. Both transmitter and receiver use an RFX 2400 daughter board and 2400 to 2480 MHz ISM band vertical omni-directional antenna with 7 dBi gain [12]. The center frequency is tuned to 2.44 GHz in order to fit the antenna and the bandpass frequency range.

As mentioned before, the bandpass filter limits our operation center frequency range to 2.4 to 2.483 GHz, to prove that the filter is affecting the measurement results, Figures 6.5 and 6.6 show the sounding signal spectrum at 2.4 and 2.5 GHz respectively, and the signal bandwidth is equal to 32 MHz. As we can see, the spectrum within the filter range has a higher power level than the portion that is outside the filter range. There exists a way to bypass the filter by modifying the RFX 2400 daughter board. However, this approach is not considered due to the

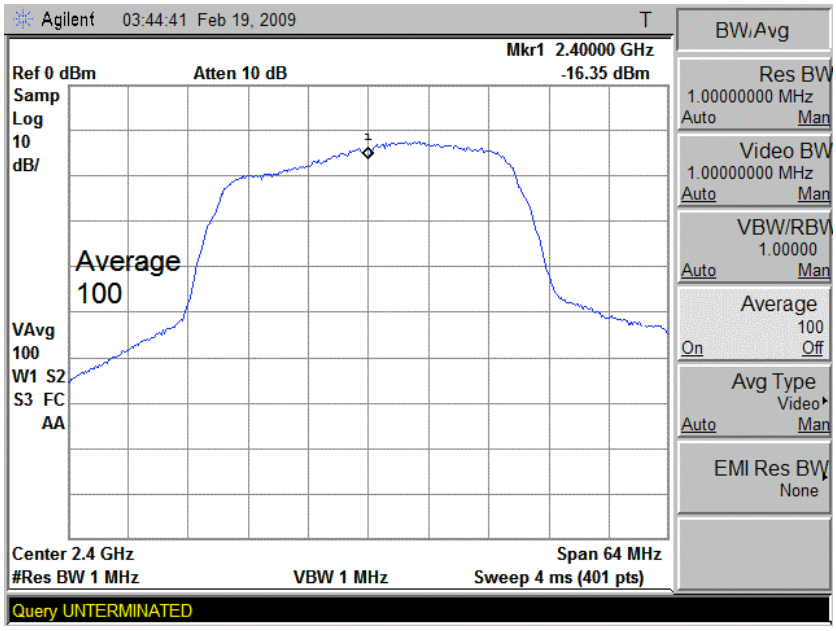

Figure 6.5. Sounding signal spectrum at center frequency of 2.4 GHz

risk of damaging the board.

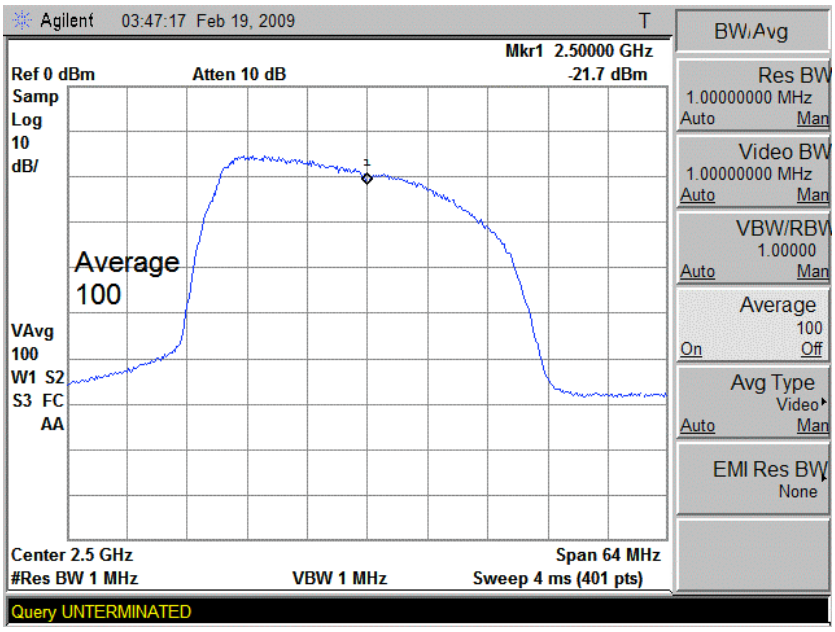

Figure 6.6. Sounding signal spectrum at center frequency of 2.5 GHz

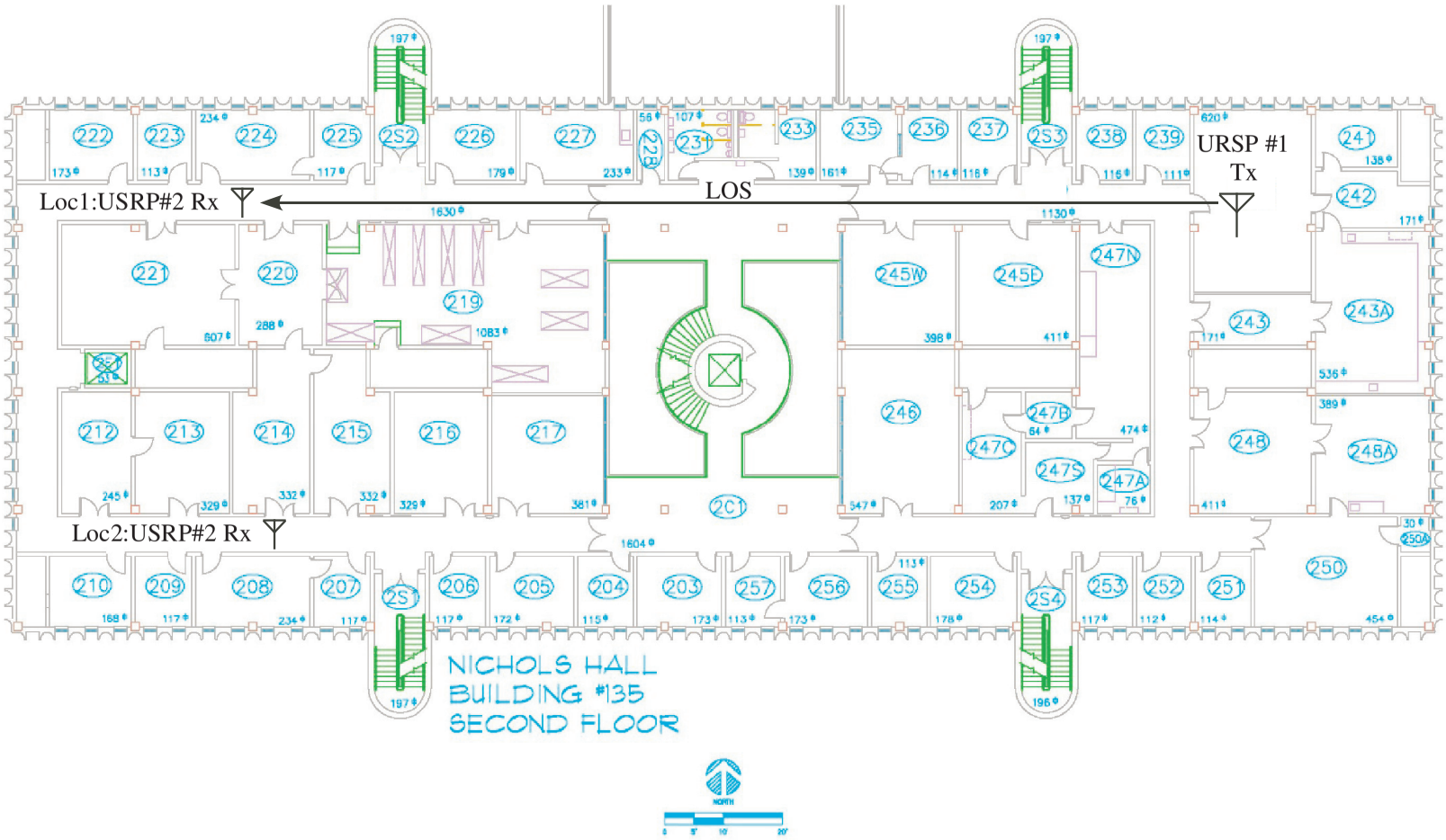

Figure 6.7. Demonstration of the in-building environment for the channel sounding measurements.

Figure 6.7 demonstrates the channel impulse response measurement model as well as the possible paths. Note that the radio channel not only contains LOS path, but also reflected paths from the walls around the transmitter and receiver. For an indoor environment, a transmitted signal may be reflected multiple times before it arrives at the receiver. The signal strength will be weakened but still strong enough to be resolved by the receiver, and each reflected path has a delay associated with it. Analytically, due to the inherent processing gain provided by the STDCC channel sounder, more multipath components should be observed with relatively short delays and small variations in terms of signal strengths. The system parameters are summarized in Table (6.1):

Table 6.1. STDCC channel sounding measurement parameters.

Baseband bandwidth	8 - 32 MHz
Modulation	BPSK
m-sequence length	255 - 4095 chips
Daughter board	RFX 2400
Antenna	ISM band vertical omni-directional
Center frequency	2.44 GHz
DAC output level	4096 - 32000
GNU Radio software version	3.1.2
Operating system	Fedora 8 and Mac OS X
Radio channel type	In-building
Scenario 1	50 meters with LOS (Fig. 6.7)
Scenario 2	56 meters without LOS (Fig. 6.7)

Figures 6.8 to 6.16 show the measured channel power spectrum of the USRP channel sounder with various DAC output levels.

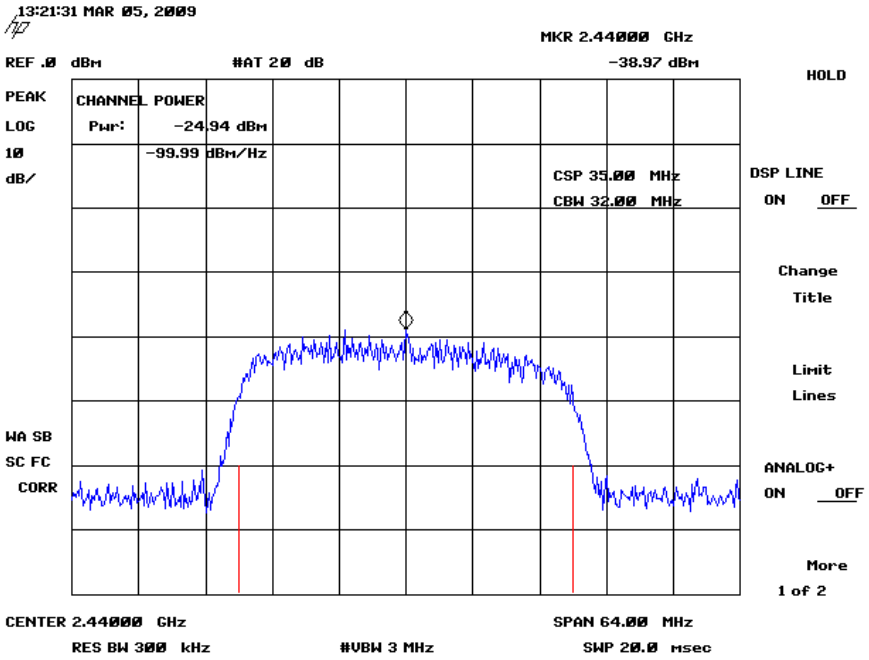

Figure 6.8. Measured channel sounding signal power with RFX2400 daughter board; amplitude=256.

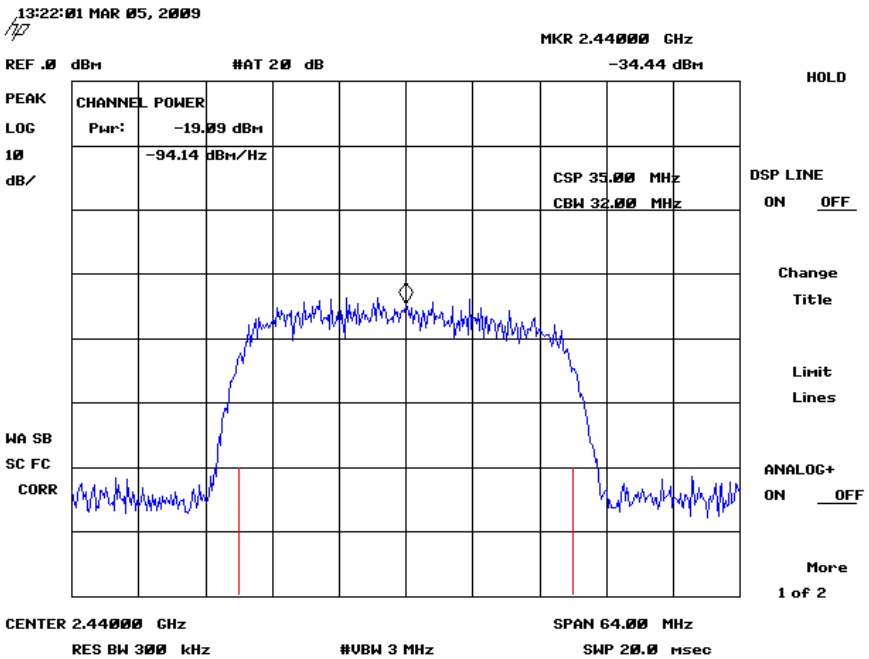

Figure 6.9. Measured channel sounding signal power with RFX2400 daughter board; amplitude=512.

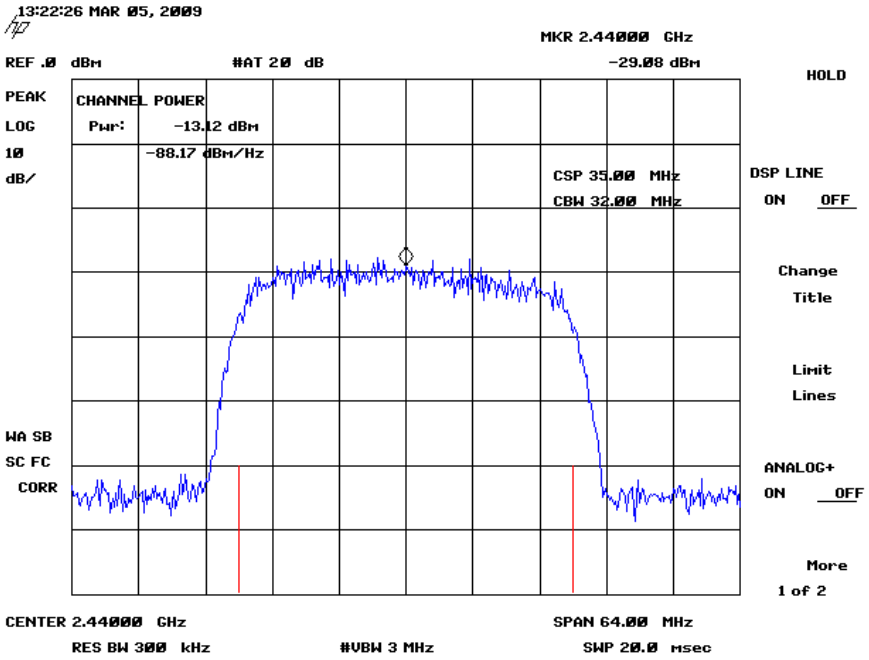

Figure 6.10. Measured channel sounding signal power with RFX2400 daughter board; amplitude=1024.

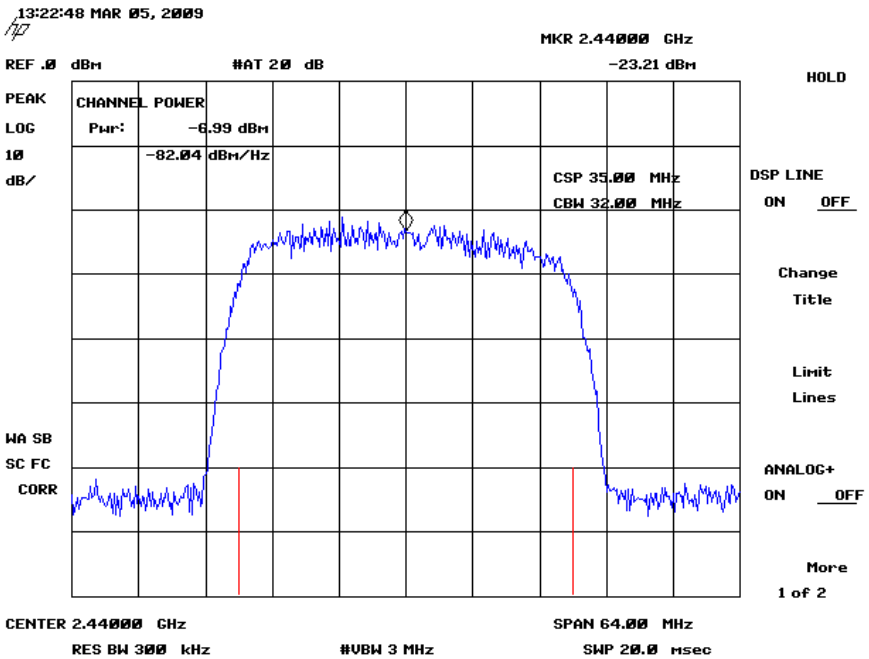

Figure 6.11. Measured channel sounding signal power with RFX2400 daughter board; amplitude=2048.

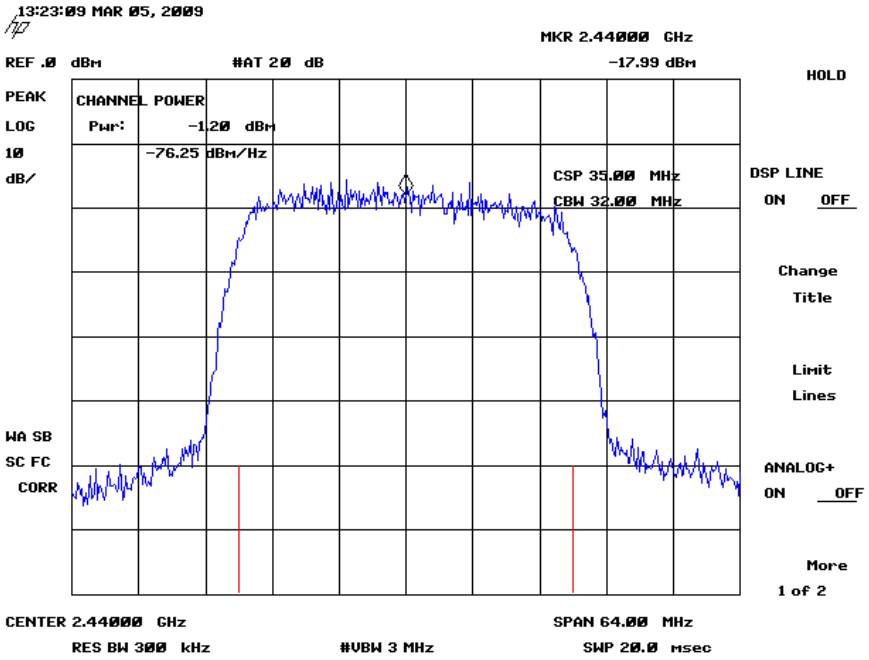

Figure 6.12. Measured channel sounding signal power with RFX2400 daughter board; amplitude=4096.

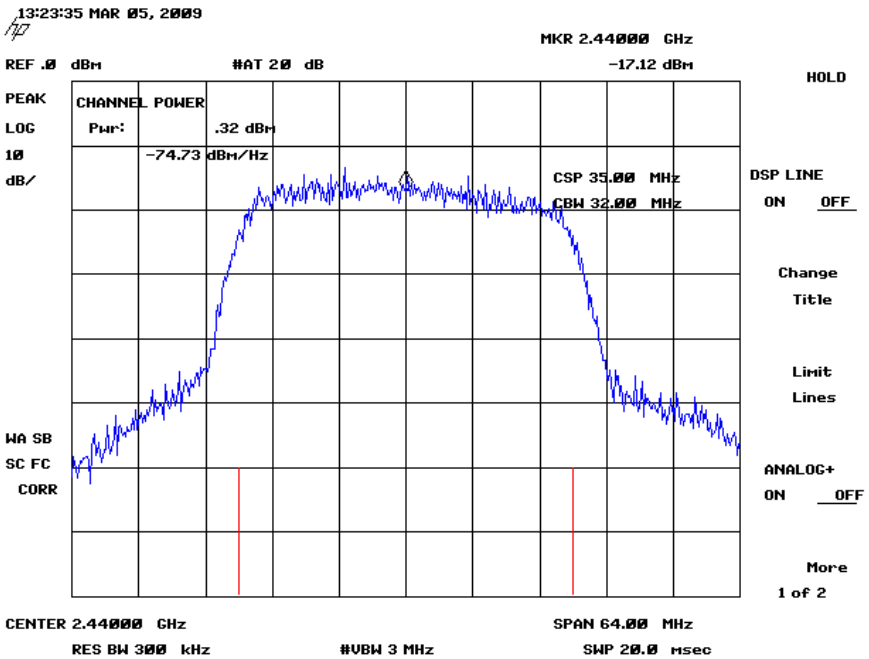

Figure 6.13. Measured channel sounding signal power with RFX2400 daughter board; amplitude=5000.

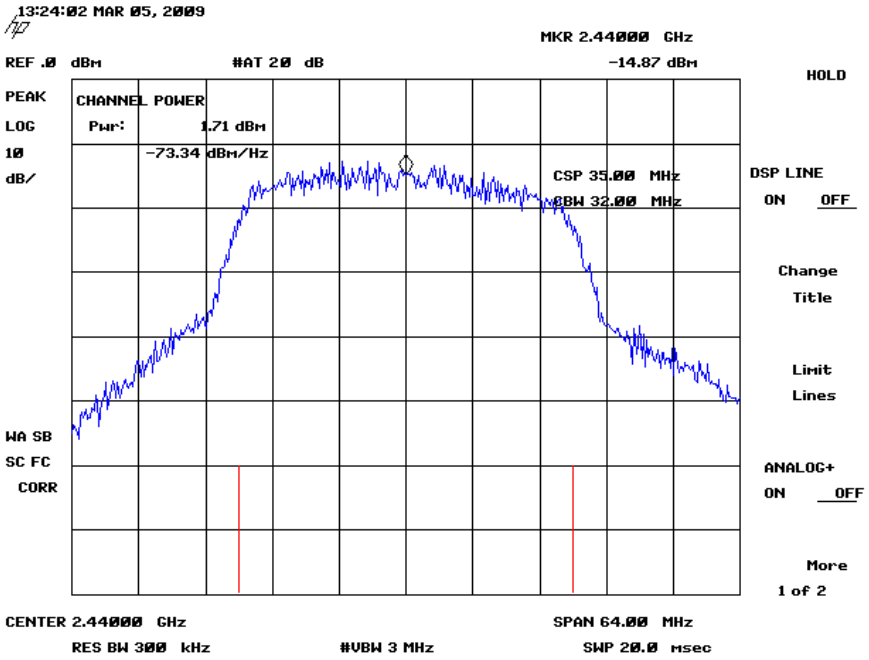

Figure 6.14. Measured channel sounding signal power with RFX2400 daughter board; amplitude=6000.

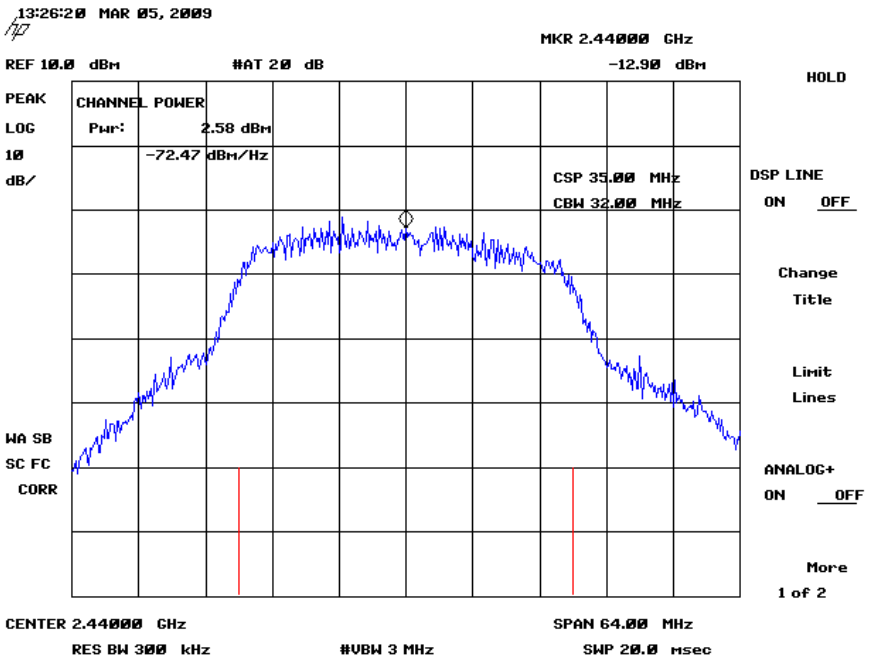

Figure 6.15. Measured channel sounding signal power with RFX2400 daughter board; amplitude=7000.

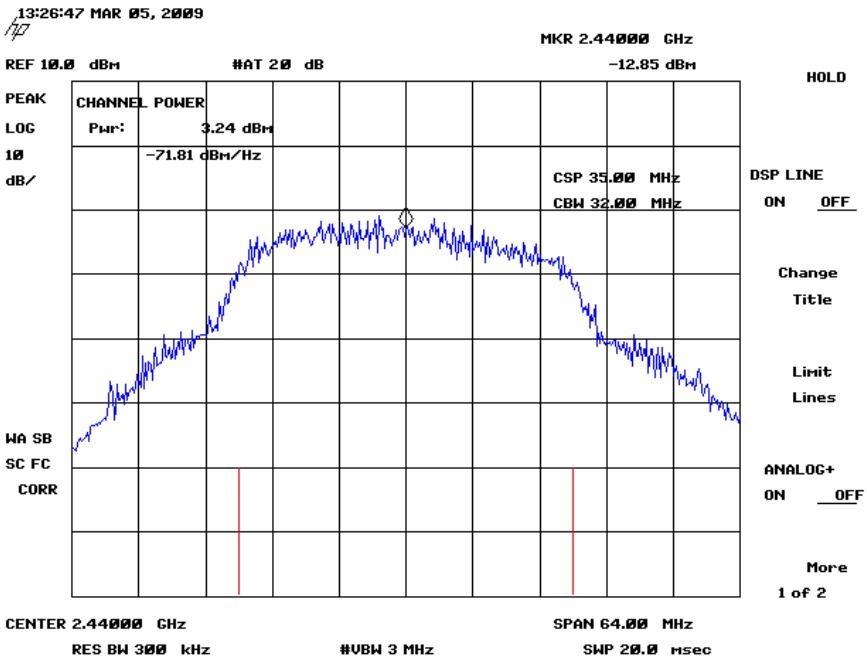

Figure 6.16. Measured channel sounding signal power with RFX2400 daughter board; amplitude=8000.

As we can see from the figures above, the signal sidelobe power level starts to increase once the DAC output power level exceeds 4096, which is half of the full DAC range. Performing channel sounding at such a power level will generate unacceptable interference to the adjacent channel. Furthermore, the noise level is also increased when boosting the signal power level. Besides interference, the power amplifier nonlinearity also comes into play when the DAC is overdriven. Figure 6.17 indicates that the channel power starts to saturate when the DAC output level exceeds 4096. Overall, we chose a DAC output power level of 4096 to avoid unintended interference to the adjacent channel, as well as nonlinearity distortion.

Figure 6.18 shows a comparison between the channel power and the DAC output level for an m-sequence length varying from 512 to 4096. The measured

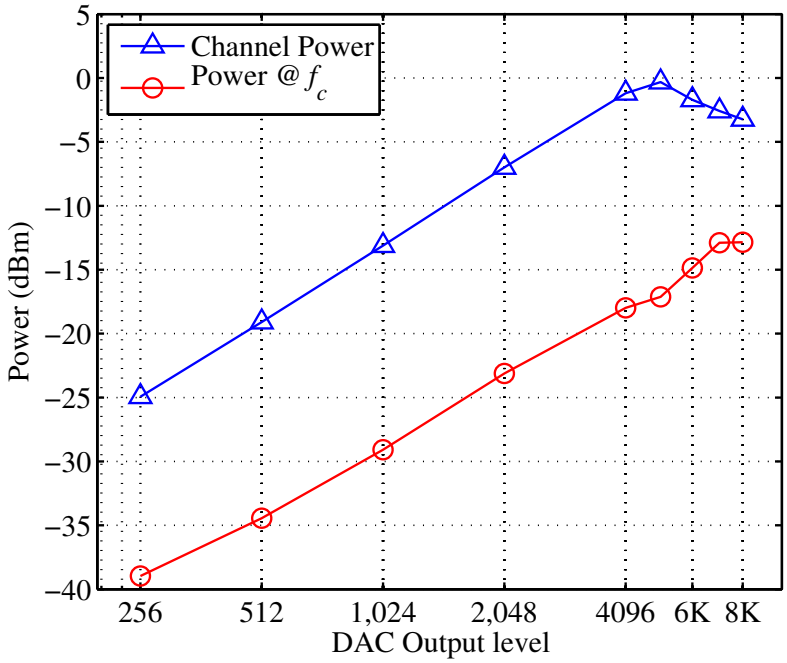

Figure 6.17. Relationship between the DAC output level and the measured output power.

channel power for different sequence lengths is relatively close. The power at center frequency behaves randomly comparing with the channel power consistency. This is because the video averaging was turned off during measurement for accuracy. It is also noticed that the actual output power for the channel sounding application does not match the theoretical maximum output power for the RFX 2400 daughter board. This can be caused by many factors, such as signal bandwidth, insertion loss, other losses on the board, RF cable loss, measurement equipment loss, etc. One example is the RF cable; the RG-58/U type cable has about 20 dB loss at frequency higher than 1 GHz. The measured channel power is -32.86 and -1.2 dBm for DAC output level of 4096 respectively with RG-58/U and minibend W-8 cable.

In order to achieve the optimal SNR, the receiver gain needs to be tuned to

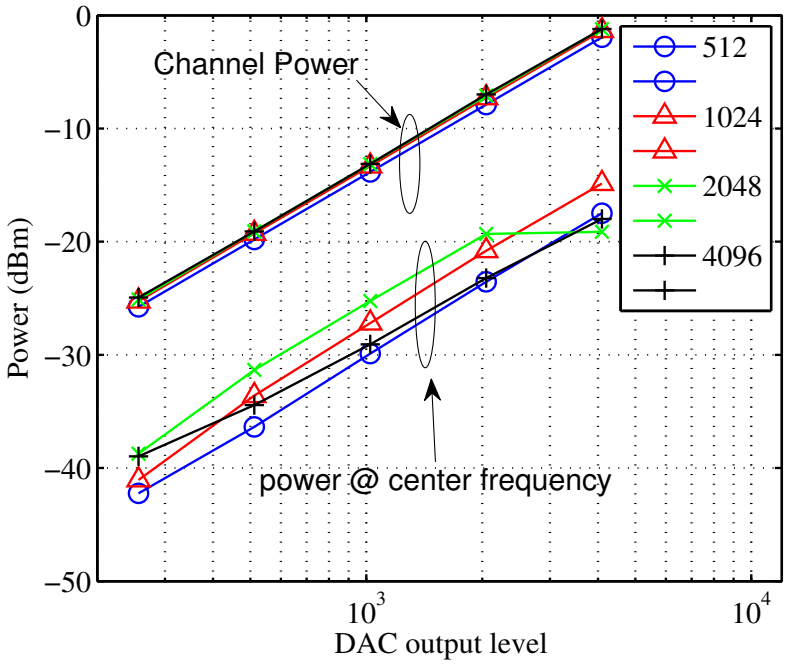

Figure 6.18. Relationship between the DAC output level and channel power; m-sequence length = {512, 1024, 2048, 4096}.

the optimal value for a certain environment. Figures 6.19 to 6.23 illustrate the maximum received channel impulse response power to noise power ratio versus the receiver gain. The channel sounding sequence length is equal to 1023 chips, and chip rate is 8 Mcps in this case. Each CIR takes approximately 0.13 second to compute, and the total number of CIR set collected is equal to 100, hence, the overall CIR calculation time is 13 seconds for each parameter set. The reason why a 1023-chip m-sequence is chosen is because longer chip sequence requires much longer calculation time. In addition, the multipath delay for indoor environment is much shorter compared with the maximum delay that a long m-sequence can offer. The *rms* delay spread for the indoor channel is on the order of nanoseconds, while the maximum delay spread a 1023-chip m-sequence can detect is on the order of microseconds for 8 Mcps.

The experiments were conducted between 10:00 AM to 12:00 PM on a business day in the hallway located on the second floor of Nichols Hall. The USRP channel sounder receiver features a tunable gain from 0 to 90 dB. Larger gain not only will boost the signal power, but also the noise power as long as the power amplifier is operated within its linear range. The blue dotted lines with circle markers in the figures represent the ratio of the maximum power and the noise power. This ratio reflects the dynamic range of the channel sounder. At small gain levels (e.g., 0 to 30), the signal is dominated by the noise, hence the ratio does not exist. For larger gain levels, the ratio first increases as the receiver gain increases, and peaks at a certain gain and the noise power becomes dominant again, hence the ratio starts to decrease. Each DAC output level represents a fraction of the full DAC output range. For the RFX 2400 daughter board, the full DAC output range is 2 volts peak-to-peak, which is 0.707 Vrms, hence, the maximum output power is 10 dBm with 50 ohm input impedance.

As we can see from the ratio graphs, a DAC output level of 6000 gives the highest maximum to noise power ratio at 60 dB receiver gain. It is important to notice that the measured signal power not only depends on the transmit power, it depends more on the channel condition where and when the measurements were taken, since the carrier frequency is within one of the IEEE 802.11b channels,[2] hence the interference from the WiFi access point and users varies over time and location. Overall, the ratio charts can be used as a configuration guideline for various parameter combinations. Figures 6.19 to 6.23 also provide a transmit power level operation guideline for the channel sounding experiment with each figure demonstrating the optimal receiver gain under unlimited transmit power

[2]The channel sounding is operated at center frequency of 2.442 GHz, which overlaps with the IEEE 802.11b channel 7 operation center frequency.

level.

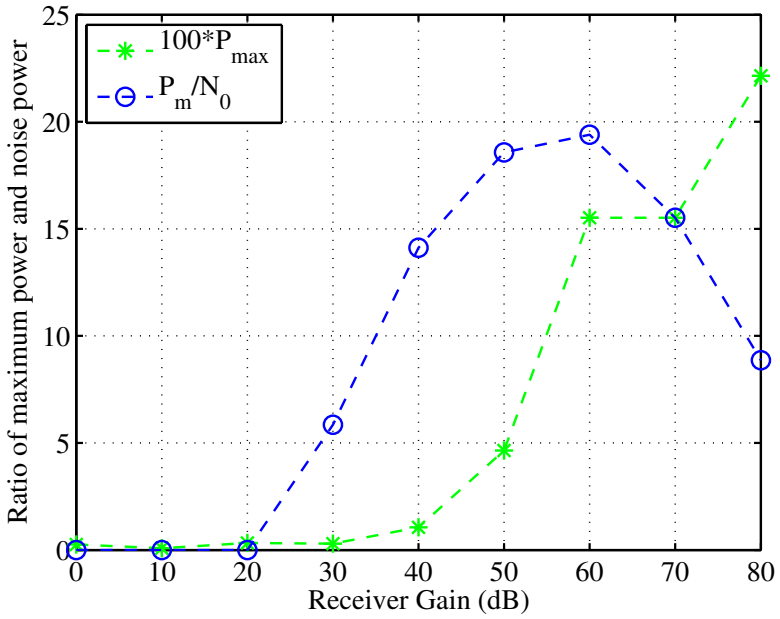

Figure 6.19. Ratio of maximum received channel impulse response power and noise power; DAC output level=6000.

6.2.2 CIR Measurement Results and Analysis

The channel impulse response measurement results discussed in this section were collected using the optimal parameters for the indoor environment, for which the output DAC level is equal to 6000, and the receiver gain is set to be 60 dB. Both line-of-sight and nonline-of-sight cases were measured at location one shown in Figure 6.7. The LOS measurements were taken at location 1 and the non-LOS measurements were taken at location 2 (see Figure 6.7). The m-sequence length is {1023, 4095} chips, chip rate is {8, 32} Mcps for both cases; the minimum delay resolution is equal to {125, 31.25} ns respectively, and the maximum detectable delay is approximately 128 μs for both sets. The total number of CIR snapshots

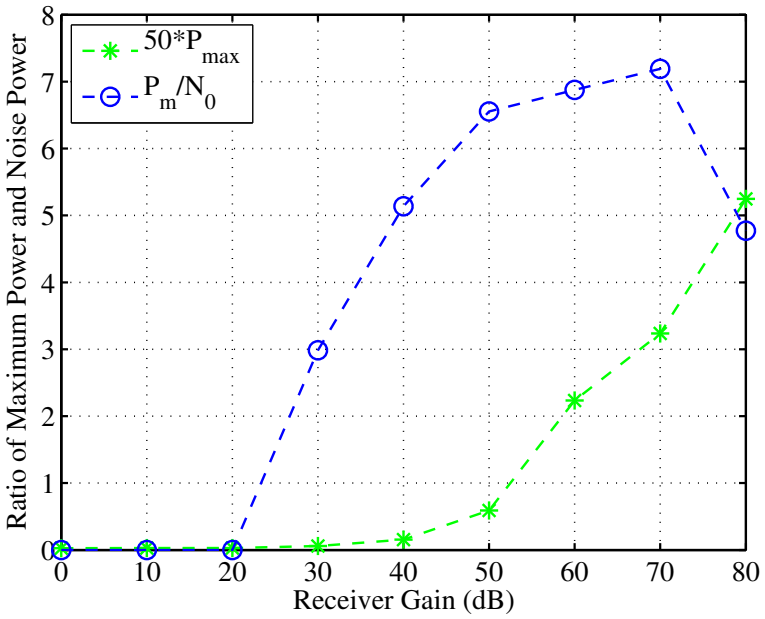

Figure 6.20. Ratio of maximum received channel impulse response power and noise power; DAC output level=8000.

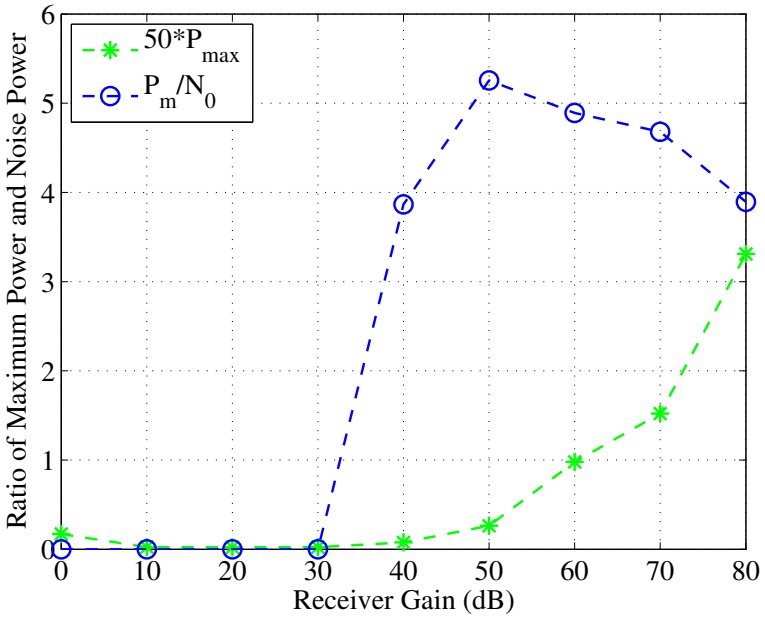

Figure 6.21. Ratio of maximum received channel impulse response power and noise power; DAC output level=10000.

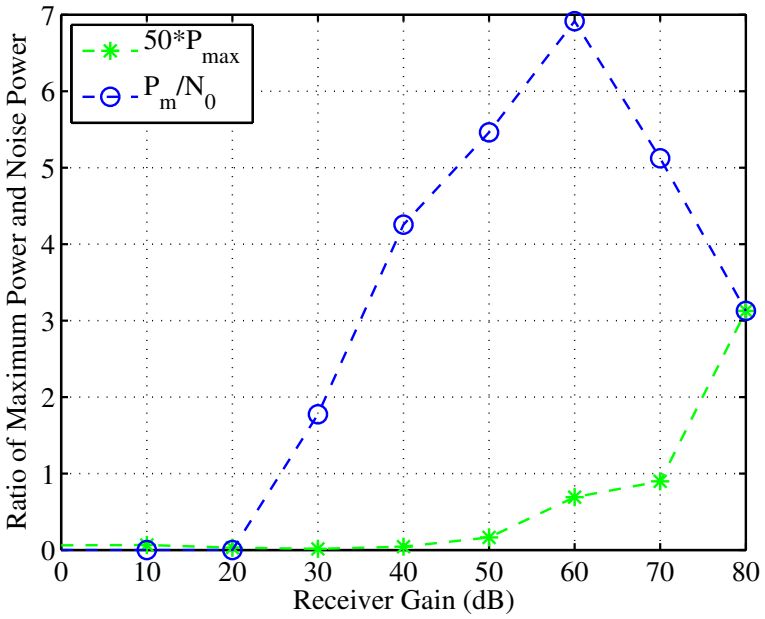

Figure 6.22. Ratio of maximum received channel impulse response power and noise power; DAC output level=20000.

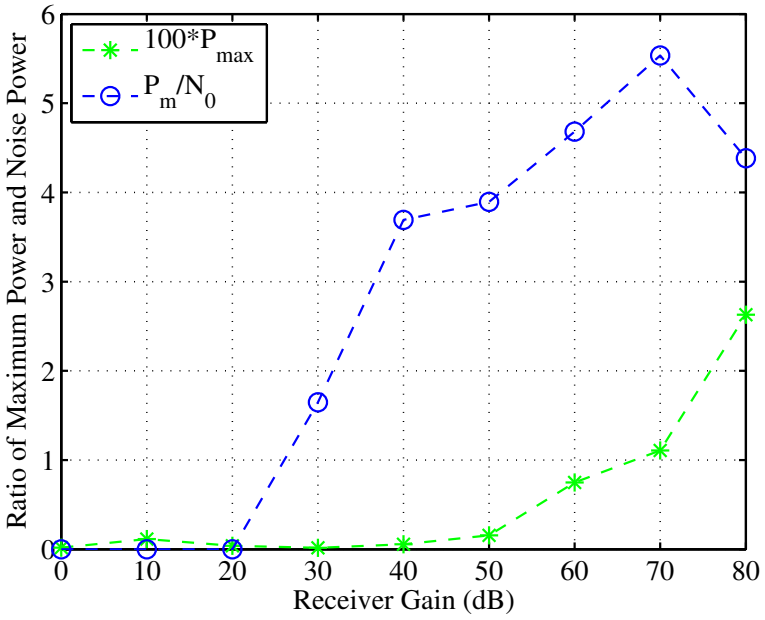

Figure 6.23. Ratio of maximum received channel impulse response power and noise power; DAC output level=30000.

collected is 100, which allows us to generate an average power delay profile across a time window width of 0.13 and 0.5 second for each sequence length. The measurements will be conducted at two different chip rates; the slower chip rate is essentially limited by the USB 2.0 throughput limitation (32 MB/s), as well as the lowpass filter. The higher chip rate version uses a custom FPGA bitstream file to bypass the USB 2.0 port when recording the channel impulse response measurement data. In addition, the received data is not filtered by the 20 MHz baseband filter, hence the maximum possible bandwidth is achieved.

6.2.2.1 Indoor Channel Measurement

Figures 6.24 and 6.25 display the measured channel impulse response for an indoor environment at two different locations. Figure 6.24 clearly shows three multipath channel components. The first path contains the most power. Notice that the power of the second multipath component is not significantly smaller than the first path. This is due to the fact that the measurement was conducted in the hallway, where the reflected signal strength is not weakened dramatically. However, if the signal is reflected multiple times before it reaches the receiver, the signal strength can be undetectable. Although only three multipath components were captured by the receiver, there might be more delay paths that fall in between two delay paths, since the minimum delay resolution of the channel sounder is only 62.5 ns. As discussed previously, the delay for an indoor channel can be as small as several nano seconds, which requires a channel sounder operating at 100 Mcps or higher.

Figure 6.25 illustrates a channel impulse response measurement for a non-LOS scenario. For this scenario, the first path that arrives at the reciever does

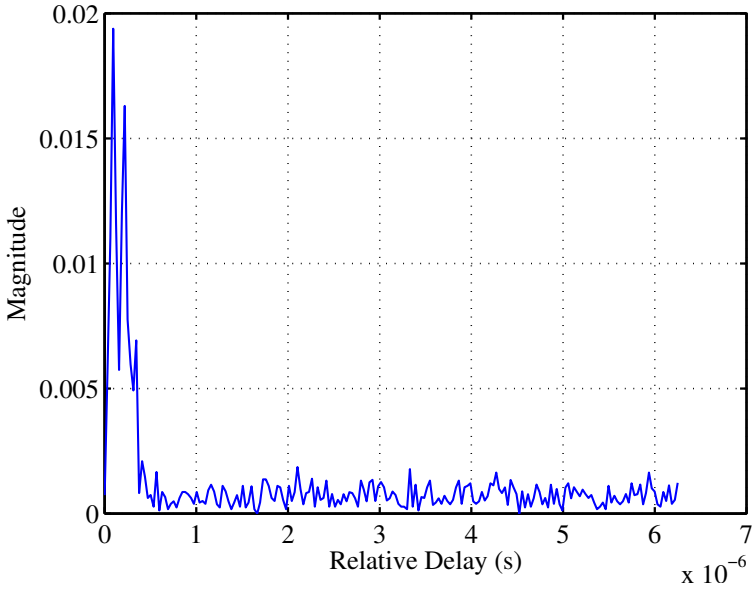

Figure 6.24. Measured channel impulse response with LOS; m-sequence length = 4095; chip rate = 32 Mcps.

not contain the strongest signal strength, because the signal is attenuated when transmitting through obstacles, such as doors, walls, etc. The delay component with the strongest signal strength usually takes a longer route where less obstacles are in the path, hence the signal strength does not suffer from attenuation as much as the first path. However, signal reflection can also cause signal strength reduction, which explains the reason why the magnitude is lower than in Figure 6.24. Moreover, the signal magnitudes shown in those two figures are instantaneous, which varies from one time instance to another. A better illustration will be the power delay profile, which shows the average channel impulse response over a period of measurement time.

Figures 6.26 and 6.27 demonstrate the power delay profile measurements for the same indoor channel as Figures 6.24 and 6.25. The power delay profile is obtained by averaging 100 CIR snapshots, which is approximately over a time

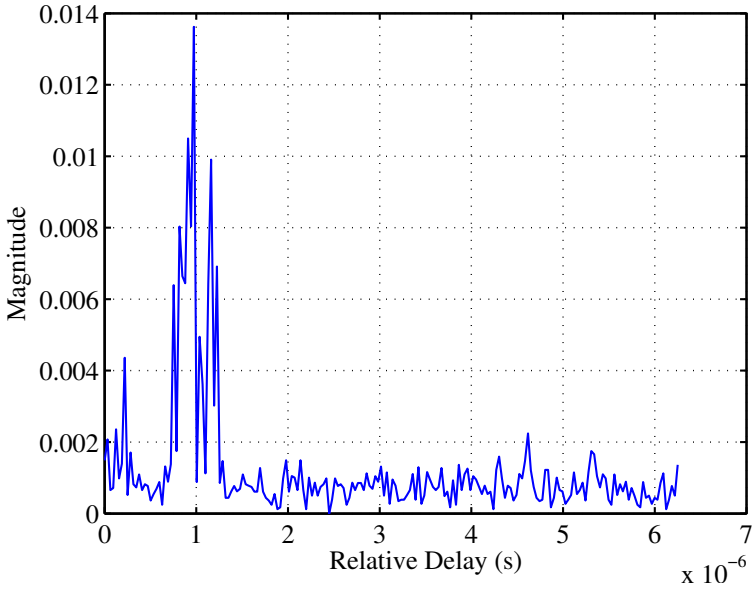

Figure 6.25. Measured channel impulse response without LOS; m-sequence length = 4095; chip rate = 32 Mcps.

window of 50 seconds. As we can see from Figure 6.26, the power delay profile reflects a similar multipath component distribution. The strong path arrives with shorter delay, and the signal strength decreases as the delay increases. Comparing Figures 6.26 and 6.24, the first clear multipath appears in the power delay profile figure has a short delay associated with it. This is the result from averaging over a relatively long period of time. In addition to the averaging process, signal fluctuation at a certain delay also causes a minor time shift. In Figure 6.27, the power delay profile almost looks like a triangle followed by a small chunk of signal. As explained previously, for the non-LOS case, the first arriving signal may not contain the strongest signal path, which is also validated in the power delay profile graph. The path with the strongest signal strength is located roughly at 1 μs, which is consistent with Figure 6.25. It is also noticed that the average signal magnitude of the non-LOS case is smaller than the LOS one. Again, this is due to

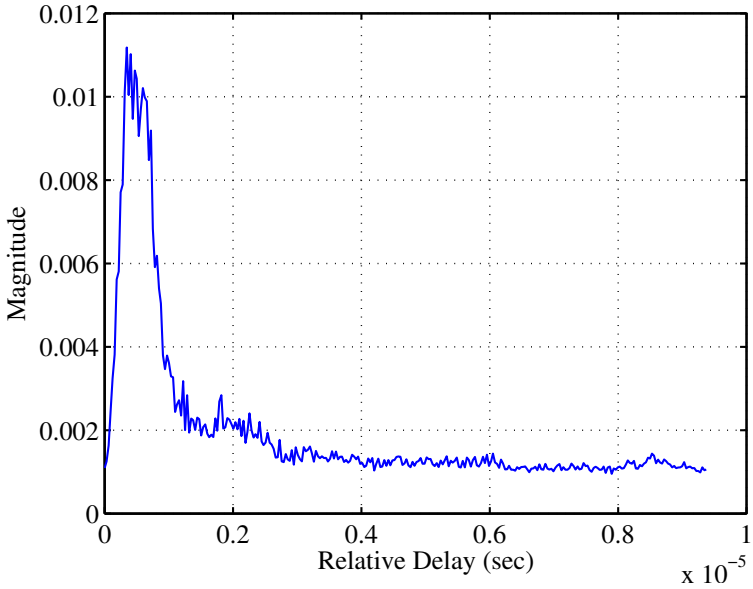

Figure 6.26. Power delay profile of the indoor channel with LOS; Number of CIR snapshots = 100.

the fact that the non-LOS signal suffers more attenuation than the LOS signal.

The dynamic range for the LOS power delay profile is approximately 15 dB, where it is 20 dB for the non-LOS case. Intuitively, the LOS signal strength should be stronger than the non-LOS signal, and hence the dynamic range is wider. However, this is true for the channel impulse response at a given time instance, see Figure 6.24 and 6.25 for example, because the power delay profile is the average of the CIRs over a period of measurement time so the dynamic range varies from one measurement to another.

Moreover, during the measurement period, the USRP underrun may happen randomly. USRP underrun happens if not enough samples are ready to send to the USRP sink, while the USB is still reading in data, which causes undesired data to be recorded. To overcome this issue, a mechanism that marks the channel sounding cycle when USRP underrun happens is implemented, and hence, the

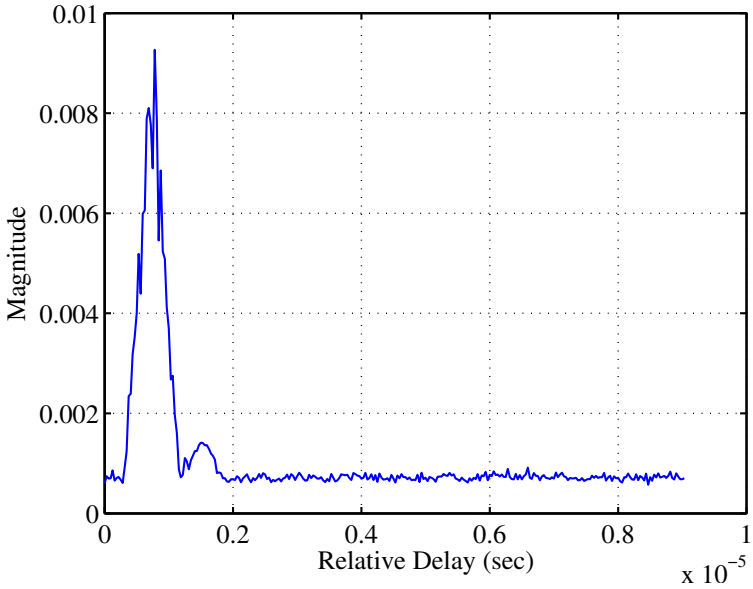

Figure 6.27. Power delay profile of the indoor channel without LOS; Number of CIR snapshots = 100.

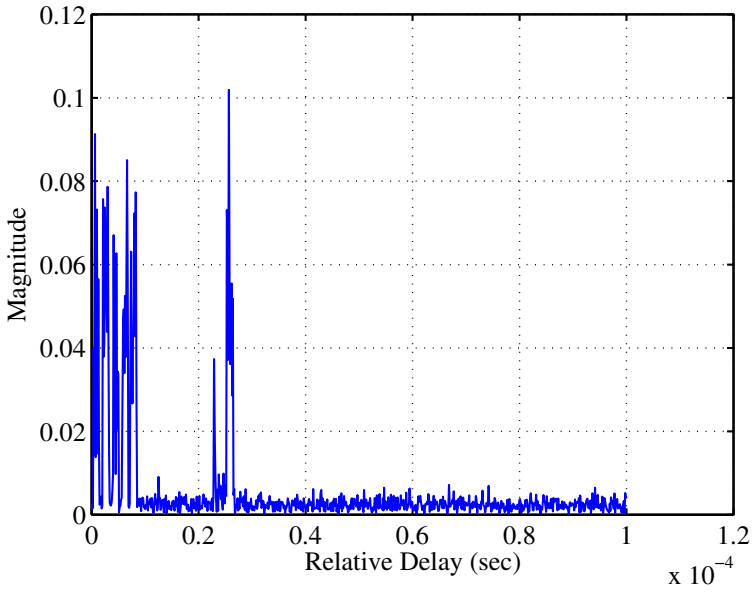

Figure 6.28. Example of the output of the correlator when USRP underrun happens.

recored data can be neglected during post processing. This issue is more noticeable for the 8 Mcps sounder, since the cross-correlation is performed by the end terminal (computer), not the FPGA. Figure 6.28 shows an example of the output of the correlator when the USRP underrun happens. It is seen from the graph that the output shows channel impulse response on the order of 10^{-4} second, which is unlikely to happen for indoor environment. After an investigation of the received signal, the output appears to be the correlation between the m-sequence and random data, which contains out-of-order m-sequences.

6.2.2.2 Timing Offset Issue

The synchronization of TX and RX is a key problem for wireless channel sounding. It is required to establish synchronization in frequency and time at a TX and RX that can be separated by distances up to several kilometers. The presence of multipath propagation makes this task even more difficult. For outdoor environments, the *Global Positioning System* (GPS) offers a way of establishing common time and frequency references [60]. However, this approach requires a direct line of sight connection to GPS satellites which is rarely fullfilled in microcellular scenarios. For the indoor channel sounding, distances up to about 10 meters, coaxial cable can be used to synchronize the TX and the RX. For larger distances, fiber-optic cables are preferable.

As mentioned previously, time synchronization is not implemented for the USRP, which will not only result in a time shift in the recorded channel impulse response, but also a timing offset between the TX and RX local clock. Minor timing offset will not affect the entire record of the CIR, however, high timing offset will. The sounder works by transmitting a PN sequence, then correlating

the received sequence against the original at all possible offsets. However, to do so, it collects an entire PN sequence and does the multiply and accumulate across it for each lag in the impulse response. Thus, if the PN sequence period is N chips, it takes N^2 chips to calculate a single impulse response. For example, the 4095-chip sequence will take 16769025 chips to complete a single IR record. At 8 Mcps, this is approximately 2 seconds per record, and 0.5 second per record at 32 Mcps.

The crystal oscillator used by the USRP has an offset of ± 50 ppm (parts per million) between the transmitter and receiver. At 8 Mcps, during the course of 2 seconds, the receiver clock will differ from the transmit clock by:

$$2 \times 50 \times 10^{-6} \times 8^6 = 800 \text{ chips}, \tag{6.2}$$

which is equivalent to 6400 clocks. At 32 Mcps, the timing offset between the TX and RX is the same as 8 Mcps. Hence, the next peak in the correlation will arrive 800 chips earlier at 50 ppm, which results in a compressed correlation bin. To prove the effect of timing offset between TX and RX, Fgure 6.29 shows a record of the channel impulse resopnse with compressed correlation bin size.

Figure 6.29(a) is generated by using a 4095-chip PN sequence, the correlation peak separation should be 4095 chips with perfect timing synchronization. However, due to timing offset, the correlation peak offset becomes 800 chips. Both Figures 6.29(a) and 6.29(b) show a compressed correlation bin size of 800 chips. For both cases, the correlation bin size is compressed to 800 chips, so the frequency offset of the crystal oscillator is 50 ppm.

Based on the analysis, the sounder will not work for a PN sequence length

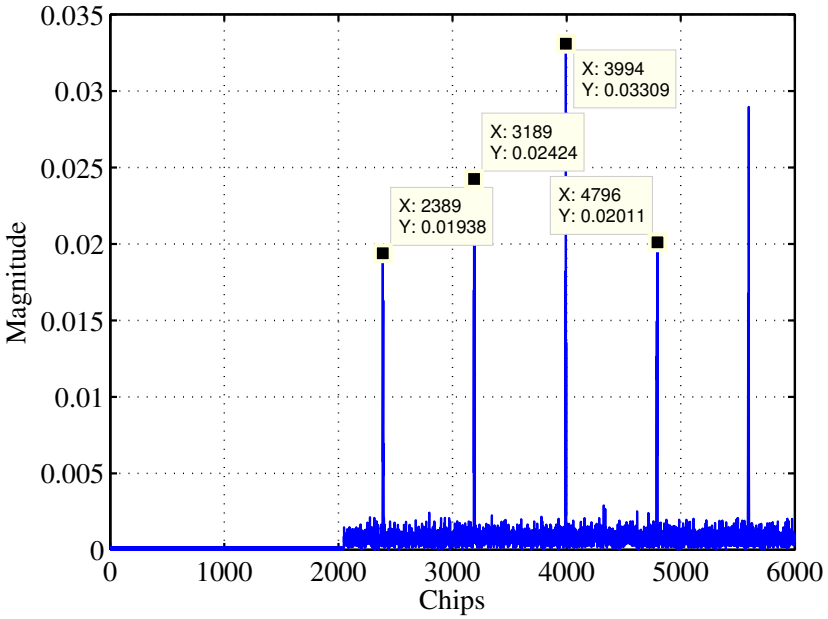

(a) 32 Mcps timing offset.

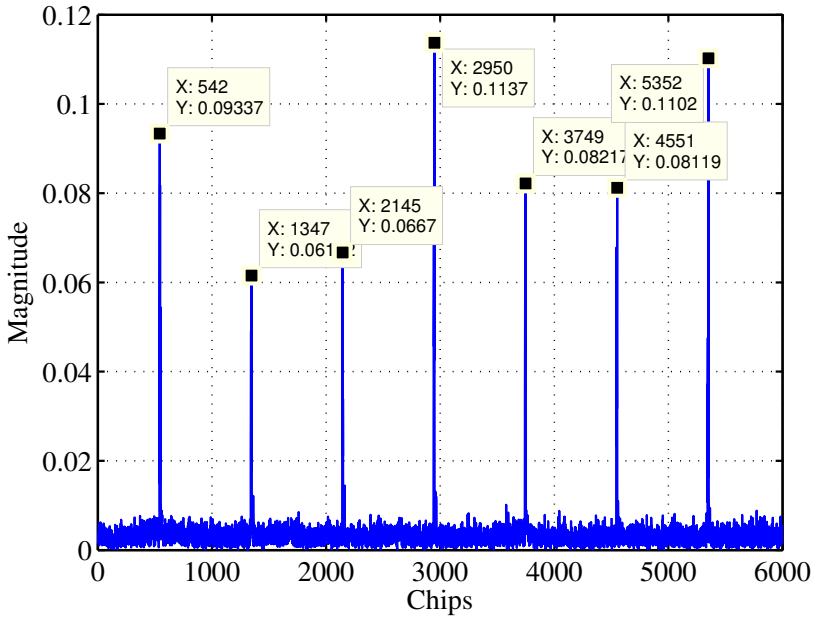

(b) 8 Mcps timing offset.

Figure 6.29. Compressed correlation bin size for 8 and 32 Mcps; PN sequence length is 4095 and 1023 chips for 32 and 8 Mcps respectively.

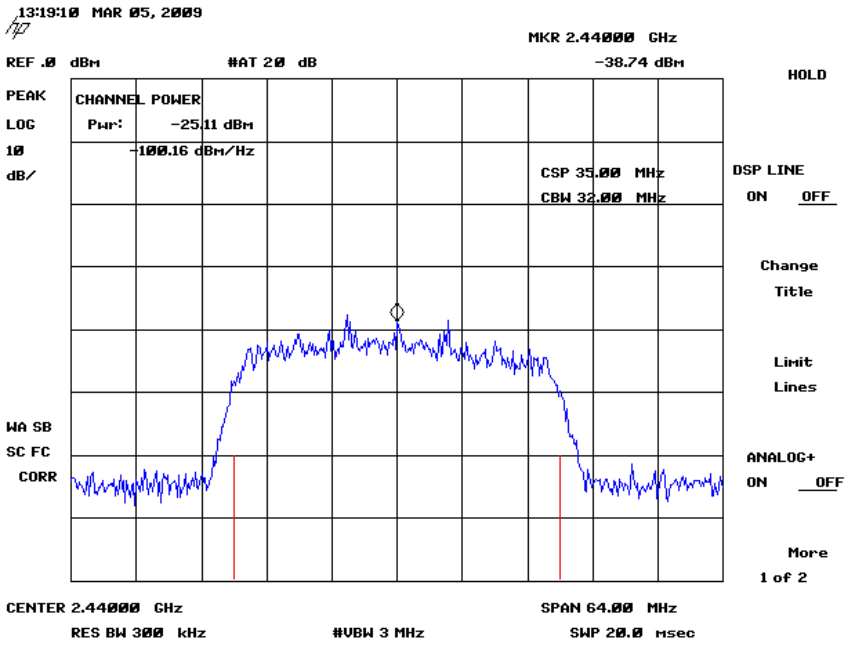

Figure 6.30. Sounding signal spectrum; Amplitude = 256; sequence length = 2047.

less than 1023 chips, since the next usable sequence length is $2^9 - 1 = 511$ chips. However, the channel impulse response records for PN sequence degree greater than 10 still represent the actual channel impulse response with the same time period according to the sequence length.

Figures 6.30 through 6.39 show the signal power spectrum and channel power for each case. Depending on the maximum transmit power limit and interference restriction, one can choose the appropriate parameter combination to perform channel sounding.

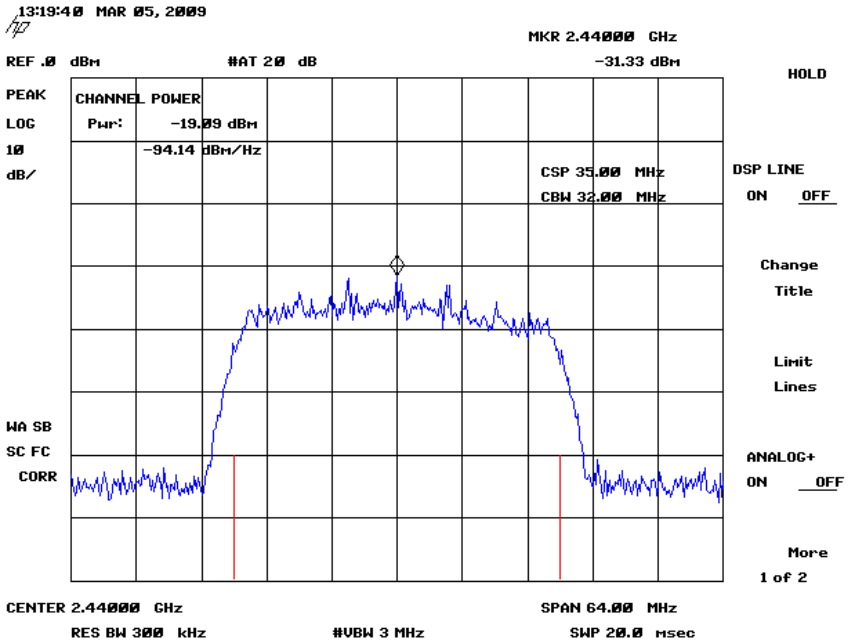

Figure 6.31. Sounding signal spectrum; Amplitude = 512; sequence length = 2047.

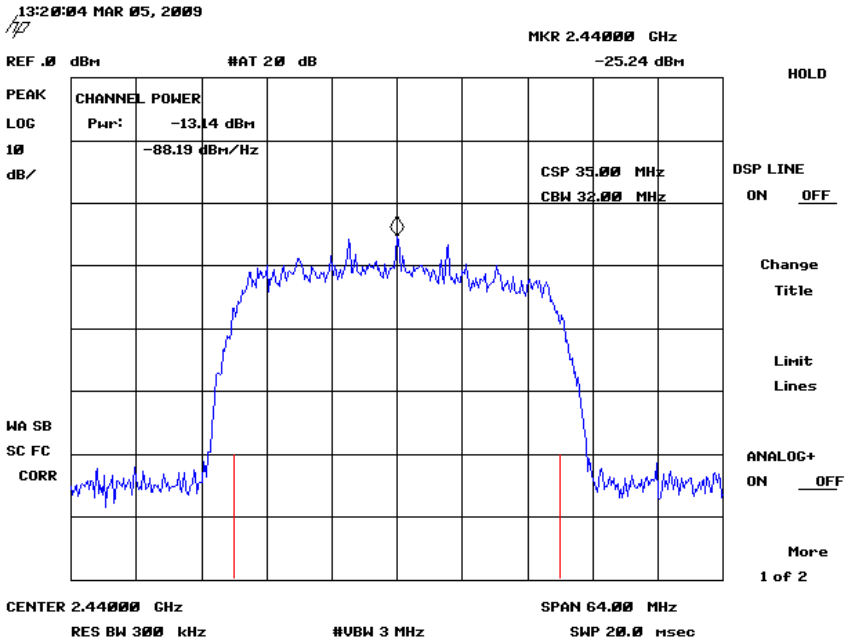

Figure 6.32. Sounding signal spectrum; Amplitude = 1024; sequence length = 2047.

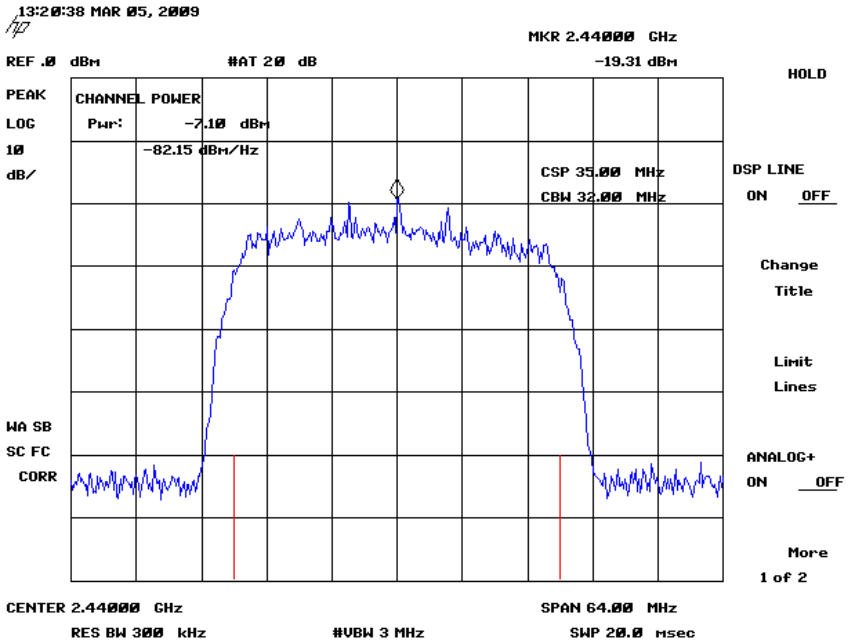

Figure 6.33. Sounding signal spectrum; Amplitude = 2048; sequence length = 2047.

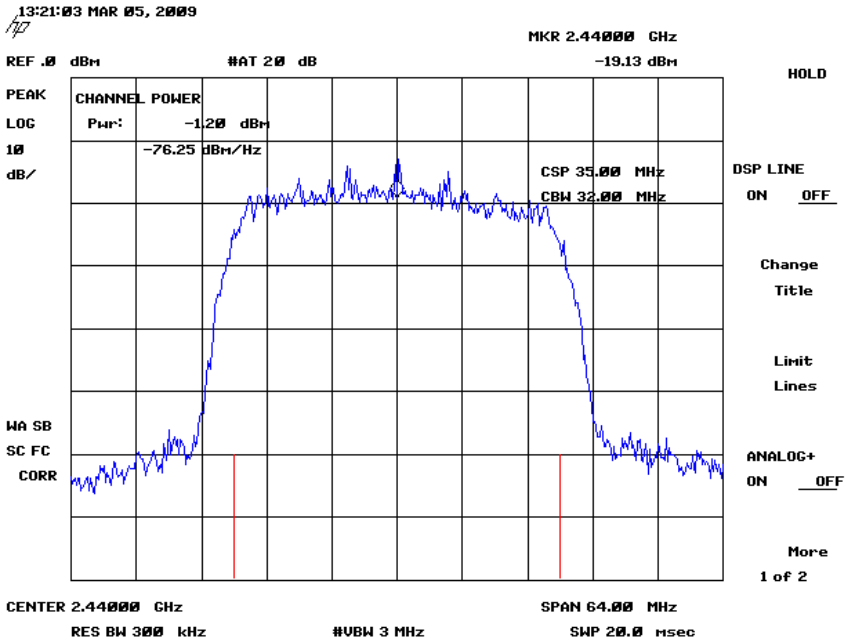

Figure 6.34. Sounding signal spectrum; Amplitude = 4096; sequence length = 2047.

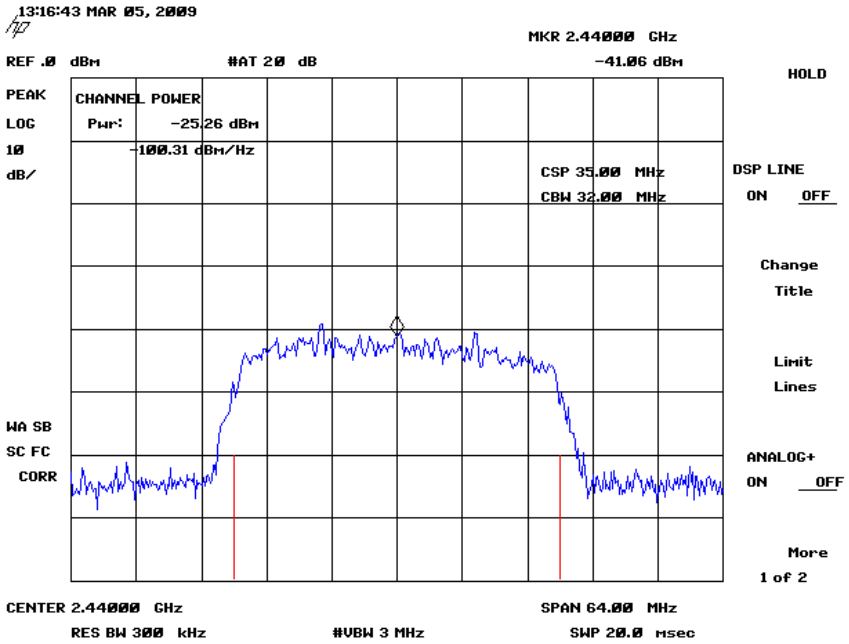

Figure 6.35. Sounding signal spectrum; Amplitude = 256; sequence length = 1023.

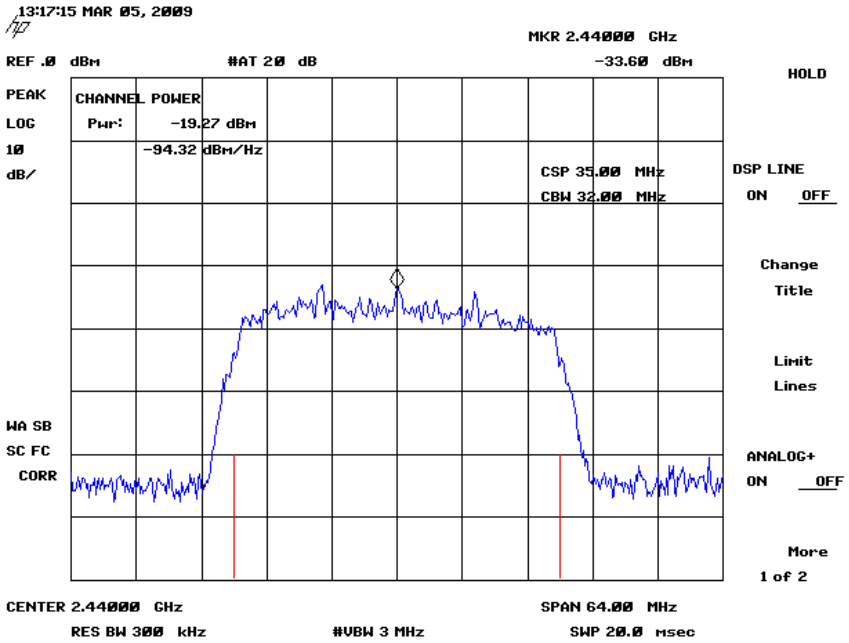

Figure 6.36. Sounding signal spectrum; Amplitude = 512; sequence length = 1023.

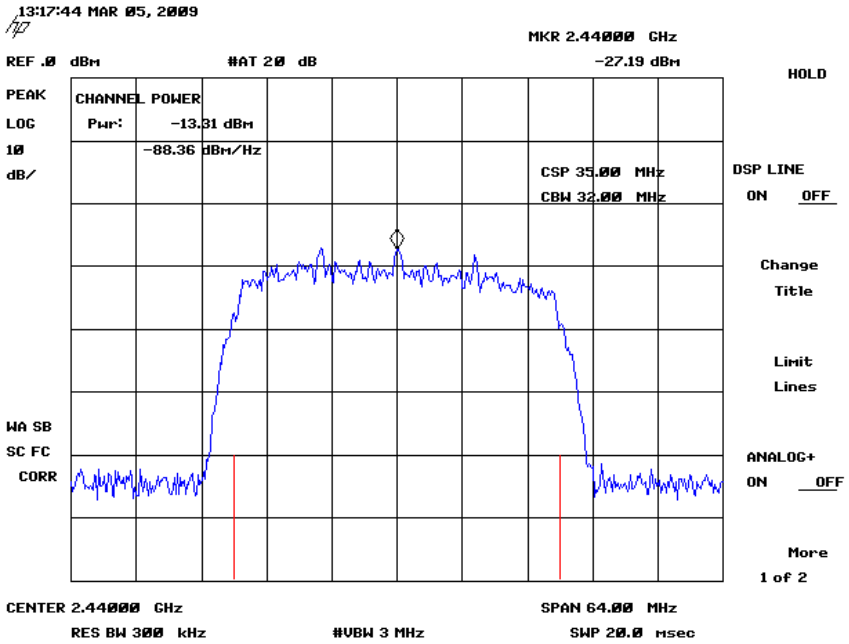

Figure 6.37. Sounding signal spectrum; Amplitude = 1024; sequence length = 1023.

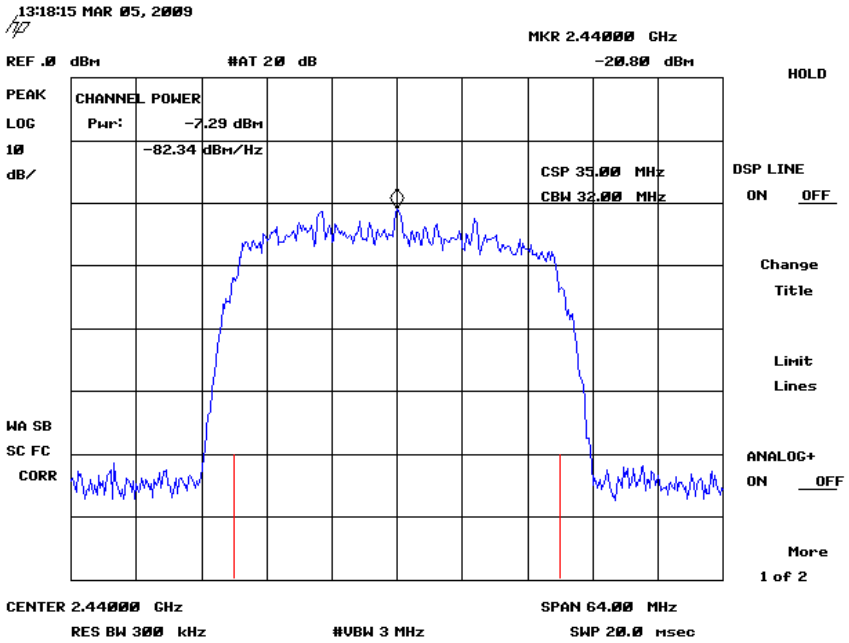

Figure 6.38. Sounding signal spectrum; Amplitude = 2048; sequence length = 1023.

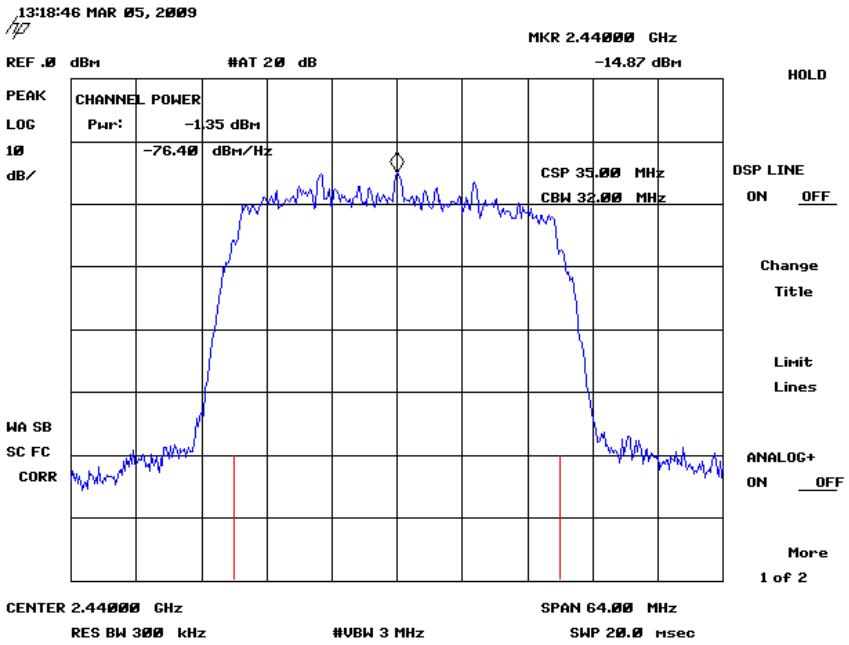

Figure 6.39. Sounding signal spectrum; Amplitude = 4096; sequence length = 1023.

6.2.2.3 Interference Measurement

Interference introduced by the sounding signal is a critical criteria when operating in a DSA network environment. In this dissertation, since the channel sounding measurement center frequency overlaps with the WiFi band, it is important to analyze the interference introduced to the WiFi user when performing channel sounding. The Received Signal Strength Indicator (RSSI) is used to evaluate the impact on the WiFi signal. The RSSI is represented in terms of percentage of the maximum received signal strength, which is -51 dBm. The full range of RSSI is between -113 to -51 dBm and it is measured versus different DAC output levels. The measurements were conducted in a laboratory; the distance separation between the USRP and a laptop is 5 meters. The WiFi signal selected has an average RSSI between 60% to 70% (-76 to -70 dBm), and the average noise

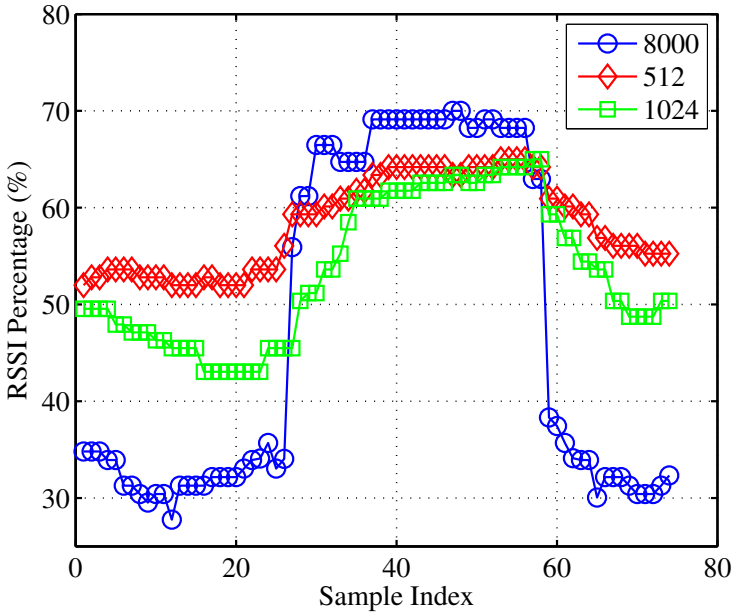

Figure 6.40. Impact on the RSSI of a WiFi signal during channel sounding measurement.

level for this location is −111.2 dBm, which is equivalent to 4% of the maximum RSSI.

Figure 6.40 shows a comparison between the impact on the RSSI for a DAC output level of 512, 1024, and 8000. The X-axis denotes the RSSI measurement sample index, where, theY-axis is the RSSI in percentage. The RSSI is measured during a period in which the channel sounder is turned on and off and turned on again. As we can observe from the figure, when the channel sounder is transmitting at the highest power (refer to Figure 6.16), the the RSSI increases about 40% from interference to interference-free.[3] For lower sounding signal power levels, the RSSI drop is approximately 12% and 15% for DAC output levels of 512 and 1024, respectively.

[3]We only consider interference from the sounding signal. Other interference sources are not discussed here.

Figure 6.41 demonstrates the impact on the RSSI for USRP DAC output power level of {1024, 2048, 4096}. The DAC output level of 4096 almost has the same impact on the WiFi signal as output level of 8000 does. This is due to the fact that the USRP output signal starts to saturate once the DAC output level exceeds 4096. This observation indicates that performing channel sounding by transmitting at the highest transmit power level without signal distortion will introduce significant amount of interference to the user within the same frequency band.

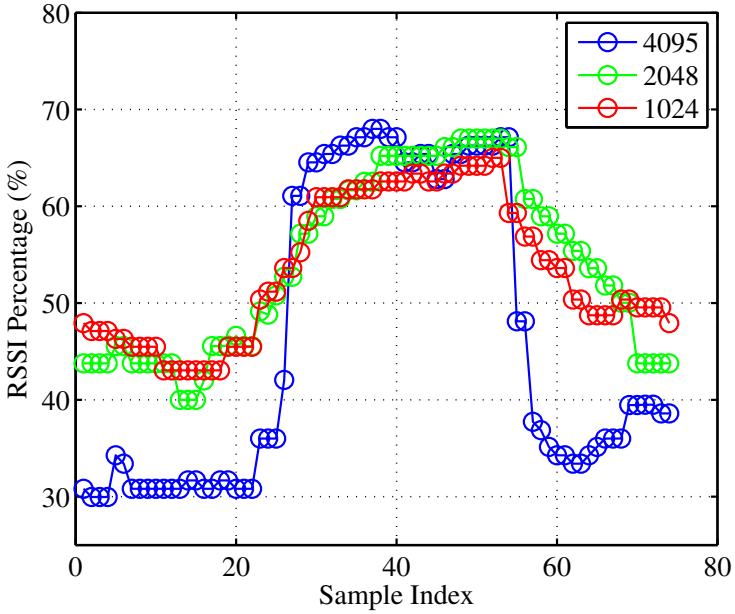

Figure 6.41. Impact on the RSSI of a WiFi signal during channel sounding measurement; DAC output level = {1024, 2048, 4096}.

Figure 6.42 reveals the relationship between the RSSI drop and the USRP DAC output level. DAC output level less than 2048 yields RSSI drop within 20%, where values greater than 2048 will result in a RSSI drop higher than 30%.

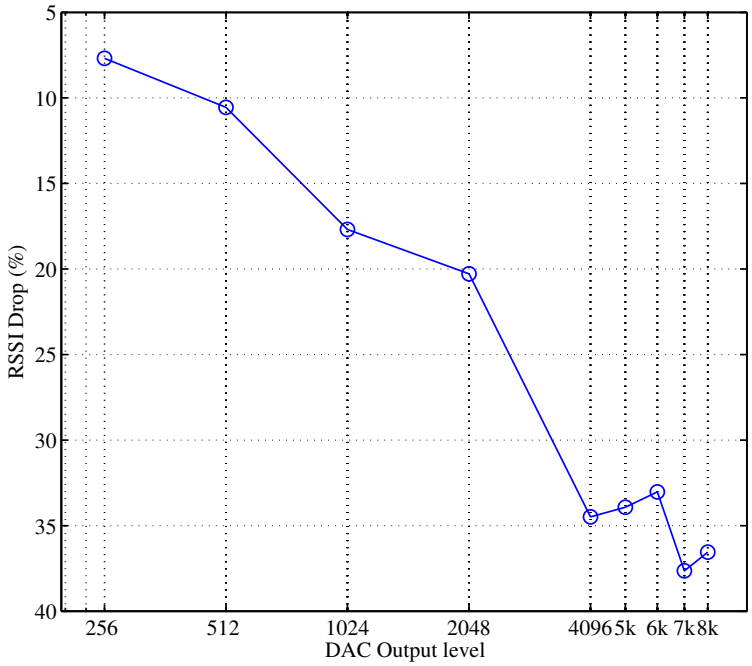

Figure 6.42. RSSI drop vs. USRP DAC output level.

6.3 Discussion on Outdoor Measurements

Ideally, the USRP channel sounder should also be able to perform measurement in an outdoor environment. However, the receiver failed to detect the transmitted signal. The measurements were conducted outside of Nichols Hall. The transmitter is located in front of the front door of the building, and the receiver is placed approximately 70 meters from the transmitter. System parameters are identical to the indoor measurement. The receiver failed to perform baseband operation, rather, the only signal observed was the carrier. This could be caused by the insufficient transmit power as well as the free space loss factor increase. It is known that the free space loss factor changes from 2 to 4 when the environment changes from indoor to outdoor [45]. Furthermore, for the indoor measurement,

the propagation channel can be considered as a tunnel, where the reflected signals are bounded within the tunnel. For outdoor environment, since onmi-directional antenna is used, the signal is emitted in all directions, which can cause weak signal strength at the receiver.

Based on the analysis, some suggestions can be made for ourdoor measurements.

- Directional Antenna: Directional antennas can limit the radiation to a narrow angle so that the signal strength is enhanced. As mentioned previously, for indoor channels, the signal is traversing through a relatively narrow space comparing with outdoor channels. The signal might be reflected multiple times before it is received by the receiver. The outcome is a channel impulse response with a large number of multipath components compacted together.

- Carrier Synchronization: Carrier Synchronization plays a more important role in outdoor channels because of greater Doppler shift. Large transmitter and receiver carrier frequency offset can result in signal reception failure. It is more severe for the sliding correlator based channel sounding, because the receiver is very likely to correlate with an undesired signal.

- Gain: In general, for an outdoor radio channel, signal distortion is more severe than for an indoor channel. This is because the objects in the channel are more scattered, and hence the signal attenuation and phase rotation are worse than for an indoor channel.

6.4 Chapter Summary

In this chapter, the implementation of the swept-time delay cross correlation channel sounder is presented. The STDCC channel sounder is implemented based on the USRP hardware platform with maximum bandwidth of 32 MHz, and an m-sequence length of 4095 chips. To achieve the maximum available bandwidth, a custom FPGA bitstream file is used in order to bypass the USB port bandwidth limitation. The GNU radio software is used to build the transmitter and receiver as well as the signal processing function blocks. Indoor channel sounding measurements were conducted inside Nichols Hall. Both line-of-sight and nonline-of-sight scenarios were studied, and measurement results were analyzed. Interference measurements were also conducted by measuring the RSSI drop of a nearby WiFi signal. The measurements show that the channel sounder will introduce significant amount interference when transmitting at half of the maximum power. However, this issue can be solved if the MC-DS-STDCC sounder is used. The experiment is not intended to be used to study the indoor wireless channel behavior because of it's lack of bandwidth. It is rather a preliminary implementation and measurement for later research. Unlike most commercial products, the GNU radio and USRP are still in the research stage, and many software and hardware issues are to be discovered by researchers.

Chapter 7

Conclusion

7.1 Research Achievements

Channel sounding plays a critical role in wireless system design. It provides the designer knowledge of the radio channel in assisting system design in many degrees. It also provides a route to study the characteristics of the radio channel, which can be used in simulation and channel modeling. In this dissertation, the challenges of designing a channel sounding technique for the dynamic spectrum access network are presented. Due to the randomness of spectral and temporal access of the DSA network, performing channel sounding consistently without interfering with other users becomes the major design concern.

The major contributions of this dissertations are summarized as following:

- Characterized the user access randomness in both frequency and time domain. Explicitly, unlicensed users access the channel, depending more on the channel availability and interference tolerance level compared to the licensed users. The licensed users can access the channel without realizing the existence of the unlicensed users. Addressed challenges in designing the

channel sounding system for the DSA network environment. Tasks needing to be solved are how to perform channel sounding without interfering with other users; how to perform channel sounding efficiently when frequent frequency and time switching is required.

- A multicarrier direct sequence spreading based channel sounding system framework combining with the STDCC channel sounder, also termed as MC-DS-STDCC is presented. The MC-DS-STDCC utilizes direct sequence spreading to minimize the interference to other users within the same frequency band, and multicarrier modulation to achieve frequency agility. To be more specific, each subcarrier is able to adjust the transmit power by increasing or decreasing the spreading sequence length in order to satisfy the power limit. Moreover, the use of spread spectrum also increases the inherent processing gain of the system, and hence, the dynamic range of the channel sounder is enlarged.

- In contrast to the MC-DS-STDCC channel sounding technique, the OFDM-based channel sounding technique is focusing on reducing the system complexity, mainly sampling rate. The OFDM-based channel sounder uses has the ability to use the user data as the sounding signal, which eliminates the sounding signal generator, and hence the system complexity is reduced. However, the performance is directly related to the autocorrelation of the user transmit data, that is, the optimal sounding signal is achieved when the data across all subcarriers is equal to one. A tradeoff study is conducted in interpolating the performance loss versus the randomness of the user data. On the other hand, since the OFDM-based channel sounding technique uses

user data as the sounding signal, no extra interference will be introduced as long as the user has permission to the frequency band. However, the system performance is traded off for the system complexity.

- Channel sounder is a measurement device, and hence, it is only useful if implemented. In this dissertation, the implementation of the STDCC is presented based on the USRP and GNU radio. The implementation of the MC-DS-STDCC and OFDM-based channel sounder is out of the scope of this dissertation because of the hardware and software limitation. The USRP platform supports maximum bandwidth of 32 MHz by adopting a custom FPGA bitstream file to bypass the bandpass filter built-in on the daughter board. This bandwidth limitation is the major obstacle of implementing the MC-DS-STDCC channel sounder, which requires a much higher bandwidth in order to perform spread spectrum. Indoor experiments were conducted inside Nichols Hall in Lawrence, KS. The experiment results were studied and analyzed.

7.2 Future Work

There exists a number of topics that have resulted from this research that are worth continuing:

- Towards the end of this research, the second version of the USRP became available, which supports much higher baseband bandwidth and eliminates the USB bottleneck completely by replacing it with a gigabyte Ethernet interface. This improvement makes the implementation of the MC-DS-STDCC and OFDM-based channel sounder become feasible. It would be

interesting to implement both proposed systems on the USRP 2.

- The channel sounding measurements taken were for the static channel environment, for most of the modern wireless communication system, the transmitter and receiver are nonstatic, which means the study of the Doppler shift is essential. Again, the USRP 2 allows us to upload the GNU radio software onto the board, which makes the entire unit stand alone. This makes the study of the Doppler shift doable.

- Due to the randomness of the DSA network, predicting the channel behavior becomes difficult. A long term statistical analysis of the channel behavior would be invaluable for both channel modeling and system design. This work requires the development of a signal processing algorithm to process the collected data.

References

[1] J. Mitola, "Software radio architecture: a mathematical perspective," *Selected Areas in Communications, IEEE Journal on*, vol. 17, no. 4, pp. 514–538, 1999.

[2] J. Parsons, D. Demery, and A. Turkmani, "Sounding techniques for wideband mobile radio channels: a review," in *Communications, Speech and Vision, IEE Proceedings I*, vol. 138, October 1991, pp. 437–446.

[3] D. Cox and R. Leck, "Correlation bandwidth and delay spread multipath propagation statistics for 910-MHz urban mobile radio channels," *Communications, IEEE Transactions on*, vol. 23, no. 11, pp. 1271 – 1280, Jan 1975.

[4] D. Cox, "Delay doppler characteristics of multipath propagation at 910 MHz in a suburban mobile radio environment," *Antennas and Propagation, IEEE Transactions on*, vol. 20, no. 5, pp. 625 – 635, Jan 1972.

[5] D. Cox and R. Leck, "Distributions of multipath delay spread and average excess delay for 910-MHz urban mobile radio paths," *Antennas and Propagation, IEEE Transactions on*, vol. 23, no. 2, pp. 206 – 213, Jan 1975.

[6] D. Cox, "A measured delay-doppler scattering function for multipath propagation at 910 MHz in an urban mobile radio environment," *Proceedings of the IEEE*, vol. 61, no. 4, pp. 479– 480, 1973.

[7] "FCC statement of the chairman." [Online]. Available: http://www.fcc.gov/Daily_Releases/Daily_Business/2008/db1117/FCC-08-260A2.txt

[8] "DARPA XG Program web site." [Online]. Available: http://www.darpa.mil/ato/programs/XG/

[9] "OverDRiVE web site." [Online]. Available: http://www.ist-drive.org/index2.html

[10] D. Grandblaise, D. Bourse, K. Moessner, and P. Leaves, "Dynamic Spectrum Allocation (DSA) and Reconfigurability," in *SDR Forum*, November 2002.

[11] J. Parsons, D. Demery, and A. Turkmani, "Sounding techniques for wideband mobile radio channels: a review," *Communications, Speech and Vision, IEE Proceedings I*, vol. 138, no. 5, pp. 437 – 446, Oct 1991.

[12] "Ettus Research web site." [Online]. Available: http://www.ettus.com

[13] A. Healey, C. Bianchi, and K. Sivaprasad, "Wideband outdoor channel sounding at 2.4 ghz," *Antennas and Propagation for Wireless Communications, 2000 IEEE-APS Conference on*, pp. 95 – 98, Oct 2000.

[14] J. Kivinen, T. Korhonen, P. Aikio, R. Gruber, P. Vainikainen, and S. Haggman, "Wideband radio channel measurement system at 2 ghz," *Instrumentation and Measurement, IEEE Transactions on*, vol. 48, no. 1, pp. 39 – 44, Feb 1999.

[15] S. Salous and V. Hinostroza, "Wideband indoor frequency agile channel sounder and measurements," *Microwaves, Antennas and Propagation, IEE Proceedings* -, pp. 573 – 580, Nov 2005.

[16] R. Thoma, M. Landmann, G. Sommerkorn, and A. Richter, "Multidimensional high-resolution channel sounding in mobile radio," *Instrumentation and Measurement Technology Conference, 2004. IMTC 04. Proceedings of the 21st IEEE*, vol. 1, pp. 257 – 262 Vol.1, Apr 2004.

[17] S. Charles, E. Ball, T. Whittaker, and J. Pollard, "Channel sounder for 5.5 ghz wireless channels," *Communications, IEE Proceedings-*, vol. 150, no. 4, pp. 253 – 258, Jul 2003.

[18] R. Thoma, D. Hampicke, A. Richter, and G. Sommerkorn, "Measurement and identification of mobile radio propagation channels," *Instrumentation and Measurement Technology Conference, 2001. IMTC 2001. Proceedings of the 18th IEEE*, vol. 2, pp. 1163 – 1170 vol.2, Apr 2001.

[19] T. Takeuchi and M. Tamura, "A ultra-wide band channel sounder for mobile communication systems," *Personal, Indoor and Mobile Radio Communications, 2001 12th IEEE International Symposium on*, vol. 2, pp. E–111 – E–115 vol.2, Jan 2001.

[20] S. Haese, C. Moullec, P. Coston, and K. Sayegrih, "Wideband measurements of the outdoor propagation channel using a new time domain channel sounder," *Vehicular Technology Conference, 1999. VTC 1999 - Fall. IEEE VTS 50th*, vol. 4, pp. 2248 – 2252 vol.4, Aug 1999.

[21] S. Guillouard, G. E. Zein, and J. Citerne, "Wideband propagation measurements and doppler analysis for the 60 ghz indoor channel," *Microwave Symposium Digest, 1999 IEEE MTT-S International*, vol. 4, pp. 1751 – 1754 vol.4, May 1999.

[22] S. Haese, C. Moullec, P. Coston, and K. Sayegrih, "High-resolution spread spectrum channel sounder for wireless communications systems," *Personal Wireless Communication, 1999 IEEE International Conference on*, pp. 170 – 173, Jan 1999.

[23] U. Karthaus and R. Noe, "Results of extensive 800 mb/s, 30 ghz channel sounding experiments," *Antennas and Propagation Society International Symposium, 1998. IEEE*, vol. 3, pp. 1688 – 1691 vol.3, May 1998.

[24] J. Kivinen and P. Vainikainen, "Wideband propagation measurements in corridors at 5.3 ghz," *Spread Spectrum Techniques and Applications, 1998. Proceedings., 1998 IEEE 5th International Symposium on*, vol. 2, pp. 512–516 vol.2, 1998.

[25] P. Karlsson, C. Bergljung, E. Thomsen, and H. Borjeson, "Wideband measurement and analysis of penetration loss in the 5 ghz band," *Vehicular Technology Conference, 1999. VTC 1999 - Fall. IEEE VTS 50th*, vol. 4, pp. 2323–2328 vol.4, 1999.

[26] J. Andersen, T. Rappaport, and S. Yoshida, "Propagation measurements and models for wireless communications channels," *Communications Magazine, IEEE*, vol. 33, no. 1, pp. 42–49, 1995.

[27] J. Medbo, H. Hallenberg, and J.-E. Berg, "Propagation characteristics at 5 ghz in typical radio-lan scenarios," *Vehicular Technology Conference, 1999 IEEE 49th*, vol. 1, pp. 185–189 vol.1, 1999.

[28] T. Rappaport, S. Seidel, and R. Singh, "900 mhz multipath propagation measurements for us digital cellular radiotelephone," *Global Telecommunications Conference, 1989, and Exhibition. 'Communications Technology for the 1990s and Beyond'. GLOBECOM '89., IEEE*, pp. 84–89 vol.1, 1989.

[29] M. Madkour, S. Gupta, and Y. Wang, "Successive interference cancellation algorithms for downlink w-cdma communications," *Wireless Communications, IEEE Transactions on*, vol. 1, no. 1, pp. 169 – 177, Jan 2002.

[30] T. Rondeau, C. Rieser, T. Gallagher, and C. Bostian, "Online modeling of wireless channels with hidden markov models and channel impulse responses for cognitive radios," *Microwave Symposium Digest, 2004 IEEE MTT-S International*, vol. 2, pp. 739 – 742 Vol.2, May 2004.

[31] A. Marousis, P. Karamalis, A. Kanatas, and P. Constantinou, "Design and simulation of a vector channel sounder for umts," *Vehicular Technology Conference, 2001. VTC 2001 Spring. IEEE VTS 53rd*, vol. 1, pp. 382 – 386 vol.1, Apr 2001.

[32] G. German, Q. Spencer, L. Swindlehurst, and R. Valenzuela, "Wireless indoor channel modeling: statistical agreement of ray tracing simulations and channel sounding measurements," *Acoustics, Speech, and Signal Processing, 2001. Proceedings. (ICASSP '01). 2001 IEEE International Conference on*, vol. 4, pp. 2501 – 2504 vol.4, Apr 2001.

[33] R. Vaughan and N. Scott, "Super-resolution of pulsed multipath channels for delay spread characterization," *Communications, IEEE Transactions on*, vol. 47, no. 3, pp. 343 – 347, Mar 1999.

[34] S. Mangold, M. Lott, D. Evans, and R. Fifield, "Indoor radio channel modeling-bridging from propagation details to simulation," *Personal, Indoor and Mobile Radio Communications, 1998. The Ninth IEEE International Symposium on*, vol. 2, pp. 625 – 629 vol.2, Aug 1998.

[35] L. Dossi, G. Tartara, and F. Tallone, "Statistical analysis of measured impulse response functions of 2.0 ghz indoor radio channels," *Selected Areas in Communications, IEEE Journal on*, vol. 14, no. 3, pp. 405–410, 1996.

[36] W. Mohr, "Modeling of wideband mobile radio channels based on propagation measurements," *Personal, Indoor and Mobile Radio Communications, 1995. PIMRC'95. 'Wireless: Merging onto the Information Superhighway'., Sixth IEEE International Symposium on*, vol. 2, pp. 397–401 vol.2, 1995.

[37] P. Bello, "Characterization of randomly time-variant linear channels," *Communications, IEEE Transactions on*, vol. 11, no. 4, pp. 360– 393, 1963.

[38] G. Martin, "Wideband channel sounding dynamic range using a sliding correlator," *Vehicular Technology Conference Proceedings, 2000. VTC 2000-Spring Tokyo. 2000 IEEE 51st*, vol. 3, pp. 2517 – 2521 vol.3, Apr 2000.

[39] A. Parr, B. Cho, and Z. Ding, "A new uwb pulse generator for fcc spectral masks," *Vehicular Technology Conference, 2003. VTC 2003-Spring. The 57th IEEE Semiannual*, vol. 3, pp. 1664 – 1666 vol.3, Mar 2003.

[40] M. Hamalainen, A. Nykanen, V. Hovinen, and P. Leppanen, "Digital stepping correlator in a wideband radio channel measurement system," *Personal, Indoor and Mobile Radio Communications, 1997. 'Waves of the Year 2000'. PIMRC '97., The 8th IEEE International Symposium on*, vol. 3, pp. 1120 – 1124 vol.3, Aug 1997.

[41] R. J. Pirkl and G. D. Durgin, "How to build an optimal broadband channel sounder," *Antennas and Propagation International Symposium, 2007 IEEE*, pp. 601 – 604, May 2007.

[42] A. Durantini, W. Ciccognani, and D. Cassioli, "Uwb propagation measurements by pn-sequence channel sounding," *Communications, 2004 IEEE International Conference on*, vol. 6, pp. 3414 – 3418 Vol.6, May 2004.

[43] A. Levy, J. Rossi, J. Barbot, and J. Martin, "An improved channel sounding technique applied to wideband mobile 900 MHz propagation measurements," *Vehicular Technology Conference, 1990 IEEE 40th*, pp. 513 – 519, Apr 1990.

[44] J. Austin, W. Ditmar, W. K. Lam, E. Vilar, and K. W. Wan;, "A spread spectrum communications channel sounder," *Communications, IEEE Transactions on*, vol. 45, no. 7, pp. 840 – 847, Jul 1997.

[45] T. Rappaport, *Wireless Communications: Principles and Practice*. Prentice Hall, 1996.

[46] M. Jeruchim, P. Balahan, and K. Shanmugan, *Simulation of Communication Systems: Modeling, Methodoloty, and Techniques*. Kluwer Academic/Plenum Publishers, 2000.

[47] P. Bello, "Characterization of Randomly Time-Variant Linear Channels," *IEEE Transactions On Communication Systems*, vol. 11, pp. 360–393, December 1963.

[48] G. Durgin, *Space-Time Wireless Channels*. Prentice Hall, 2003.

[49] "FCC part 15b regulations on U-NII band." [Online]. Available: http://www.atcb.com/publicdocs/fcc-03-287a1-UNII-Changes.pdf

[50] "ITU page on definitions of ISM bands." [Online]. Available: http://www.itu.int/ITU-R/terrestrial/faq/index.html

[51] A. Hewitt and E. Vilar, "Selective fading on los microwave links: classical and spread-spectrum measurement techniques," *Communications, IEEE Transactions on*, vol. 36, no. 7, pp. 789–796, 1988.

[52] P. Smulders and A. Wagemans, "Frequency-domain measurement of the millimeter wave indoor radio channel," *Instrumentation and Measurement, IEEE Transactions on*, vol. 44, no. 6, pp. 1017–1022, 1995.

[53] J. Parsons, *The Mobile Radio Propagation Channel*. John Wiley & Sons, Inc.,, 2000.

[54] R. Dixon, *Spread Spectrum Systems*, 2nd ed. John Wiley & Sons, Inc., 1984.

[55] J. Meel, "Spread spectrum (SS)," *De Nayer Instituut, Hogeschool Voor Wetenschap & Kunst*, December 1999.

[56] P. Karlsson and L. Olsson, "Time dispersion measurement system for radio propagation at 1800 MHz and results from typical indoor environments," *Vehicular Technology Conference, 1994 IEEE 44th*, pp. 1793–1797 vol.3, 1994.

[57] Y. D. Jong and M. Herben, "High-resolution angle-of-arrival measurement of the mobile radio channel," *Antennas and Propagation, IEEE Transactions on*, vol. 47, no. 11, pp. 1677–1687, 1999.

[58] G. J. Minden, J. B. Evans, L. Searl, D. DePardo, R. Rajbanshi, J. Guffey, Q. Chen, T. Newman, V. R. Petty, F. Weidling, M. Lehnherr, B. Cordill, D. Datla, B. Barker, and A. Agah, "An agile radio for wireless innovation," May 2007.

[59] A. Levy, J.-P. Rossi, J.-P. Barbot, and J. Martin, "An improved channel sounding technique applied to wideband mobile 900 MHz propagation measurements," MAY 1990.

[60] A. F. Molisch, *Wireless Communications*. John Wiley & Sons, Inc., 2005.

[61] S. Hara and R. Prasad, "Overview of multicarrier CDMA," *Communications Magazine, IEEE*, vol. 35, no. 12, pp. 126–133, 1997.

[62] "3GPP Specifications Home Page." [Online]. Available: http://www.3gpp.org/specs/specs.htm

[63] T. Inoue, D. Garg, and F. Adachi, "Study of the OVSF Code Selection for Downlink MC-CDMA," *IEICE Transactions on Communications*, vol. E88-B, pp. 499–508, Feburary 2005.

[64] L. Henzo, M. Munster, B. Choi, and T. Keller, *OFDM and MC-CDMA for Broadband Multi-User Communications, WLANs and Broadcasting*. John Wiley & Sons, Inc., 2003.

[65] N. Yee, J. Linnartz, and G. Fettweis, "Multicarrier CDMA in indoor wireless radio netwokrs," in *PIMRC*, September 1993, pp. 109–113.

[66] R. Peterson, R. Ziemer, and D. Borth, *Introduction to Spread Spectrum Communications*. Prentice Hall, 1995.

[67] D. Sarwate and M. Pursley, "Crosscorrelation properties of pseudorandom and related sequences," *Proceedings of the IEEE*, vol. 68, no. 5, pp. 593–619, May 1980.

[68] D. Sarwate, "Bounds on crosscorrelation and autocorrelation of sequences (corresp.)," *Information Theory, IEEE Transactions on*, vol. 25, no. 6, pp. 720–724, Nov 1979.

[69] D. Sarwate and M. Pursley, "Crosscorrelation properties of pseudorandom and related sequences," *Proceedings of the IEEE*, vol. 68, no. 5, pp. 593–619, May 1980.

[70] "Federal communications commission (FCC)." [Online]. Available: http://www.fcc.org

[71] A. Molina, P. Fannin, and J. Timoney, "Generation of optimum excitation waveforms for mobile radio channel sounding," *Vehicular Technology, IEEE Transactions on*, vol. 44, no. 2, pp. 275–279, 1995.

[72] T. Felhauer, P. Baier, W. Konig, and W. Mohr, "Optimum spread spectrum signals for wideband channel sounding," *Electronics Letters*, vol. 29, no. 6, pp. 563–564, 1993.

[73] Q. Shi and M. Latva-aho, "An exact error floor for downlink mc-cdma in correlated rayleigh fading channels," *Communications Letters, IEEE*, vol. 6, no. 5, pp. 196–198, May 2002.

[74] A. Coulson, "Bit error rate performance of ofdm in narrowband interference with excision filtering," *Wireless Communications, IEEE Transactions on*, vol. 5, no. 9, pp. 2484–2492, September 2006.

[75] U. Goni and A. Turkmani, "Ber performance of a direct-sequence cdma system in multipath fading mobile radio channels with rake reception," Jun 1994, pp. 747–751 vol.2.

[76] H. Xie, X. Wang, A. Wang, B. Qin, H. Chen, and B. Zhao, "An ultra low-power low-cost gaussian impulse generator for uwb applications," *Solid-State and Integrated Circuit Technology, 2006. ICSICT '06. 8th International Conference on*, pp. 1817 – 1820, Sep 2006.

[77] W. Ye-Qiu, L. Ying-Hua, Z. Hong-Xin, and H. Peng-Fei;, "Evaluation of uwb interference to the 3rd generation communication systems," *Environmental Electromagnetics, The 2006 4th Asia-Pacific Conference on*, pp. 161 – 164, Jul 2006.

[78] B. T. Ahmed, M. C. Ramon, and L. H. Ariet, "On the impact of ultra wide band (uwb) system on macrocell downlink of is-136 systems," *Wireless Communication Systems, 2006. ISWCS '06. 3rd International Symposium on*, pp. 645 – 649, Aug 2006.

[79] S. Brandes, I. Cosovic, and M. Schnell, "Sidelobe suppression in ofdm systems by insertion of cancellation carriers," in *Vehicular Technology Conference,*

2005. VTC-2005-Fall. 2005 IEEE 62nd, vol. 1, September 2005, pp. 152–156.

[80] T. Jiang and Y. Wu, "An overview: Peak-to-average power ratio reduction techniques for ofdm signals," *Broadcasting, IEEE Transactions on*, vol. 54, no. 2, pp. 257 – 268, Jun 2008.

[81] J. Proakis, *Digital Communications*, 4th ed. McGraw-Hill, 2000.

[82] "GNU Radio web site." [Online]. Available: http://www.gnuradio.org/trac/

[83] "USRP Signal Flow Block Diagrams." [Online]. Available: http://gnuradio.org/trac/browser/gnuradio/trunk/usrp/doc/usrp_rfx_diagrams.odp

[84] A. Saleh and R. Valenzuela, "A Statistical Model for Indoor Multipath Propagation," *Selected Areas in Communications, IEEE Journal on*, vol. 5, no. 2, pp. 128–137, Febuary 1987.